UNIVERSITÀ DEGLI STUDI DI PADOVA

Dipartimento di Fisica e Astronomia “Galileo Galilei”

Master Degree in Physics

Final Dissertation

Characterisation of the SpecMAT active target for the $\alpha(^{86}\mathrm{Kr},^{3}\mathrm{He})^{87}\mathrm{Kr}$ transfer reaction

Thesis supervisors
Prof. Francesco Recchia
Prof. Riccardo Raabe
Thesis co-supervisors
Dr. Oleksii Poleshchuk
Andreas Ceulemans

Candidate
Anita Candiello

Academic Year 2021/2022

Abstract

The SpecMAT active target was designed to study nuclei via direct reactions using very weak radioactive ion beams. Such studies will provide insights on the single-particle structure of states in key nuclei, helping the understanding of the changes in nuclear structure away from stability. The detector will be used in CERN inside the ISOLDE Solenoidal Spectrometer to exploit the secondary beams of the ISOLDE facility. The detector has been assembled at KU Leuven, where the first off-line tests had already been performed with an argon gas mixture. This thesis describes the performance of the SpecMAT active target with a helium gas mixture and a Monte-Carlo simulation of the $\alpha(^{86}\mathrm{Kr},^{3}\mathrm{He})^{87}\mathrm{Kr}$ transfer reaction that estimates the feasibility of its measurement with SpecMAT.

Contents

Foreword

The SpecMAT active target is a newly developed detector, which was designed and built at KU Leuven to study nuclei far from the stability valley through direct nuclear reactions. The core part of the active target is a gas-filled time projection chamber (TPC) in which the gas molecules are used both as the target for nuclear reactions and as the detection medium for reaction products. The TPC allows 3D reconstruction of the tracks left by light reaction products in the gas. Active targets are naturally oriented for studying isotopes produced with low intensity RIBs (Radioactive Ions Beams), due to their high efficiency and their large effective target thickness. In addition, SpecMAT combines the TPC detector for the tracking of charged particles with an array of $CeBr_3$ scintillation detectors for γ-rays spectroscopy. The active target will be placed in the ISOLDE Solenoidal Spectrometer (ISS) at the ISOLDE/CERN facility for identification of the light reaction products by the shapes of their trajectories in a homogeneous magnetic field and the amount of energy loss by the particles inside the gas volume.

This thesis describes the performance of the SpecMAT active target with a He(98%)CF_4(2%) gas mixture for the study of the low lying states in ^{87}Kr via the $\alpha(^{86}\text{Kr},^{3}\text{He})^{87}\text{Kr}$ transfer reaction. ^{86}Kr has 36 protons and 50 neutrons. 50 is a magic number, which corresponds to a closed shell configuration in the shell model theory. By adding an extra neutron, several low-lying states can be populated, corresponding to the transfer of the neutron in the orbitals such as 1νg7/2, 2νd5/2 and 2νd3/2. After a detailed analysis of the populated states it would be possible to deduce positions of these orbitals and thus contribute to the understanding of the evolution of the orbitals along N=50.

The SpecMAT active target has been assembled at KU Leuven, where it was characterized via a series of off-line measurements using an argon gas mixture. In this thesis the potential of the detector has been assessed with an off-line measurement in a He(98%)CF_4(2%) gas mixture at 1000 mbar by using a radioactive source containing three α-decaying isotopes (^{239}Pu/^{241}Am/^{244}Cm). The evaluated performance has then been compared to the previous results obtained with a Ar(95%)CF_4(5%) gas mixture.

In the analysis of the signals generated by the α-particles in the TPC and by the γ-rays in the scintillator array, it is possible to correlate the 5485.6 keV α-particle emitted in the α-decay of ^{241}Am with the 59.5 keV γ-ray emitted in the de-excitation of its daughter nucleus ^{237}Np.

Simulations of the $\alpha(^{86}\text{Kr},^{3}\text{He})^{87}\text{Kr}$ transfer reaction for the SpecMAT active target by using the SPCMsim simulation package based on Geant4 were performed in order to evaluate the feasibility of using the detector for the study of the reaction.

Particularly, ^{3}He ejectiles were produced inside the active volume of SpecMAT, filled with the helium gas mixture, in presence of a magnetic field. The ground state and the two low-lying states of ^{87}Kr (at $\sim$ 1.420 MeV and $\sim$ 1.476 MeV) were also populated in the reactions.

From the radius of the ^{3}He particle track combined with its emission angles, it was possible to reconstruct the kinematics of the reaction simulated and obtain the Q-value of the reaction and the excitation energy of the states populated in ^{87}Kr. The Q-value and excitation energy were then obtained by using the energy deposited by the ^{3}He ejectile in the TPC volume.

Chapter 1

Introduction

Ernest Rutherford, in 1911, discovered that the mass of the atoms is concentrated in its positively charged central core, named "nuclei" [1]. This discovery follows the Geiger-Marsden experiment in which a thin gold foil was bombarded with alpha particles. The aim of the experiment was to test Joseph John Thomson's plum pudding model of the atom, in which electrons were believed to be distributed throughout a positively charged matter. With the results of the gold foil experiment, Rutherford proposed that the electrons in the atom must be orbiting around its positive central core, like planets around the sun, opening the way for modern nuclear physics. In an experiment performed in 1917 and published in 1919-20 [2]- [3], Rutherford observed the proton (hydrogen nucleus) by investigating the byproducts of reaction of alpha particles with the nitrogen gas ^{14}N present in air via the first artificial nuclear reaction $^{14}N + \alpha \rightarrow {}^{17}O + p$. The composition of the nucleus was then finally established with the discovery of the neutron, an uncharged, distinct particle from the proton, by James Chadwick in 1932 [4].

Important subsequent experimental progress and theoretical efforts such as the development of quantum mechanics, the development of particle accelerators and of new experimental techniques allowed in the following years to enhance the knowledge about the atomic nucleus and its structure.

Nowadays it is well known that protons and neutrons (collectively called nucleons) are spin $\frac{1}{2}$ fermions with a mass of ~ 1 GeV/c^2 and are the main building blocks of a nucleus. The nucleons are kept in the nucleus thanks to the nuclear force, that is attractive at intermediate distances at the order of one fermi (10^{-15} m) of distance, overcoming the repulsive Coulomb force between protons. At the same time the nuclear force is repulsive at shorter distances (see Fig. 1.1).

One of the properties of the nucleon-nucleon force is that it is spin dependent. Indeed it has been observed that the nuclear force between nucleons having parallel spins is greater than the force between nucleons having anti-parallel spins. Moreover, it is (nearly) charge independent, i.e. the interaction between protons is the same as between neutrons, $V_{pp} \simeq V_{nn} \simeq V_{pn}$. This means that protons and neutrons are not distinguishable for the nuclear force. This nuclear force property was explained by Werner Karl Heisenberg [9] by introducing a new quantum number, the isospin T, and identified as the isospin symmetry, for which p and n represent different states of the same particle, the nucleon, that are characterised by different projections of T ($T_z = +\frac{1}{2}$ for the neutron and $T_z = -\frac{1}{2}$ for the proton, following the convention as in [9]). Any difference in behaviour between the nucleon interactions should be due to the fact that protons are also subject to the electromagnetic interaction and to the minimal mass difference from neutrons. The study of mirror nuclei, i.e. nuclei with inverted numbers of protons and neutrons, allows the quantitative investigation of the isospin symmetry in laboratory. There has been recently some hint that level splitting in mirror nuclei could not be explained by electromagnetic interactions alone and could suggest an isospin non-conserving term in the nucleon-nucleon interaction [10].

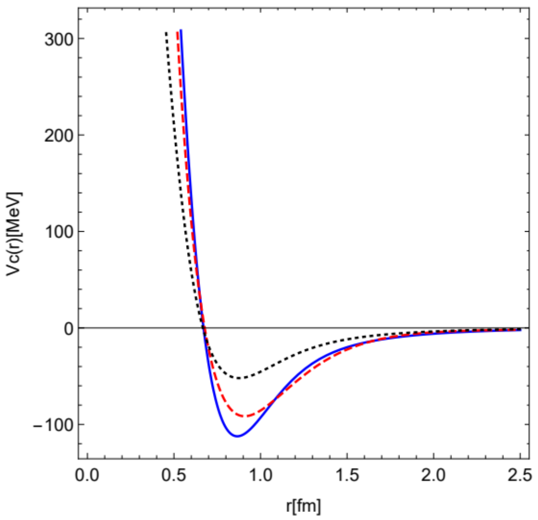

Figure 1.1: The figure shows the phenomenological nucleon-nucleon potential in the $^1S_0$ channel. Taken from Fig.1 of [5]. The three curves refer to the works of [6] (solid blue line, Argonne v_{18} potential), [7], (dashed red line, regularized version of the Reid soft-core potential) and [8], (dotted black line, charge-dependent Bonn potential).

Protons and neutrons were initially considered elementary particles but it was then understood that both are more appropriately described as colour-neutral, bound states of triplets of quarks. Quarks are elementary particles that come in different flavours, whose lowest mass ones are the 'up' quark (charge $+\frac{2}{3}$) and the 'down' quark (charge -$\frac{1}{3}$), that can form bound states either as triplets of quarks (baryons) / antiquarks (antibaryons) or as couples of quark/antiquarks (mesons). The nucleons are baryons: the proton is built up by the uud 'valence' quarks, and the neutron by udd, where u and d means respectively 'up' and 'down'. Quarks make up only $\sim$ 2% of the total nucleon mass. The rest arises from the kinetic energy of the constituents. Quarks have three kinds of 'colour charges' that sum up to zero in combinations of three and are carried by massless bosons called gluons. The quantum mechanical theory that describes quarks, gluons and their interactions is called Quantum ChromoDynamics (QCD). Due to its strong coupling constant $\alpha \sim 1$ it can not be effectively computed with perturbation theory calculation methods at low energies.

In the structure of nuclei the full complexity of the strong interaction does not usually come into play, owing to the fact that nuclei are relatively weakly bound systems. The energy required to remove a nucleon from a nucleus (separation energy) is $S \sim 8$ MeV along stability [11]. These energies are small compared with the rest energies (for nucleons $m_N c^2 \sim 1000$ MeV, but also for the lightest of the hadrons $m_\pi c^2 \sim 140$ MeV). While at low energies (<1000 MeV/nucleon; distance >1 fm) the interaction can be regarded as being mediated by the exchange of π mesons, the nuclear force between nucleons is now understood as the residual colour force between the constituent quarks mediated by the exchange of gluons.

In order to compare the experimental characteristics of the nuclear force with the predictions of QCD, the perturbative method being not viable, there is the need for some different techniques to do the calculations. Researchers developed the lattice QCD approach which, with the help of a lot of computing power, allows to simulate the effects of the theory to some specific cases. This approach currently allows computations of nuclei dynamics up to A = 4 [12], where A is the mass number of the nucleus, sum of protons and neutrons. An alternative method (ab-initio computations) establishes the two-nucleon interaction in order to compute global properties of the nuclei; several improvements brought this method to be viable up to A $\sim$ 50 [13]. Density functional theory allows to manage computations for more massive nuclei. As nucleons are added to the system, the number of nucleon-nucleon(-nucleon) interactions increases rapidly and with the current computing capabilities these calculations are often too complex to be solved in a reasonably short time, thus approximations and effective theories have been employed.

Several nuclear models, such as the liquid drop model, the shell model and the collective model have been developed, providing description of the observed nuclear properties for different regions of the nuclide chart. The predictions of these models also help the researchers searching not yet known isotopes. Systematic analysis through the comparison between the values computed via the semi-empirical mass formula [11] of the liquid drop model with experimental data of the binding energies led Walter Elsasser [14] and Kurt Guggenheimer [15] in 1933 to the identification of “magic numbers” of protons and neutrons that provide greater stability to the nuclei. For these nuclei the proton (neutron) separation energy, S_p (S_n), is strongly increased and hence nuclei have a particularly stable nuclear configuration. The binding energy, i.e. the energy that holds nucleons together in the nucleus, is defined as the difference between masses of protons m_p and neutrons m_n that compose the nucleus and the mass of the nucleus itself $B = Zm_p + Nm_n - m_{^A_ZX_N}$, where Z is the number of protons, N is the number of neutrons and A is the mass number. In an effort to explain these properties the “nuclear shell model” was developed. In this phenomenological model the nucleons move in a mean field potential generated by all nucleons in the system; closed shells of protons and neutrons are more strongly bound and stable. The initial version the shell model did not reproduce correctly the stability numbers, so different choices of central potential were tested. From the study of the harmonic oscillator potential it was then acknowledged that something important was still missing to obtain the real magic numbers. In 1949 Maria Goeppert Mayer [16]- [17] and Otto Haxel, Hans Jensen and Hans Suess [18] improved the potential by adding a spin-orbit term that allowed the shell model to predict several properties of nuclei, including the emergence of the magic numbers of 2, 8, 20, 28, 50, 82 and 126 nucleons that characterise more stable and bound nuclei. This model is currently the most widely used theoretical model that describes the atomic nuclei.

In Figure 1.2 the chart of Segrè is presented [19]. The chart of nuclides shows all the nuclides with experimentally evaluated properties, sorted according to the number N, in the abscissa, and Z in the ordinate. The different colours represent the half-lives of the nuclides. The magic numbers are also indicated. The stable isotopes are shown as black dots in the centre of the chart (also known as the ”valley of stability”), they constitute constitute only a small part (254 as reported in [20]) of the all discovered ones ($\sim$ 3300 as reported in [21]), which for the most part are radioactive . With the developed models it is possible to predict the existence of $\sim$ 7000 nuclides [21].

In order to study the nuclei, some advanced experimental techniques were developed. The kinetic energy of the particles emitted in the decay of naturally radioactive sources is barely enough to overcome the nuclear potential barrier and to interact with nuclei beyond elastic collisions. In 1932 John Cockcroft and Ernest Walton, after proposing a novel approach, with the development of a charged particle accelerator, performed the first nuclear reaction p + ^{7}Li $\rightarrow 2\alpha$, in which a proton beam was accelerated to energies ranging from 100 to 600 keV [22]. Later the technique was further improved, allowing to reach higher energies of the accelerated nuclei. This newly acquired capability for artificial disintegration of the atomic nuclei via particle accelerators triggered a new generation of experimental investigations.

Initially only the stable nuclei were available to create ion beams. Since the 1960s (with the first proposals dating back in the 1950s by Otto Kofoed-Hansen and Karl-Ove Nielsen, [23]), the advent of Radioactive Ion Beam (RIB) facilities provided access to the unexplored regions on the nuclide chart. To better characterise the nucleon-nucleon interaction it is necessary to probe the behaviour of exotic nuclei far from the valley of stability, i.e. nuclei with a big difference between the number of protons and neutrons. In such exotic p/n unbalanced nuclei the magic numbers are modified due to specific nucleon-nucleon interactions and as a result some magic numbers disappear and some new ones appear. This phenomenon is known as shell evolution.

Direct reactions can be used to study the shell evolution in chains of nuclides. Reaction observables

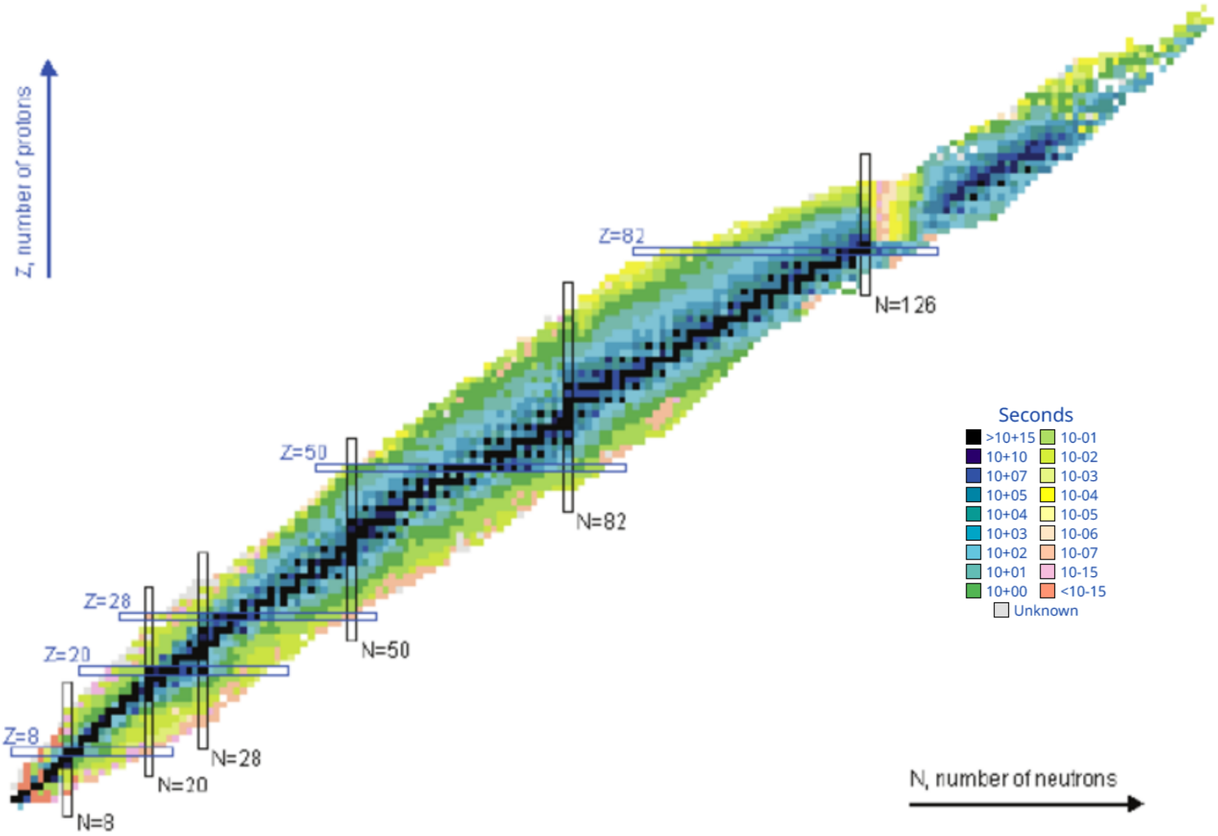

Figure 1.2: Nuclides chart [19]. The colours represent the half-lives of nuclides. The magic numbers are indicated with vertical and horizontal lines.

that will help to understand the nuclear structure can be extracted experimentally with detector setups. To detect, track and identify the particles of the reactions and to study the main property of the nucleus, (such as the structure, the half-life, its energy, momentum, spin, charge) one or more detectors are usually placed near the focal point of the reaction. Detectors usually consist of layers of different types of material, which are used to either show the path of a particle as it travels along, or absorb it to make the particle stop. Each one has different properties that can make it more suitable for studying a certain type of particles and to get information on a specific aspect of the reaction.

The main goals of this thesis are: 1) an evaluation of a He-based gas mixture performance in the SpecMAT active target for perspective nuclear transfer reaction studies; 2) Investigating the feasibility of a $\alpha(^{86}\text{Kr},^{3}\text{He})^{87}\text{Kr}$ reaction studies with SpecMAT using a Monte-Carlo simulation toolkit.

SpecMAT combines two types of detectors: a gas-filled time projection chamber (TPC), a core detector for tracking charged particles emitted in nuclear reactions and an array of auxiliary scintillation detectors for γ-ray spectroscopy.

In the following sections, an overview of the nuclear shell model and the experimental techniques developed to probe the nuclear structure is presented. The part dedicated to the experimental techniques describes the physics of the radiation interaction with matter and two detector types: active targets and scintillation detectors. The following section is dedicated to the reactions that can occur in a nuclear experiment and particularly to the transfer reactions. Chapter 2 provides an overview of the SpecMAT active target and describes the characterisation of the detector performance with a helium gas mixture. In Chapter 3 the results obtained from the simulations of the $\alpha(^{86}\text{Kr},^{3}\text{He})^{87}\text{Kr}$ transfer reaction in the SpecMAT active target are shown. This simulation is aimed at the evaluation of the feasibility to study the reaction with the active target. In Chapter 4 the final considerations will be discussed.

1.1 The Nuclear Shell Model

The nuclear shell model, with the spin-orbit term discovered by Maria Goeppert Mayer [16]- [17] and Otto Haxel, Hans Jensen and Hans Suess [18], assumes that protons and neutrons can have only specific discrete energies and occupy orbits according to the Pauli Exclusion principle. The main idea of the shell model is to consider all nucleons as subject to an average central, spherically symmetric potential produced by all the nucleons.

The nucleus is a strongly interacting quantum many-body system and the levels allowed by this system can be identified by solving the Schrödinger equation:

$$\hat{H}\psi = (T+V)\psi = E\psi \tag{1.1}$$

where ψ is the state vector, the wave function representing the nucleus, E the associated energy, eigenvalue of the system and $\hat{H}$ is the Hamiltonian that can be rewritten as the sum of the kinetic energy plus the many body interaction between the nucleons inside the nucleus.

The Hamiltonian can be approximated with a two-body interaction as:

$$H = \sum_{i=1}^{A} T_i + \sum_{i<j=1}^{A} V(\vec{r_i}, \vec{r_j}) \tag{1.2}$$

where T_i is the kinetic energy of each particle inside the nucleus, and $V(\vec{r_i}, \vec{r_j})$ is the interaction potential between nucleons $\vec{N_i}$ and $\vec{N_j}$. This term includes the repulsive component at short distances ($<$ 0.5 fm), an attractive term at intermediate distances (0.5 fm $< r <$ 1 fm) and the Coulomb interaction between protons at greater distances. It is known that the strong interaction exploits also a three-body term that is non-negligible due to the high intensity of the strong interaction coupling constant at the typical nuclear excitation energies (a few MeV). Solving the many-body problem is complex and does not allow to obtain an exact solution of the equation.

The Hamiltonian of Eq.(1.2) can be further simplified by assuming that the nucleons, described as independent particles, move in a central one-body potential, created by the combined effect of all the two-body interactions. This can be implemented by adding and subtracting the average potential $U_{M.F.}(\vec{r}) = \sum_{i=1}^{A} u(\vec{r_i})$ where $u(\vec{r_i})$ is the single-particle potential energy, and $\vec{r_i}$ is the coordinates of each nucleon:

$$H = [\sum_{i=1}^{A}(T_i + u(\vec{r_i}))] + [\sum_{i<j=1}^{A}(V(\vec{r_i}, \vec{r_j}) - \sum_{i=1}^{A} u(\vec{r_i}))] = H_{M.F.} + H_{res} \tag{1.3}$$

Now the Hamiltonian can be interpreted as the mean field Hamiltonian $H_{M.F.}$ created by all the particles plus a residual interaction H_{res}, that can be made small with a proper choice of U and can be considered as a perturbation.

In the first-order approximation, by neglecting the residual interaction, the Schrödinger equation can be solved for $H_{M.F.} = \sum_{i=1}^{A}(T_i + u(\vec{r_i}))$. The eigenvalues of the Hamiltonian are the single-particle energies (SPE), the energy for each single particle orbit.

Usually, the mean field potential can be approximated with the Wood-Saxon potential $V_{W.S.}$:

$$V_{W.S}(r) = -\frac{V_0}{1 + e^{(r-R_0)/a}} \tag{1.4}$$

where V_0 represent the depth of the potential well, R_0 represents the mean radius of the nucleus, and a is a parameter that reflects the skin thickness of the well, defined as the distance over which the nuclear charge density falls from 90% of its central value to 10%.

By adding a spin-orbit term (V_{ls}), an orbital angular momentum (V_{ll}) term and the Coulomb interaction (V_C) to $V_{W.S.}$, the mean field potential $U_{M.F.}$ can be written:

$$U_{M.F.}(\vec{r}) = V_{W.S.}(\vec{r}) + V_{ls}(\vec{r})\,\vec{l}\cdot\vec{s} + V_{ll}(\vec{r})\,\vec{l}\cdot\vec{l} + V_C(\vec{r}) \tag{1.5}$$

where l and s are respectively the orbital angular momentum and the intrinsic spin of the nucleons.

By solving the equation of Schrödinger with this choice of $U_{M.F}$, the single-particle spectrum, with the magic numbers 2, 8, 20, 28, 50, 82 and 126, can be obtained. An illustration of the single-particle spectrum in Fig. 1.3 describes the shell structure of a nucleus with highlighted closed shells.

The study of the validity of the shell model for nuclei away from the valley of stability has shown that the magic numbers obtained with this model do not find a correspondence across the entire chart of nuclides. Examples of the shell evolution can be find in Ref. [24], [25], [26].

Some changes of shell structure have been explained by the effect of the monopole part of the residual interactions, in particular by its tensor (non-central) component, which takes into account the interaction between nucleons. In the case of many nucleons outside a closed shell, correlations and interactions between nucleons have to be considered, and thus the H_{res} is not negligible anymore and has to be included in the model.

The shell-model approach, to keep the problem computationally tractable, is then switched from the full Hilbert space to a restricted space, a valence space. By means of a regularization procedure, aimed to soften the short range repulsion, the effective interactions are then computed. The behaviour of the nuclear system is analysed by using the effective interactions in this restricted space. The requirement is that all expectation values in the full space be equal to the expectation values of the restricted space.

For a given number of protons and neutrons the nuclear orbitals can be grouped in three regions:
- inert core, which is composed of full orbits and in which nucleons do not interact between each other;
- valence space, in which the orbits are partially populated by the nucleons, that determine the properties of the nuclear system, and in which the particles distribution is governed by the effective interactions;
- external space, composed by high-lying orbitals whose occupation by valence nucleons is energetically very unlikely and, therefore, are considered always empty and are not taken into account for calculations.

In order to further develop the existing nuclear models, new experimental information is required especially about the nuclei located far from stability. However, such studies are challenged by difficulties associated with production of these exotic isotopes. For this purpose new facilities and techniques have been developed and research is actively on-going in this domain.

1.2 Experimental techniques

The nuclear structure can be studied with direct nuclear reactions using various experimental techniques. Several of such techniques and devices have been developed and improved in the last years. The available range of tools covers a wide range of particle accelerators, beam isotopes, target materials and detectors.

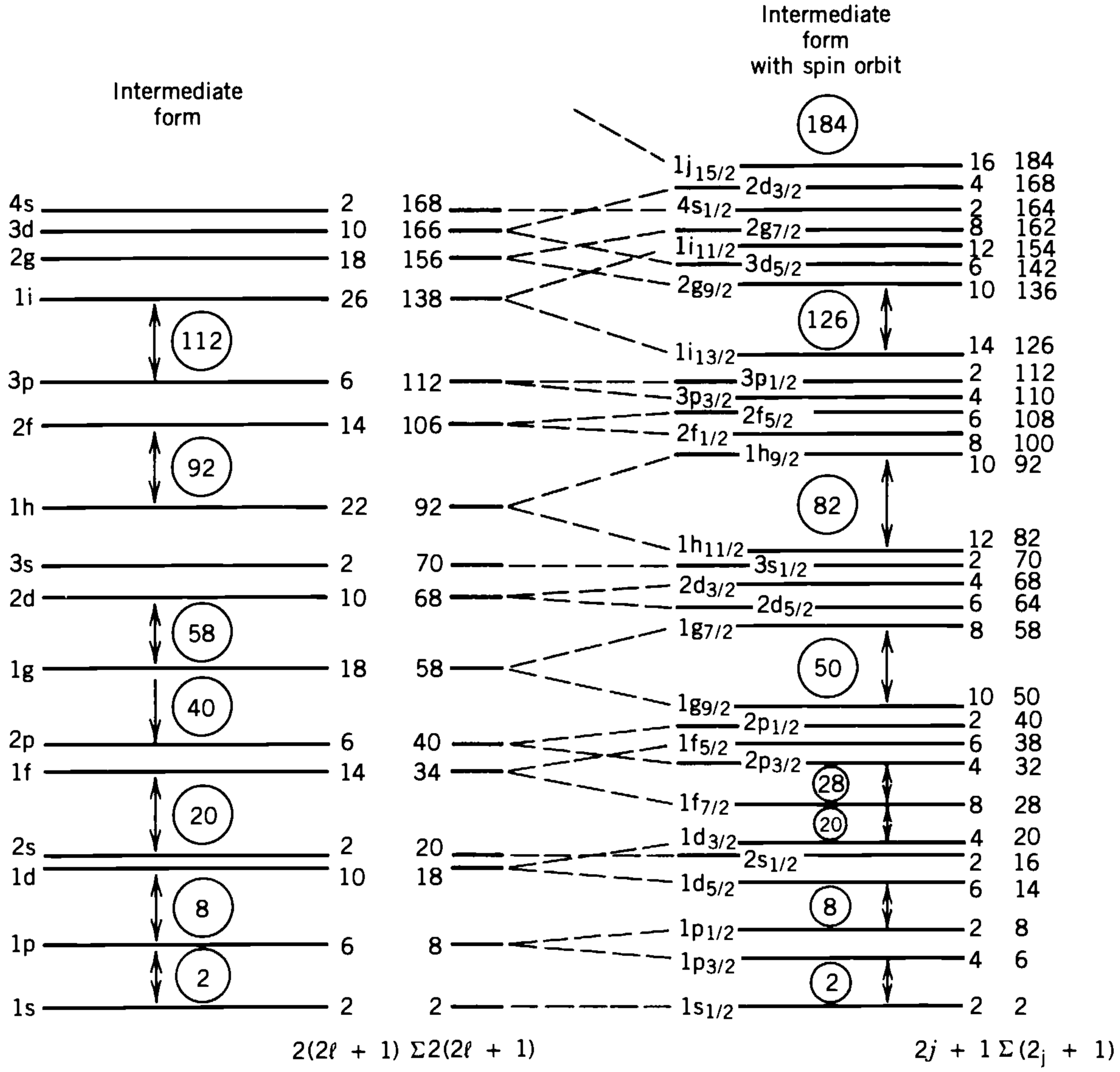

Figure 1.3: Single-particle energy spectrum. The energy levels on the left are calculated with the Wood Saxon potential. To the right of each level the capacity, the number of nucleons that can be put in it and the cumulative number of nucleons up to that level are reported. On the right the effect of the spin-orbit interaction, which splits the levels with l>0 into two levels is shown. The image is taken from Fig. 5.6 of Ref. [11]

1.2.1 Radioactive ion beam facilities

After the development of the first accelerator by John Douglas Cockcroft and Ernest Thomas Sinton Walton [22], despite big improvements of the facilities to accelerate particles like cyclotrons and synchotrons, at the beginning only less than 300 natural nuclides (including primordial nuclides [21]) were available to create ion beams. It was since the advent of radioactive ion beam facilities in the '60s, that became possible to create rare isotopes and radioactive ion beams with unstable elements. This new technique allows the production of more exotic nuclei far from the valley of stability. The requirements for a RIBs production facility are:
- efficiency, as the typical RIBs production rates of these facilities are low. The total efficiency is defined as the ratio of the number of nuclei per second (intensity of the beam) delivered at the experimental setup with respect to the nuclei produced in the primary reaction target.
- selectivity, with a high capability of eliminate 'contaminants'. The isotopes of interest often represent a minority of the whole production yeld. Other primarily produced isotopes can be much more abundant than the isotopes of interest.
- rapidity, as required by the radioactive isotopes with short half-life. The time between the moment of production and the arrival to the experimental set-up has to be short compared to the half-life.
- production rate, with a large cross section, obtained by optimising the production mechanism (beam-target combination, beam energy, high intensity of the primary beam, power dissipation into the target).

There are two main techniques for the RIB production: the ISOL (Isotope Separation On-Line) and the in-flight separation methods.

ISOL facility

In these facilities high energetic stable ions or neutrons are used as the primary beam and are directed towards a sufficiently thick target. The reaction products are thermalised in the target and diffused out of the material. Then, through a specifically designed transfer tube, isotopes are transported to an ion source (e.g. surface ionisation, plasma, laser) where originally neutral atoms can lose or gain electrons and become ions. The typical times of diffusion and effusion, that are chemical processes, may vary widely, from fraction of seconds to more than hours. To increase the diffusion rate the target is kept at high temperatures (more than 2000 °C). In the collision of the primary beam with the target material, several reactions can occur, resulting in the production of a very large range of nuclei. The nuclei of interest are only a small fraction of the whole production, which is dominated by nuclides close to the valley of stability. These radioactive isotopes are accelerated and then separated by high-resolution electromagnetic separator, where the isotopes of interest with the specific mass and charge can be selected and further delivered to the experimental setups (e.g. for transfer reaction studies).

Due to the low energies of ions which are extracted from the ion source, the ISOL technique is suitable for low energy experiments (typically 30 to 50 keV [27]) for example nuclear decay spectroscopy or solid state applications are possible end-uses of ISOL. Also, post-acceleration of the ions by various accelerator techniques that allow to reach tens of MeV, can be used for nuclear reaction studies. To achieve a high acceleration efficiency in the post-accelerator the charge state of ions is boosted by a charge breeder, a device aimed at stripping many electrons from the ions. A schematic view of an ISOL facility is shown in Fig. 1.4.

One of the main reaction channels responsible for the ISOL ions production is fission. Therefore, a target containing heavy elements, such as tantalum, uranium or thorium is irradiated by a light particle beam (like protons or deuterons). This technique produces predominantly neutron-rich isotopes. The production of nuclei with excess of protons or neutrons can also be obtained by fragmentation, the peripheral interaction of the high energy light ions of the beam with the heavy target nucleus that causes portions of the target nucleus to be removed. Other typical mechanisms than can be employed

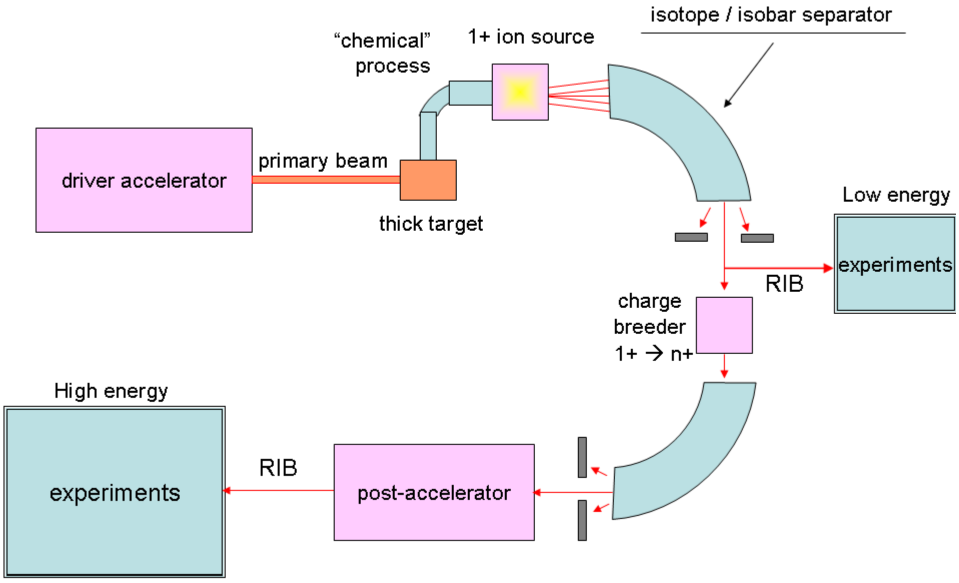

Figure 1.4: Schematic view of ISOL facility. The image is adapted from Fig.2 of Ref. [28].

to study neutron-deficient nuclei are spallation and fusion reactions [27].

The main advantages of an ISOL facility are its selectivity and the high quality (small emittance and small beam energy spread) of the beam. The high selectivity of the ISOL technique is ensured by several stages of isotope manipulation: ion sources provide the first selection of isotopes, then isobaric purification of the isotopes can be reached in electromagnetic separators. An important property that express the quality of the system is the mass resolving power $\frac{A}{\Delta A}$, defined as the ratio between the mass of the isotope A and ΔA, the minimum difference between two masses that can be separated in the magnet: this number can vary between a few hundreds and a few thousands. Other ways to improve the selectivity can include the use of ion traps and time-of-flight methods.

The isotopes production process strongly depends on the chemical properties of the produced atoms and ions of interest. However, for each species of isotopes a long development is necessary to optimise those chemistry-dependent procedures. Furthermore, short-lived isotopes cannot be obtained because of the time required for diffusion and effusion. In this sense, the ISOL method is complementary to the in-flight method, which allows a fast delivery of the produced isotopes.

ISOLDE at CERN (Switzerland) [29]- [30], SPIRAL and SPIRAL2 in GANIL [31]- [32] (France), ISAC at TRIUMF [33] (Canada) and the future SPES at Legnaro National Laboratory (Italy) [34], are examples of ISOL facilities.

In-flight facility

Another technique for the RIB production is the in-flight separation, where radioactive ions are obtained through the collision of energetic heavy ions (E > 30MeV/u) on a thin target made of light elements. The reaction fragments are ejected in the forward direction with respect to the beam; as a significant part of the primary beam energy is transferred to the reaction fragments, these are characterised by high energy. The reaction fragments then pass through the thin target without a substantial energy attenuation and therefore they do not require a further acceleration for physics studies. The isotopes of interest are then separated and identified with an in-flight fragment separator. A schematic view of the facility is shown in Fig. 1.5.

Depending on the choice of the target material, the most common reaction mechanisms are fragmentation (with beryllium and carbon targets), spallation (with targets containing proton) and fission (for

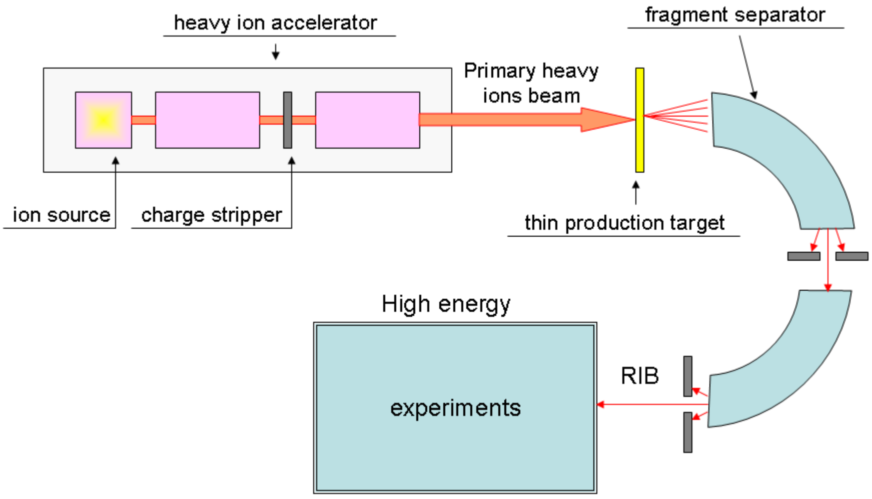

Figure 1.5: Schematic view of in-flight production method. The image is adapted from Fig.1 in Ref. [28]

all target materials).

The main separation process of in-flight facility consists in the deflections of ions passing through a series of large magnetic dipoles according to their magnetic rigidity Bρ, where B is the magnetic field perpendicular to the particle velocities and ρ is the radius of curvature of the particle path in the magnetic field. The magnetic rigidity is defined as:

$$B\rho = \frac{p}{Q} = \gamma \frac{Au}{Ze} \beta c \tag{1.6}$$

where p and q are respectively the momentum and the charge of the particle, $\gamma = 1/\sqrt{1-\beta^2}$ is the Lorenz factor, A is the atomic mass and u=931.5 MeV/c^2 is the atomic mass unit (Au is the mass of the nucleus), Z the atomic number, e the electric charge ($Q = Ze$ the total charge of the nucleus), β the velocity of the particle (β= $\frac{v}{c}$ where c is the speed of light in vacuum). The magnetic rigidity depends on the velocity and on the mass-to-charge ratio of the particles. While in the ISOL technique the first element separation is managed through chemical processes, in the in-flight technique a different selection is needed. The separation can be achieved by inserting a wedge-shaped degrader between two dipoles. When charged particles pass through the degrader, they lose energy according to the Bethe-Bloch formula [35]. The energy loss is dependent on the atomic number Z, the energy E, and the mass m of the ion ($\frac{dE}{dx} \propto \frac{mZ^2}{E}$, where $\frac{dE}{dx}$ is the differential energy loss for the particles within the material divided by the corresponding differential path length dx). Therefore, isotopes with different Z are subjected to different amount of energy loss and come out of the passive material with distinct velocities that, for nuclei with the same mass-to-charge ratio $\frac{A}{Q}$, means different rigidities and thus trajectories. The degeneracy in $\frac{A}{Q}$ is thus removed.

An advantage of this method to respect the ISOL technique is that the production of the RIBs is independent of the chemical properties of the elements and no chemical separation is needed. Moreover, in-flight separation method is very fast (100 ns), so that isotopes with very short half-lives can be produced as RIBs and the radioactive beams are directly available at high energy, with no need for post-acceleration. On the other hand, as the quality of the RIBs is poor (large energy spread and transverse emittances) and the separation of isotopes is not complete, a contamination by secondary products is present and a ion-per-ion identification has to be performed.

GSI in Germany [36]- [37], RIBF at RIKEN Nishina Center in Japan [38], GANIL [39] in France, NSCL [40] and the future FRIB [41] in USA are examples of in-flight facilities.

1.2.2 Detectors

As nuclear reactions are very powerful tools to investigate the nuclear structure, detectors are needed to observe the particles produced and to study the reactions.

Different types of radiation detectors with different characteristics, depending on the type of incident radiation (charge particles, fast electrons, neutrons and electromagnetic radiations like γ-rays and X-rays) and the properties subject of analysis are used to identify and study the reaction products. The principle for the radiation detection is that the radiation must interact with the material of the detector itself and all or a part of the radiation energy is transferred to the detector mass. Charged particles release their energy to matter through direct collisions with the atomic electrons, inducing excitation or ionisation on the atoms, depending on their energy. Neutrons, instead, must first interact with the detector material through nuclear reactions in order to produce charged particles, which then ionise and excite the detector atoms. Photons can be fully absorbed, or can deposit only a part of their energy in the detector material, or can produce an electron-positron pair through the three main interaction mechanisms (a more detailed discussion can be found in Section 1.2.5). The strategy to collect and convert the energy in signal depends on the detector and its design. For example the electrons produced by ionisation can be collected to form an electric current signal or both excitation and ionisation processes can contribute to the signal by inducing molecular transitions which result in the emission of light.

The main characteristics that a detector should have are [35]- [42]:

- **sensitivity**: the capability of the detector, given a type of radiation and energy, to produce a usable signal. Detectors are indeed designed to be sensitive to only certain types of radiation in a specific range of energy.

- **response function**: the relation between the incident radiation energy and the output signal of the detector. In general, the amount of ionisation produced corresponds to the electrical charge collected. Hence the detection produces a current pulse signal proportional to the energy the radiation loses in the sensitive volume of the detector. Ideally, but often not the case, the signal should be always the same for a given particle at a certain energy and possibly it should vary linearly with the energy of the radiation.

- **energy resolution**: the minimum energy difference that the detector can distinguish. It can depends on the energy of the incoming particle. Ideally, a monochromatic radiation should result in a delta-function peak. Because of statistical fluctuations in the number of ionisations and excitations produced inside the detector and the noise, it always results in a Gaussian peak with a finite width. The width parameter of the peak, the standard deviation σ, define the Full Width Half Maximum (FWHM) of any Gaussian through the relation FWHM $\simeq 2.35\sigma$. Usually expressed as a percentage, the resolution is conventionally defined as the FWHM divided by the position of the centroid of the peak E_0. The energy resolution R is thus a dimensionless fraction of the energy of the radiation deposited on the detector E_0:

$$R = \frac{\Delta E}{E_0} = \frac{FWHM}{E_0} \simeq \frac{2.35\sigma}{E_0} \tag{1.7}$$

- **detection efficiency**: it is related to the capability of the detector to detect the totality of events of interest emitted by the radioactive source.

The absolute efficiency ϵ_{abs} is the ratio between the number of recorded events and the number of events emitted by the source and it depends on the detector properties and on the geometrical configuration of the detection system, mainly the source-detector distance and the solid angle covered by the detector:

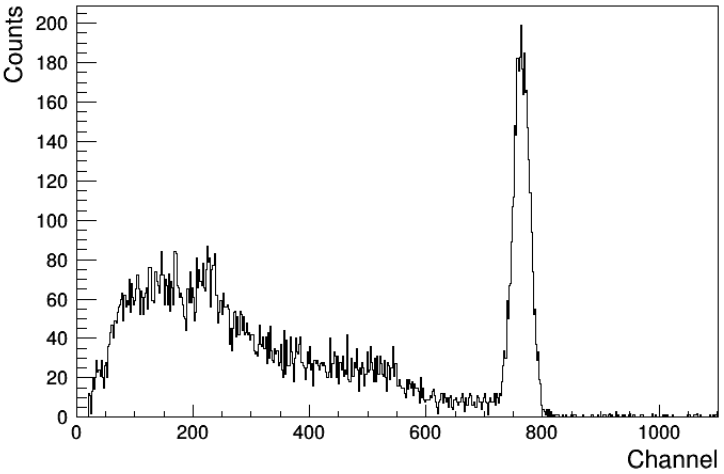

Figure 1.6: Spectrum measured using a scintillation detector obtained using a ^{137}Cs source. The peak corresponds to the $\sim$ 662 keV γ-ray emitted from the decay of cesium-137.

$$\epsilon_{abs} = \frac{\text{Number of events detected}}{\text{Number of emitted events}} \tag{1.8}$$

The intrinsic efficiency ϵ_{int} is defined as the ratio between the number of recorded events and the number of radiation events that hit the detector:

$$\epsilon_{int} = \frac{\text{Number of events detected}}{\text{Number of incident events}} \tag{1.9}$$

ϵ_{int} strongly depends on the interaction cross sections of the incoming radiation with the detector medium and thus on the type and on the energy of the incoming radiation. It does not take into account the geometric factors.

The absolute efficiency can be factorized as: $\epsilon_{abs} = \epsilon_{int} \cdot \epsilon_{geom}$, where ϵ_{geom} is the geometric efficiency, the fraction of the radiation coming from the source which is geometrically intercepted by the detector, which depends on the solid angle coverage. The angular distribution of the incident radiation has also to be considered.

The peak-to-total ratio r, defined as the ratio between the number of counts in the peak and the total number of counts on a given spectra:

$$r = \frac{\epsilon_{peak}}{\epsilon_{total}} \tag{1.10}$$

is an other important value to be taken into account while studying the detector proprieties and the energy spectrum. In the total efficiency all the interactions recorded in the detector are counted, independent on the energy deposited by the radiation. In the peak efficiency, instead, only the interactions that deposit the full energy of the radiation are considered. Usually it is preferable to use peak efficiencies, because the number of events with the total energy of the radiation is not affected by perturbing effects such as scattering from surrounding materials or noise events. Anyway there can still be noise at the position of the peak that needs to be taken into account in the measurements of efficiency.

In Fig. 1.6 as an example a spectrum acquired by the array of CeBr$_3$ scintillators of SpecMAT is shown. The Full-energy peak has a gaussian shape and corresponds to the total energy of the radiation detected (in this case γ-rays emitted during the decay of a ^{137}Cs source).

- timing properties: the *response time* of a detector is the time needed to form and process the signal after the arrival of the radiation in its sensitive volume. This is also important as a measure of the timing resolution that a detector can reach. The *dead time* is the finite time a detector needs to process an event (to shape and to amplify the pulse) and fully recover, i.e. to be ready for the following event. It is a measurement of the minimum separation in time between two events in order to be recognized and analysed as two separate pulses. The limiting time may be due to the detection processes or may arise in the electronics associated to the detector. During this period, a second event cannot be accepted. The dead time limits the counting rate that the detector can achieved.

Experiments with RIBs are conditioned to deal with the low intensity of the beam: from $\sim 10^{11}$-10^{12} particle per second (pps) for stable beam down to a few pps for other conditions. In order to reconstruct the kinematics of the reaction event and thus to calculate the energy balance of the process, detectors with high efficiency and sensitivity are needed. The detectors have to be able to record and identify the largest possible number of events of interest and ensure good energy and position resolution.

1.2.3 Active target

To compensate for the low intensity of the RIBs, that limits the luminosity of experiments which use them, thick targets and high efficiency detection system are needed. In experiments with passive materials as targets the luminosity can be enhanced by increasing the target thickness, but at the expense of a deterioration in the resolution that can be achieved. Indeed, for these detectors, the collision point of the nuclear reactions can not be determined with high precision and it is not possible to detect or reconstruct the energy loss by particles inside the target, introducing a spread in the observed energy of the charged products.

Active targets are naturally oriented to the study of short-lived radioactive nuclei with RIBs, due to their high efficiency and the large thickness. The core part of these detectors is a Time Projection Chamber (TPC), a gaseous detector for charged particles tracking. The term 'active' means that the atomic nuclei of the gas molecules employed as the target material for nuclear reactions are simultaneously used as the detector medium. In this way the vertex of the reactions can be directly tracked for each event and it is possible to correct for the energy loss inside the target. Therefore, the target thickness does not influence the determination of the particle energies at the reaction point. Because the reaction happens within the detection medium, a large solid angle (almost 4π) of the emitted reaction products is covered in the active targets. This enhances the detection efficiency and further provides to increase the luminosity. Moreover, due to inverse kinematics, the energies of the recoil particles that carry the kinematic information of the reaction can vary over a wide range and in active targets the recoil particles of low energies do not need to escape from target material to be detected. Therefore there is no loss of statistics and the target thickness does not impact on the angular resolution. By combining energy information of particles for a particular reaction mechanism with the kinematics of the process, identification of the nuclear species of interest can be achieved.

A Time Projection Chamber [43] is an ionisation detector in which the incoming radiations, energetic charged particles, by traversing the detection volume ionise the atoms of the gas (or liquid) and produce three dimensional ionisation tracks. A two-dimensional tracks reconstruction is possible by collecting the electrons produced along the path into a position-sensitive anode. A schematic view of the working principle of a TPC is shown in Fig. 1.7. High voltage is applied between the electrodes of the chamber to produce the electric field that causes the electrons to drift towards the anode. In order to be detectable, the electron signal needs to be amplified. Therefore electrons pass through an amplification zone, where their number is multiplied, before reaching the anode. Here the particles can be detected on the readout plane, perpendicular to the drift direction, which is composed by segmented pads. For a precise measurement of the positions of particle trajectories a very homogeneous electric field is needed. This can be achieved by a field cage, which usually consists of conducting rings or wires around the chamber, that allows to divide the high potential from the cathode stepwise down

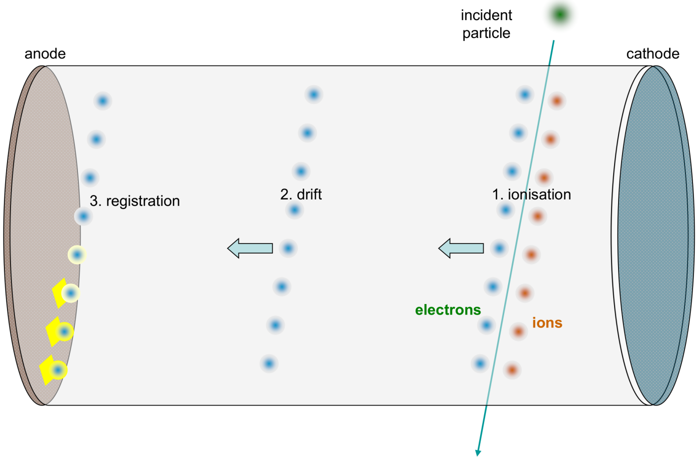

Figure 1.7: Working principle of a time-projection chamber. The incoming particle ionise the atoms of the gas. An electric field guides the positive ions and the electrons to drift towards the cathode and the anode, respectively. The electrons first pass towards an amplification stage where are amplified and then are collected in segmented pads which generate the signal that allows the two-dimensional reconstruction of the tracks of the incident particle.

to the anode. While the electrons signal permits the reconstruction of a two-dimensional projection of the ionisation track, information on the third dimension can be derived from the measurement of the drift time of the electrons passing through the gas volume.

In the active target mode the events of interest are produced in the interaction between the incoming beam nuclei and the nuclei of the target gas atoms of the TPC. In Fig. 1.8 the working principle of an active target is shown. As well as through reactions, the detector can be used to study unstable nuclei by measuring the charged particles emitted in their decays. In this case, a beam of the nuclei of interest is stopped inside the detector volume, where the subsequent decay is recorded. Around the world several active target projects [44]- [45] have been realized with the aim of getting a better insight in the nuclear structure of nuclei far from stability.

Besides an increase of the target thickness, the large energy range of the high energetic light recoil of nuclear reactions can be covered in different ways. Some active targets make use of a solenoid inside which the active volume is placed. A strong homogeneous magnetic field parallel to the beam direction is applied and the consequence is a curvature of the trajectory of the charged particles. This results in lengthening of the tracks within the active volume, and thus higher energy particles release all their energy inside the gas volume, where they stop. Therefore, the energy of the particles can be estimated from the amplitude of the signals collected along the whole track. Particles identification is based on the measurement of the radius of curvature of their trajectories and on the amount of energy left by the particles in the gas.This is the method used for example in the AT-TPC detector [47] and in the SpecMAT [48] active-target, focus of this thesis. A different approach, employed in experiments without using a magnetic field, consists on the combination of the active target with ancillary charged-particle detectors. They can be situated around the active target with the function of intercepting particles that escape the gas volume, due to their high energies. Particles identification relies on the ΔE-E method: the energy loss in the active volume ΔE detector is combined with the residual energy E detected in the ancillary detectors. Examples of detectors using this technique are MAYA [49] and ACTAR [50] active targets.

1.2.4 Interaction of heavy charged particles with matter

Heavy charged particles, such as alpha particles, interact with matter in a continuous way through the electromagnetic interaction with mainly the electrons of the medium they cross. This interaction

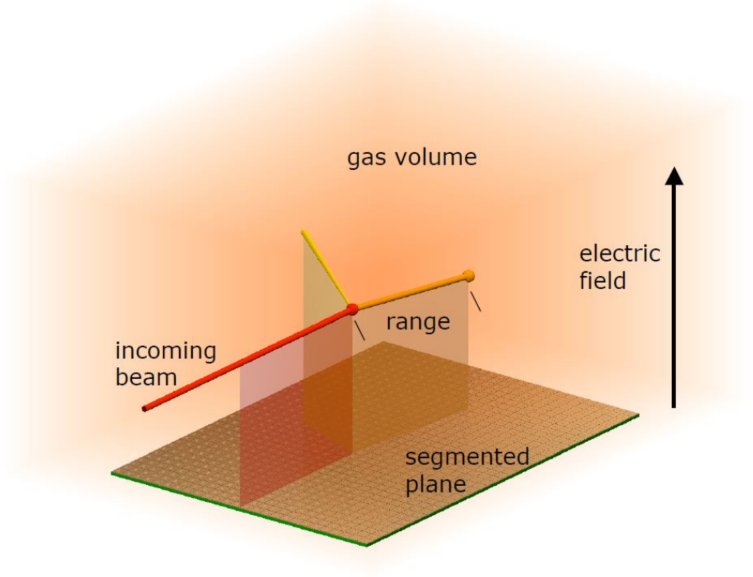

Figure 1.8: Working principle of an active target. The beam and the charged reaction products ionise the target gas (in orange). An electric field is applied, and the electrons drift towards an amplification stage. The recorded signal on a segmented readout plane enable the reconstruction of the tracks. The figure is taken from [46].

can promote an electron to an atomic orbit of higher energy (excitation) or remove it from the atomic nucleus (ionisation) at the expenses of the kinetic energy of the heavy ion [35]. In the first case the produced excited atoms quickly de-excites back to the ground state, while in the second case ion-electron pairs have a natural tendency to recombine in neutral atoms.

The interaction occurs simultaneously with several electrons of the medium and thus the charged particle loses energy gradually and is continually slowing down as it travels through matter. The maximum energy that can be transferred in a interaction from a charged particle of mass M with kinetic energy E to an electron of mass m_e (assumed to be at rest for simplicity) is during an elastic head-on collision. The value can be obtained by momentum and energy conservation and it is $\Delta E = 4E(\frac{m_e}{M})$. Because this is a small fraction of the total energy ($\frac{\Delta E}{E} \sim \frac{m_e}{M} << 1$), several thousands of collisions are needed for a heavy ion to lose its entire kinetic energy.

If the electrons produced by collisions have sufficient energy ($\sim$ keV), they can themselves ionise the atoms of the matter they cross and create further ions, producing secondary electrons (the ionisation energy of the medium is of the order of 10 eV). The distance traveled by these electrons is small with respect to the range of the heavy charged particle, therefore ionisation is produced along the track of the incoming particle with branches close to it. The primary and secondary electrons, as well as the atomic excitations, should be considered to determine the total amount of energy lost by the particle in the matter.

Except at its very end, the heavy ion trajectory in the material is only minimally altered by the interaction processes and tends to be quite straight in absence of a magnetic field. This happens because the particle is not heavily deflected by the single interactions, which occur in all directions simultaneously. Therefore the distance that a charged particle can travel in a given material before losing all of its energy is characteristic and it is called range of the particle. It depends on the material, the particle type and its energy.

The collision processes can be studied by a calculation which takes into account the quantum effects. The particle energy loss per unit path length within the absorber material, called stopping power, is

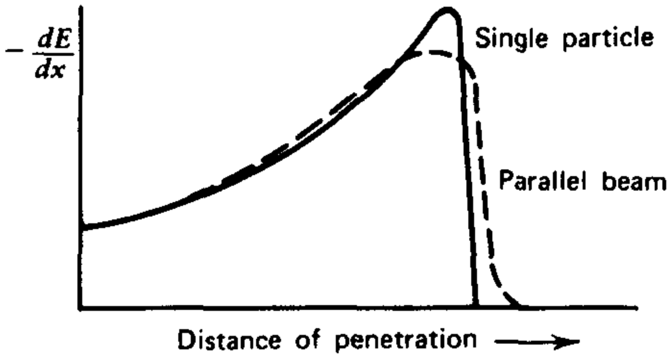

Figure 1.9: Bragg curve for an alpha particle of several MeV initial energy. The image is taken from Fig. 2.2 of [35]. The solid curve refers to a single alpha particle track while the dashed one to the average behavior of a parallel beam of alpha particles of the same initial energy crossing a material.

described by the Bethe-Bloch formula [35]:

$$S = -\frac{dE}{dx} = \frac{4\pi e^4 z^2}{m_0 v^2} NZ \left[ln \frac{2m_0 v^2}{I} - ln\left(1 - \frac{v^2}{c^2}\right) - \frac{v^2}{c^2} \right] \tag{1.11}$$

where m_0 and e are the mass and the charge of the electron, v and ze are the velocity and the electric charge of the incident particle and Z and N are the atomic number and the number density of the medium. I is the mean ionisation energy of the medium and it is treated as an empirical constant, experimentally determined for each element.

The graph of the energy loss as a function of the distance through the absorber medium is called the Bragg Curve and it is shown in Fig. 1.9. It has a characteristic shape, with a peak near the end of the track of the charged particle, just before it stops. For most of the track, the charge of the particle remains unchanged and the specific energy loss increases according to the 1/E. This is a consequence of the $\frac{1}{v^2}$ dependency of the stopping power. Indeed, when the charged particle velocity is low, the particle spends more time close to the electron. Therefore the impulse felt by the electron, and hence the energy transfer during the interaction, is larger. Near the end of the track, the charge is reduced through electron pickup and the curve falls off.

For a given material, the Bragg curve for a parallel beam of particles with the same initial energy can differ with respect to the Bragg curve for a single particle of the same type. This variation is due to the effect of straggling, caused by the statistical nature of the energy loss process.

1.2.5 Interaction of γ-rays with matter

The reaction products are often produced in an excited state and emit γ-rays to reach their ground state. The detection of photons and the reconstruction of their energy allows to study the structure of the populated nuclei and to obtain the total cross section for the production of a nucleus and the cross section for the population of the excited levels. Detectors with high γ-ray efficiency and with high resolution are important for the gamma-spectroscopy measurements.

The three main mechanisms through which the γ-radiation interacts with matter are photoelectric effect, Compton scattering and pair production.

The photons are much more penetrating with respect to the charged particles in matter. This is due to the much smaller interaction cross section of the γ-rays with respect to the interaction cross section of charged particles which undergo inelastic electron collisions. In contrast to heavy charged particles, which lose gradually their energy through continuous and simultaneous interactions with atoms of the matter they cross, X-rays and γ-rays undergo to a net variation of their history. If a beam of heavy charge particles passes through a slab of material of thickness t that is less than the particles range, the number of particles does not change but their energy decreases. Instead, when considering a incident mononergetic and high collimated photon beam, the intensity of the beam is attenuated, while the energy of γ-rays does not change. Indeed, in all the processes, the γ-rays transfer their energy (completely or partially) to the electrons of the medium, leading in sudden and 'catastrophic' change in the photon history. If the photon interacts with matter either it is entirely absorbed and disappears through the photoelectric or pair production mechanisms or it is scattered, possibly under a very large angle, after the Compton scattering. Thus if the photon interacts with matter it is removed from the beam entirely and the photons which pass straight through are those which have not suffered any interactions at all. They therefore retain their original energy. The fractional loss in intensity suffered by a photon beam as it passes through a thickness dt of material is:

$$\frac{dI}{I} = -\mu dt \tag{1.12}$$

and the intensity attenuation is exponential with respect to the material thickness:

$$I(t) = I_0 e^{-\mu t} \tag{1.13}$$

with I_0 is the incident beam intensity, t the thickness of absorber and μ the absorption coefficient.

The 'linear attenuation coefficient' μ is the total probability per unit length in the absorber that the gamma ray is removed from the beam and corresponds to the sum of the respective probabilities for the three main interaction processes, photoelectric absorption τ, Compton scattering σ and pair production k:

$$\mu(total) = \tau(photoelectric) + \sigma(Compton) + k(pair) \tag{1.14}$$

This quantity is characteristic of the absorbing material and is directly related to the total interaction cross-section.

Photoelectric effect

In the photoelectric absorption process, the incident photon (X-ray or γ-ray) with energy $h\nu$, being h the Planck's constant and ν its frequency, interacts with an atom of the medium, which absorbs it. As result a photoelectron is emitted from one of the atomic shells (usually one of the innermost ones) with kinetic energy E_{e^-}:

$$E_{e^-} = h\nu - E_b \tag{1.15}$$

where E_b is the binding energy of the photoelectron in the atomic shell. For energies of more than few hundred of keV, the photoelectron acquires the majority of the original γ-ray energy and E_b can be neglected. Therefore, if no electrons escape from the detection volume, the energy value of the incident γ-ray will results in a monoenergetic photopeak in the energy spectrum of the detector. After the emission of the electron, the ionised atom remains with a vacancy in one of its shells. The atom quickly fills the vacancy by capturing a free electron from the medium and/or rearranging the electron configuration in the shells. Because of this, one or more characteristic X-ray photons can be produced. The X-rays can then be re-absorbed or migrate and eventually escape from the detection medium. It is also possible that the emission of an Auger electron substitutes the X-ray emission. In a detection system these processes can influence the detector response.

The photoelectric effect dominates for gamma rays of relatively low-energy ($\sim$ 100 keV). Beside a single analytic formula do not exists, its probability P increases rapidly with the atomic number Z of the absorber medium and decreases rapidly when the photon energy E_γ increase.

$$P \propto \frac{Z^n}{E_\gamma^{3.5}} \tag{1.16}$$

In this approximation, the exponent n varies between 4 and 5 (Ref. [35]).

Compton scattering

In this interaction process, the incoming photon undergoes an elastic scattering with a quasi-free electron of the absorber medium. The electrons, that are bound in matter, can be considered as essentially free if the photon energy is high with respect to the binding energy. This is a good approximation when considering the orbital energies of the loosely bound outer atomic electrons.

The γ-ray transfers part of its energy to the electron (initially assumed to be at rest), then called recoil electron, and it is scattered through an angle θ with respect to its original direction, resulting in a scattered and less energetic photon of energy, $h\nu'$:

$$h\nu' = \frac{h\nu}{1 + \frac{h\nu}{m_e c^2}(1 - cos(\theta))} \tag{1.17}$$

where m_e is the rest mass energy of the electron (0.511 MeV). The relation is obtained by applying energy and momentum conservation laws.

The Klein-Nishina formula (eq. 2.18 in [35]) for the differential scattering cross section describes the angular distribution of scattered photons. It describes the preference for forward scattering at high energy values of gamma-rays. If the scattered γ-ray does not suffer another interaction in the scintillator material, it is possible for it to escape so that only a part of its energy is deposited in the detector and it is not possible to reconstruct the total energy of the incident γ-ray. The amount of energy deposited in the detector depends on the scattering angle of the photon, that can vary between 0° and 180°, and appears as a a Compton continuum in the gamma energy spectrum. The highest energy that can be deposited by the incident photon in a single collision, corresponding to full back-scatter, is called the Compton edge. Multi-Compton scattering for a single photon can also influence the energy spectrum, generating counts also between the Compton edge and the full energy peak.

The Compton scattering is the predominant type of γ-interaction in the range of energy (1-5 MeV) and its probability P increases linearly with the atomic number Z of the atoms of the medium.

Pair Production

If the energy of the incident photon exceeds twice the rest mass energy of an electron (1.022 MeV), it is energetically possible its annihilation. The energy is converted into mass, resulting in the production of an electron-positron pair. The conservation of linear momentum requires the presence of a third body, a massive atomic nuclues, which takes up the balance of the momentum in the form of a recoil. Any excess energy of the pair-producing gamma-ray is then shared by the electron and the positron as kinetic energy T_{e^+} and T_{e^-} (by considering the recoil energy negligible):

$$h\nu = T_{e^+} + m_{e^+}c^2 + T_{e^-} + m_{e^-}c^2 \tag{1.18}$$

The subsequent annihilation of the positron by reaction with an electron of the detector material produce the emission of two photons of 0.511 MeV each, created as secondary products of the interaction. These photons can then escape from the detector volume causing the 1.02 MeV of the incoming energy to be not detected. In the photons energy spectrum this results in a peak, called 'double escape peak' that appear 1.02 MeV before the photopeak. The same can occur if only one

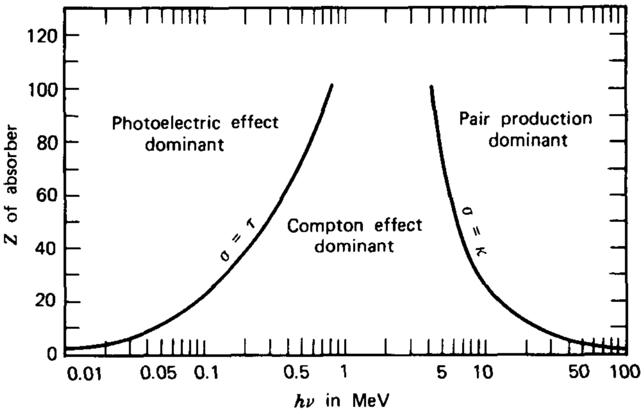

Figure 1.10: Regions of dominance of the three major types of γ-rays interactions. The black lines show the values of Z and E_γ for which the two neighboring interactions are equally probable. The figure is taken from Fig. 1.1 of Chapter 25 in [51].

annihilation photon escapes from the detector, causing the emergence of a 'single escape peak' 0.511 MeV before the full-energy peak.

Pair production is the most dominant process for photons of energy larger than 5 MeV. Its probability P increases approximately with the square of the atomic number of the absorber medium.

As shown in Fig. 1.10, the interaction probability of these processes depends both on the energy of the incoming γ radiation E_γ and on the atomic number Z of the atoms in the medium. In order to make an efficient detector for gamma rays, and capable to reconstruct the photons energy, materials in which the photoelectric and pair production cross sections are large compared to the Compton scattering cross section, are usually used. This allows to avoid too many Compton scatterings with escaping photons. Because of this, materials with high Z are more suitable for γ-rays detection. If scintillation detector are considered, inorganic materials offer the best performances.

1.2.6 Scintillators

Scintillators are materials that convert the high energy of the incoming radiation to a near visible or visible light through the excitation of electrons between molecular or atomic states. They can be gaseous, liquid or solid crystals, and can be divided in organic and inorganic. Each kind of detector has its own advantages and is employed for specific applications. The number of light photons created in a scintillator is proportional to the energy deposited by the particle in the material. To convert the light back to electrons, collect them and amplify the signal, a device that keeps the linearity, making it suitable to measure the energy of the incoming radiation, such as a photomultiplier tube (PMT) or silicon photomultiplier (SiPM), is used.

In addition to *linearity*, important general characteristics of scintillator detectors are:

- *Fast Time Response*: it allows timing information, such as determining the arrival time of an event in the detector and the time difference between two events with great precision. This and the fast recovery (low dead time) also permit scintillation detectors to accept higher counting rates.
- *Pulse Shape Discrimination*: it is a technique used to distinguish between different types of particles by analyzing the shape of the emitted light signals. This is possible because for some scintillator materials the light-emission process differs depending on the type of incoming radiation.

As in this thesis work the scintillators have been used to detect gamma-rays, the focus of this section will be on inorganic scintillators. Indeed, as mentioned in the previous section, to detect γ-rays with a reasonable efficiency, high-Z materials, such as inorganic crystals, are the most favored. Organic detectors, with low-Z material, are instead rather insensitive to the photons.

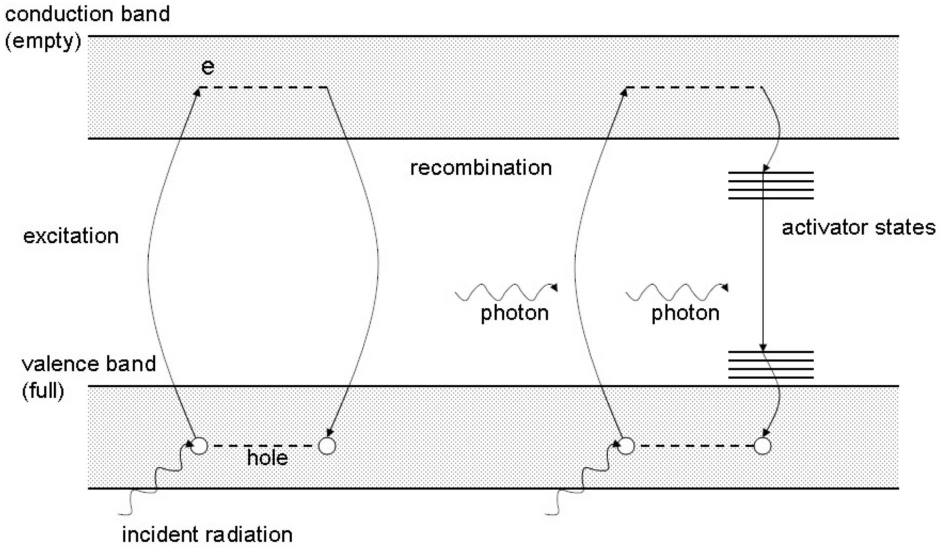

Figure 1.11: Energy bands in a crystal. On the left the emission process in a pure crystal is shown, while on the right it is the scintillation mechanism in presence of activators. The figure is based on Fig.7.16 of Ref. [11].

The scintillation mechanism in inorganic materials depends on the structure of the electronic bands on the crystal lattice. A schematic view is shown in Fig. 1.11. In crystal lattices, the electrons of the outermost atomic orbits (valence electrons) are responsible for the formation of electronic bands. The most important bands, involved in chemical bonding and electrical conductivity, are the *valence band* and the *conduction band*. In an insulating or semiconductor pure inorganic crystal lattice, the valence band represents the states, that are generally full and with electrons that are essentially bound at lattice sites, while the conduction-band represents states usually empty and with electrons that have sufficient energy to move in the crystal. An incoming radiation can excite an electron across the energy gap, a intermediate energy region forbidden in the pure crystal, to the conduction band. A hole in the valence band is generated by the missing electron. However, the electron can eventually lose energy and drops back to the valence band by emitting a γ-ray. This is an inefficient process that has to be limited. In order to enhance the probability of emitting photons and to reduce its self-absorption, small amounts of atoms of impurities (called activators) are commonly added to the scintillation material. The usual notation used is for example NaI(Tl) where NaI is the sodium iodide crystal and Tl is the thallium impurity. The activator generates states in the energy gap, the forbidden energy band in the pure crystal. This allows the light emission through the de-excitation of electrons to takes place between the activator states, causing a shift in the wavelength of the maximum γ-ray transition (with the energy corresponding to the gap energy between valence and conduction bands) and determining the emission spectrum of the scintillator.

The response in light output (number of photons per MeV gamma) is governed by the luminescence mechanism, the process governing the energy absorption and the subsequent re-emission in the form of visible light. If re-emission process occurs within 10^{-8} s (roughly the time taken for atomic transitions), it results in a fast component of the light signal. This is called 'fluorescence' mechanism. If the excited state is metastable and the re-emission is therefore delayed (with times that can vary from a few microseconds to hours depending on the material) it appears as the slow component of the signal. This process is called 'phosphorescence'. The light output of most scintillators is a function of temperature. This is caused by the fact that in scintillation crystals, radiative transitions, responsible for the production of scintillation light, compete with non-radiative transitions (no light production).

Some important and widely used inorganic scintillators are NaI(Tl), LaBr3(Ce), CsI(Tl), CsI(Na), BaF_2 and Bismuth Germanate (BGO). The latter has a not so good energy resolution but a high efficiency, that makes it suitable to be used as anti-Compton shields. BGO crystals can be situated around a main detector to intercept those γ-rays which undergo Compton scattering in the main detector and do not lose all of their energy in the material. Those events are then eliminated from the analysis, cleaning up the γ-ray spectra. This technique is typically used if energy information of the radiation is desired and the requirement is that the particle must deposit all of its energy rather than just part of it.

In addition to the possible detection processes mentioned above, that can take place inside a detector, influencing its energy response and the energy spectrum that can be obtained, there is the sum-peak mechanism. It is based on the fact that coincident γ rays can deposit their energy in the same detector almost simultaneously, and can be thus considered as part of the same event, creating a sum peak in the energy spectrum. For example the ~1172 keV and ~1332 keV γ rays emitted in the ^{60}Co decay can be detected as a sum peak at ~2.5 MeV.

Doppler broadening

Often, in experiments with radioactive beams, it is needed to consider the high velocities of the recoil nuclei emitting gammas (especially in inverse kinematics reactions). Indeed, after the reactions take place in the target, if the emerging nuclei are produced in excited states, they will emit gamma radiation to de-excite to the ground state. If the photons are emitted in-flight and then detected, according to the Doppler effect, they undergo a shift in energy:

$$E_\gamma = E_\gamma^0 \frac{\sqrt{1-\beta^2}}{1-\beta cos\theta} \approx E_\gamma^0(1+\beta cos\theta) \tag{1.19}$$

where E_γ is the measured energy in the laboratory, E_γ^0 is the energy of the emitted γ ray in the frame of the recoil, $\beta = \frac{v}{c}$ where v is the velocity of the moving nucleus and c is the speed of light in vacuum and θ is the angle between the velocity vector of the recoil nucleus and the direction of the emitted γ-ray in the laboratory.

Together with the energy shift, the Doppler effect causes a broadening of the peak and a worsening of the energy resolution of the detectors. The contributions to the Doppler broadening arise from the opening angle of the detectors, from the angular spread of the recoils and from the velocity (energy) variation of the recoils. To improve the resolution, the Doppler correction by the kinematic reconstruction of the reaction is needed. To achieve a better energy resolution, especially for γ-rays emitted by nuclei with very high velocities (10-50% of the speed of light) the detectors employed in the detection should subtend a small angle. This can be obtained with high granularity segmentation detectors.

AddBack procedure

When an array of scintillators is employed in experiments, it could happen that a single photon releases its energy in more than one crystal. For example it can undergo multiple Compton scatterings or after pair production one or both annihilation photons can escape from a detector and be detected in a nearby one. To recover the full energy peak for these events, the add-back procedure, that consists in checking the surrounding detectors when a detector provides a signal for an event, is used in the analysis. It allows to adds the energies back together (hence the name of this method). There are different parameters that must be chosen for the energy reconstruction as the add-back radius, the maximum distance between two different crystals, and the maximum number of crystals to be used for the reconstruction.

1.3 Reaction processes

During in-beam experiments, from the collision of two nuclei commonly several different reactions take place and as a result many and distinct types of particles are produced. The analysis of the data acquired by the detectors is needed to identify the reaction products and select the reaction channel of interest. In this chapter, after an overview of the possible types of nuclear reactions, the theory that allows to describe transfer reactions will be presented.

1.3.1 Nuclear reactions

A typical 2-body nuclear reaction can be written:

$$\mathrm{a} + \mathrm{A} \rightarrow \mathrm{b} + \mathrm{B} \tag{1.20}$$

where a is the accelerated particle, called *projectile*, A is the *target* nucleus (usually at rest in the laboratory system), while b and B are the reaction products, called respectively *ejectile* (typically the lighter one) and *recoil.* A more compact way to refer to a nuclear reaction is:

$$\mathrm{A(a,\ b)B} \tag{1.21}$$

which allows to describe a general class of reaction with common proprieties, for example the (d, p) stripping reaction or the (n, γ) neutron radiative capture reaction.

Nuclear reactions can be classified according to the rearrangement of nucleons in or between the particles of a given a entrance channel (a + A), i.e. on the possible combinations of the particles in the exit channel.
If in the collision there is no exchange of nucleons between the projectile and the target nuclei and hence the incoming and outgoing particles are the same, the process is called *scattering.* If all the nuclei are populated in their ground states and only their trajectories are altered, the reaction can be written a + A → a + A and this is named *elastic* scattering. If one nucleus is excited from its ground to a higher-lying energy state, the reaction a + A → a + A* is instead an *inelastic* scattering. Usually the nucleus in the exited state will then decay quickly by γ emission.
Reactions in which one or more nucleons are exchanged between the projectile and the target nuclei are called *transfer reactions. Stripping* reactions are referred to the processes in which nucleons are transferred from the projectile to the target nucleus, while in *pickup* reactions nucleons are transferred from the target to the projectile. An example of a transfer reaction is the $\alpha(^{86}\mathrm{Kr},^{3}\mathrm{He})^{87}\mathrm{Kr}$, a neutron pickup reaction, subject of this thesis. Other reactions that can occur are *break-up*, when the projectile is split into two or more parts by the interaction (as this is not a binary reaction) and the *knock-out* reaction, when the projectile removes one nucleon or a light cluster from the target.

A different classification of reactions is related to the mechanism that governs the nuclear reaction processes.
Nuclear reactions that occur very rapidly, in a time of the order of 10^{-22}s [11] in peripheral collisions with one-step interactions, are called *direct reactions.* In direct reactions (of which transfer reactions are a subclass) only very few nucleons, located mainly on the surface of the studied nucleus, are involved in the reaction and the transition from the entrance to the exit channel is immediate. These reactions allow to populate states by adding or removing a single nucleon from a nucleus and can be used to investigate the shell configuration of nuclei. The outcome depends on the entrance channel. The cross section of the exit channel b + B strongly depends on the overlap of the initial and final wave functions and the angular distributions of the reaction ejectiles has a pronounced shape that is related to the transferred orbital angular momentum of the system. This makes direct reactions a useful technique to explore the nuclear structure.
On the other hand there are the *capture reactions* in which the incoming particle and target nucleus fuse together to form a compound nucleus and the absorbed energy is distributed over all nucleons.

The time scale of these processes varies from 10^{-16} to 10^{-18} s [11]. The compound nucleus then decays by particle or radiative emission. In this case, the emitted particles lose all the information of the entrance channel A + a by which the compound nucleus was formed and the resulting angular distribution will in general be isotropic in the center of mass. A subclass of capture reaction are fusion-evaporation reactions. A compound nucleus in a highly excited state and high angular momentum is produced by the collision between heavy nuclei. After the collision, the produced compound nucleus is rapidly rotating and de-excites by "evaporating", i.e. emitting light particles. When the excitation energy of the residual nuclei is below the particles separation energy, these nuclei de-excite by γ rays emission until they reach their ground states.

The amount of energy that is required by the reaction to take place or released in the process is called the reaction Q-value and is defined as the initial mass energy minus the final mass energy of the system. It corresponds to the excess of kinetic energy of the final products [11]:

$$Q = [(m_A + m_a) - (m_B + m_b)]c^2 = T_{final} - T_{initial} \tag{1.22}$$

where m_A, m_a, m_B and m_b are the masses of the nuclei while $T_{initial}$ and T_{final} are the kinetic energies of the initial and final particles. If Q is positive the reaction is said to be *exothermic* and the binding energy is converted into kinetic energy of the final reaction products. If Q is negative the reaction is called *endothermic* and and a minimal amount of kinetic energy in the entrance channel is needed to initiate the reaction. If one of the particles in the exit channel is produced in an excited state, the Q-value of the reaction has to include the excitation energy of the state above the ground state E_{ex}:

$$Q_{ex} = Q_0 - E_{ex} \tag{1.23}$$

where Q_0 is the Q-value for the reaction with all particles in their ground states.

1.3.2 Cross section

The interaction between the projectile and target particles is generally described in terms of the cross section σ, which is a measure of the probability for a reaction to occur. The total cross section σ_{tot} is the sum of the cross sections of all the different nuclear processes (elastic scattering, inelastic excitations, nucleon transfer, fusion, ...) that can take place:

$$\sigma_{tot} = \sigma_{el} + \sigma_{inel} + \sigma_{transfer} + \sigma_{fusion} + .. \tag{1.24}$$

By considering a collision between a beam of N_a projectile particles and a target with N_A particles per unit of area, the number of interactions per unit of time dN_a/dt, i.e. the reaction production rate R is:

$$R = \frac{dN_a}{dt} = \sigma N_A I_a \tag{1.25}$$

where I_a is the intensity of the beam and the reaction cross section σ is the constant of proportionality between R and the luminosity, the product $I_a N_A$.

The cross section represents the area where the projectile and the target particles interact. It has indeed a dimension of an area and is usually measured in fractions of barn: 1 barn = $10^{-28} m^2$.

The cross sections (either total or for individual processes) generally depend on the bombarding energy and, in non-relativistic mechanics, are not affected by transformation between the center-of-mass and the laboratory frame of reference. They are scalar quantities.

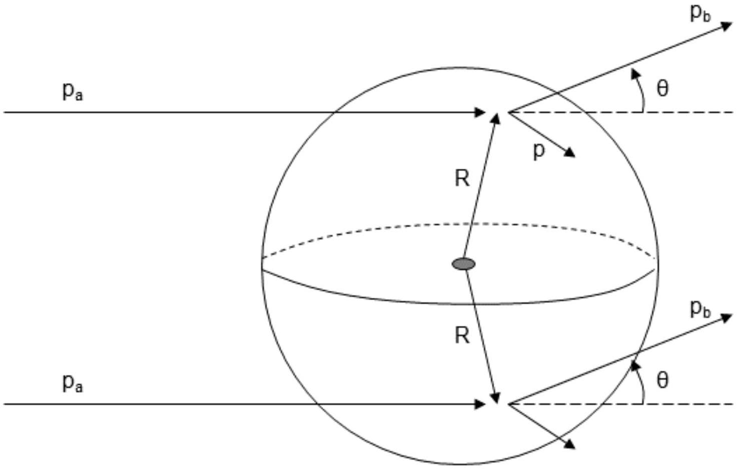

Figure 1.12: Schematic view of a direct reaction. R is the nuclear radius. The figure is based on Fig. 11.22 of Ref. [11].

The detectors used in experiments generally cover only a fraction $\Delta\Omega$ of the whole solid angle and thus intercept only a portion $\mathrm{dR}_{reaction}$ of the total flux of the emitted particles. The value that can be obtained in the experiments is the differential cross section $d\sigma$. It depends on the emission angle, which can be described by the polar θ and the azimuthal ϕ angles with respect to the beam direction. In general, the angular distribution $r(\theta,\phi)$ of the scattered particles is not isotropic, i.e. the outgoing particles will not be emitted uniformly in all directions.

The differential cross section is not an invariant quantity and changes according to the reference frame. It can be defined as:

$$\frac{d\sigma(\theta,\phi)}{d\Omega}d\Omega = \frac{r(\theta,\phi)}{I_a N_A} \tag{1.26}$$

The total cross section can be then be obtained by the integral over the full solid angle:

$$\sigma_{tot} = \int \frac{d\sigma}{d\Omega}d\Omega = \int_0^{\pi} sin\theta d\theta \int_0^{2\pi} \frac{d\sigma}{d\Omega}d\phi \tag{1.27}$$

where in spherical coordinates $d\Omega = sin\theta d\theta d\phi$.

1.3.3 Transfer reactions

One-nucleon transfer reactions favour transitions corresponding to single-particle degrees of freedom and are very useful for the study of low-lying shell-model excited states.

For a particular reaction, in the collision between the ion beam and the target, several states of the same isotope can be populated. From the energy and angular distribution of the light particles it is possible to deduce the excitation energies of populated levels and obtain spins and parities of the shell model states. Angular distributions therefore are of critical importance in studies of transfer reactions. In the following paragraphs the relation between the angular distribution and the transferred momentum l that allows to assign spin and parity to the populated state is deduced.

Fig. 1.12 is a schematic view of a direct transfer reaction in direct kinematics, with the incoming light particle colliding with a heavy target nucleus.

p_a and p_b are respectively the momentum of the incident particle and the momentum of the scattered one, while $p = p_a$ - p_b is the recoil momentum of the residual nucleus.

In a direct process, it is assumed that the transferred nucleon instantaneously has the recoil momentum. By assuming that the interaction occurs at the surface of the nucleus, the transferred angular momentum is L = Rp and thus $\hbar\,\sqrt{l(l+1)} \approx$ Rp. After the reaction the nucleon will be allocated to an orbit with orbital angular momentum l.

From the momentum conservation in the reaction, one can relate the orbital angular momentum l with the momentum p transferred to the recoil nucleus in the reaction. Let θ be the angle between p_a and p_b, the momentum vectors are connected by the law of cosines:

$$p^2 = p_a^2 + p_b^2 - 2p_a p_b(\cos\theta) = (p_a - p_b)^2 + 2p_a p_b(1-\cos\theta) = (p_a - p_b)^2 + 4p_a p_b \sin^2(\frac{\theta}{2}) \tag{1.28}$$

The following relation is thus obtained:

$$l(l+1) \approx \frac{R^2}{\hbar^2}[(p_a - p_b)^2 + 4p_a p_b \sin^2(\frac{\theta}{2})] \tag{1.29}$$

From these simple semi-classical considerations it is evident that it is possible to infer the state populated in the reaction, i.e. the orbital to which the neutron has been transferred, by knowing the energy of the incident particle and by measuring the angle θ and the momenta of the ejectile particles. In other words, the populated state in the recoil can be identified from the shape of the differential cross section curve. The angular distribution shows maxima and minima that are typical of an interference phenomenon between scatterings that take place at the opposite sides of the nucleus, as can be observed in Fig. 1.12. This simple estimate changes by considering also the intrinsic spins of the particles, which was neglected in the previous discussion. If the initial state of the target nucleus is 0^+ and the orbital angular momentum transferred is l, the final nuclear states that can be populated are the ones with total angular momentum j=l$\pm\frac{1}{2}$, where $\frac{1}{2}$ is the intrinsic spin of the transferred nucleon. Moreover, the angular momentum transferred in the reaction provides information on the change in parity occurred, if l = even there is no change in parity while if l = odd there is a change in parity. This allows to assign parity π to the populated state. The parity of the final state can indeed be obtained with $\pi = \pi_a \pi_A (-1)^l$ where π_a and π_A are the parities of the nuclei in the entrance channel (where A is the target nucleus, see eq. 1.20). For example if the momentum transfer is $l = 2$ the states that can be populated are the ones with total angular momentum j=$\frac{3}{2}^+$ or $\frac{5}{2}^+$.

Figure 1.13 shows a simplified general two-body reaction A(a,b)B represented in the laboratory frame, where the target nucleus is assumed at rest. The reaction plane is defined by the direction of the projectile and of one of the two outgoing particles. Because of the conservation of the perpendicular component of momentum, with respect to the reaction plane, the motion of the second particle in the exit channel must lie in the same plane. In this work only non-relativistic kinematics have been studied because the energy of beam delivered at ISOLDE/CERN is limited to ∼ 10 MeV/u. Only the non-relativistic case will be treated in thee following paragraphs.

The kinematic relations can be derived from the principles of conservation of energy and linear momentum:

$$\mathrm{T}_a + \mathrm{Q} = \mathrm{T}_B + \mathrm{T}_b \tag{1.30}$$

$$p_a = p_b\cos\theta + p_B\cos\xi \qquad \text{(axis parallel to the beam)} \tag{1.31}$$

$$0 = p_b\sin\theta - p_B\sin\xi \qquad \text{(axis perpendicular to the beam)} \tag{1.32}$$

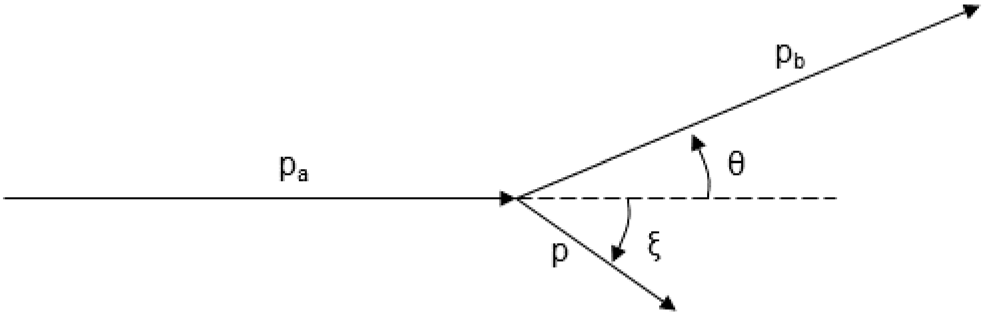

Figure 1.13: Schematic view of a 2-body reaction.

where Q is the Q-value of the reaction, T_a, p_a are the kinetic energy and the momenta of the particles in the entrance channel (T_A=0 because the nucleus is assumed to be at rest), T_b, T_B, p_b and p_B are the corresponding values for the particles in the exit channel. θ and ξ are the angles between the momentum vectors, as represented in figure. If the heavy reaction product is produced in an exited state, the excitation energy $E_{ex,B}$ has to be added in eq. 1.30.

By detecting the light ejectiles it is possible to obtain the scattering angle θ. The knowledge of the Q-value of the reaction and the energy of the beam, and thus T_a, allows to obtain the value T_b as a function of θ [11]:

$$\sqrt{T_b} = \frac{\sqrt{m_a m_b T_a} cos\theta \pm [m_a m_b T_a cos^2\theta + (m_B + m_b)[m_B Q + (m_B - m_a)T_a]]^{\frac{1}{2}}}{m_B + m_b} \tag{1.33}$$

In case Q<0 a minimum value of the energy (threshold energy) of the incident particles exists, below which it is not possible for the reaction to occur.

This threshold energy T_a^{th} is:

$$T_a^{th} = (-Q)\frac{m_B + m_b}{m_B + m_b - m_a} \tag{1.34}$$

This threshold corresponds to the case of $\theta = 0$ and consequently $\phi = 0$. The outgoing particles B and b have the same direction, even if they are two distinct objects. In this case no energy is spent giving transverse momentum to the two particles.

For Q>0 no threshold energy exists, the reaction can take place regardless of the incident energy.

From symmetry reasons the dynamics of reactions are most conveniently analysed in the center of mass frame of reference, which has its origin in the center of mass of the nuclei in the entrance channel and in which the total linear momentum of the reacting particles is zero. In order to compare theory and experiment a coordinate transformation of the observed properties of the reaction (energy, momentum and emission angle of the outgoing particles and the reaction cross sections) from the laboratory (L) to the center-of-mass (CM) reference frame is needed.

In the following relations CM $\longleftrightarrow$ L the values in the laboratory frame of reference are represented with unprimed symbols (ex. T_a) while the values in the CM frame with primed symbols (ex. T'_b).

The conservation of energy in the laboratory and center-of-mass frames gives the energy of the particle b in the CM frame [11]:

$$T'_b = \frac{m_b}{m_B + m_b}[Q + (1 - \frac{m_a}{m_B + m_b})T_a] \tag{1.35}$$

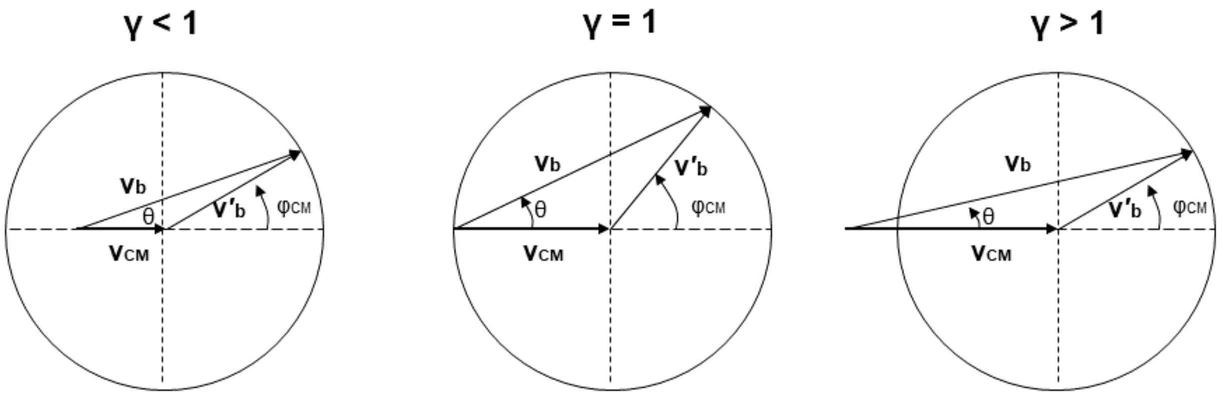

Figure 1.14: Kinematics of binary reactions

From the velocity and momentum composition, that can be obtained from the first picture on the left of Fig. 1.14, the following expressions can be derived:

$$\mathbf{v_b} = \mathbf{v_{CM}} + \mathbf{v'_b} \tag{1.36}$$

$$tan(\theta_{LAB}) = \frac{v'_b sin(\psi_{CM})}{v_{CM} + v'_B cos(\psi_{CM})} = \frac{sin(\psi_{CM})}{\gamma + cos(\psi_{CM})} \tag{1.37}$$

where v'_b is the velocity of the ejectile b in the centre-of-mass reference frame while v_{CM} is the velocity of the centre of mass of the system (in the laboratory frame) which direction is the same of the incoming particle a. θ is the scattering angle in the laboratory frame while ψ_{CM} is the corresponding in the CM reference frame. The expression for γ, the ratio between v_{CM} and v'_b can be found using conservation of energy and linear momentum [11]:

$$\gamma = \frac{v_{CM}}{v'_b} = \sqrt{\frac{m_a m_b}{m_A m_B} \frac{T_a}{T_a + Q(1 + \frac{m_a}{m_A})}} \tag{1.38}$$

According to the value of the parameter γ, there are three different kinematic cases: if $\gamma < 1$ the emission of the particle b in the laboratory can be at all angles. If $\gamma = 1$ the emission of b in the laboratory is limited between angles θ from 0° to 90°, while if $\gamma > 1$ the emission of the particle in the laboratory is confined in a forward cone. A graphical picture can be seen in Fig. 1.14.

A transfer reaction can occur in direct or inverse kinematics. While in direct kinematics a target of heavy isotopes is bombarded with light projectiles to induce reactions, in inverse kinematics ion beams of heavy isotopes are accelerated and collide to a target of light isotopes. In direct kinematics, the kinetic energy of the center of mass is small, indeed it is almost stationary at the target position. The energy of the system is instead mainly contained in the energy of the relative motion. In inverse kinematics reactions, the motion of the center of mass corresponds nearly to the motion of the heavy projectile and it contains most of the energy of the system. The heavy isotope produced in the exit channel takes most of the kinetic energy of the projectile nucleus and moves with small deviations from the beam axis. Light products instead can be emitted with much smaller energy and over 4π relative to the reaction vertex in the laboratory coordinate system, depending on the kinematics.

Chapter 2

Characterisation of SpecMAT

The SpecMAT active target (European project for Spectroscopy of exotic nuclei in a Magnetic Active Target) is a particle detector designed and built at KU Leuven for spectroscopy of nuclei far from the stability valley through direct nuclear reactions. As an active target, SpecMAT combines a high efficiency, due to the almost 4π coverage of the reaction vertex, and a good energy resolution. This makes active targets suitable for the detection of the light ejectiles of the nuclear reactions - p, d, t, ^{3}He or α-particles. The SpecMAT detector accommodate an array of $CeBr_3$ scintillators to detect γ-rays emitted in the de-exitation of the nuclei of interest produced in the reactions. SpecMAT is also optimized for operation in a strong homogeneous magnetic field. This allows particles identification based not only on the amount of energy left by the particles in the gas but also on the shape of their trajectories in the sensitive volume of the detector. For experiments with beam the detector will be moved to ISOLDE/CERN inside the ISOLDE Solenoidal Spectrometer (ISS). The combination of several detection techniques, charged particle detection in a high-luminosity active target in a strong magnetic field coupled to a gamma-ray spectrometer, makes SpecMAT an ideal tool for studies of the nuclear structure of exotic isotopes. This chapter is dedicated to the description of the components of the SpecMAT active target and to the characterisation measurements performed in this work.

2.1 The SpecMAT active target

As shown in Fig. 2.1 the active target of SpecMAT, delimited by the field cage, has a cylindrical structure. The length of the active target is 323.5 mm and the radius of the cylindrical shape is 110 mm [52]. To produce the nuclei of interest, a ion beam will be delivered to the TPC from REX/HIE-ISOLDE post-accelerator of ISOLDE. This ISOL facility at CERN is capable of delivering isotope beams at the energy up to $\sim$ 10 MeV/u [30]. As can be seen in Fig. 2.1 starting from the right, the beam will enter the gas chamber of the detector through a thin mylar film of $\sim 10\ \mu$m that separates the active volume from the beamline vacuum. This thickness allows the beam to enter in the gas chamber with a minimal loss of energy.

The field cage allows to generate the uniform electric field within the sensitive (or active) volume of the TPC. Particularly the field cage of SpecMAT has a double structure with two sets of coaxial electrodes (see [53] for details). The inner electrodes are used for generation of a homogeneous E-field in the detector, while the outer electrodes are used for minimisation of the electric field between the outer surface and the aluminium gas chamber.

The ions created along the ionisation tracks drift towards the cathode and they can recombine with free electrons in the gas during their path or, if they reach it, are collected at the cathode. The electrons drift towards a position-sensitive gaseous detector, the Micromegas (Micro Mesh Gaseous Structure) detector [54], divided in 2916 triangular pads (channels). The detector is located downstream and

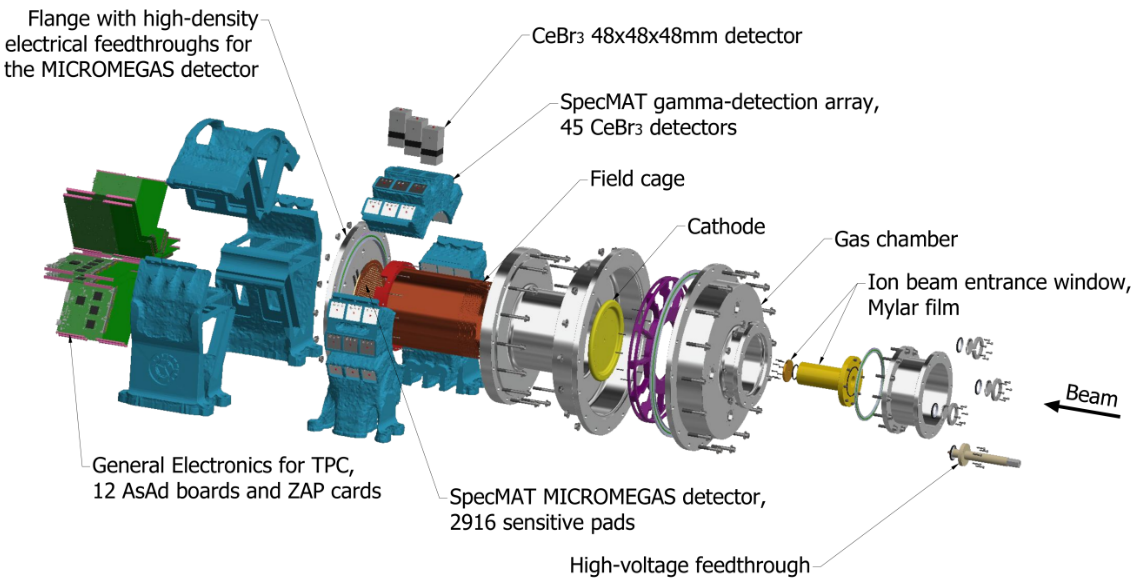

Figure 2.1: View of SpecMAT. Figure taken from Fig.1 of [53].

perpendicularly with respect to the direction of the beam. Each singular pad is an equilateral triangle with a height of 4.6 mm and the distance between pads is 125 μm. The total pad plane is divided into six sectors, with 486 pads each. The Micromegas detector is used for amplification of the signal of ionisation electrons. A mesh separates the main gas volume from the amplification gap, which has a length of only 128 μm (the distance between the mesh and the pad plane) and in which an high electric field is applied. The electron avalanche produced is then collected by the anode pads and the signal is sent to the electronics to be analysed. The detector has a hole of 8 mm in the center in the place of six pads that have been removed. This was done to allow the RIB to exit from the TPC volume and not to stop it in the Micromegas. In this way the implantation on the Micromegas of unwanted sources of radiation is avoided. Also, the saturation of the electronics due to the strong signal of the beam particles is prevented. The Micromegas detector allows to reconstruct the three-dimensional particle track. Its 2D orthogonal projection on the sensitive plane of the detector is reconstructed by the activated pads which collect ionisation electrons and the information on the 3rd dimension, along the beam, can be obtained from the timing intervals between the activated pads.

The electronic signals (from each individual pad) are then recorded by the data acquisition system (DAQ). Usually the data acquisition electronics of an active target is optimised to read only channels that have been activated in a reaction event, in order to reduce the data flow.

During experiments the gas in the active target is usually kept in the pressure range from ~100 mbar to atmospheric pressure. However, the gas chamber can sustain a high level of vacuum. The maximum level reached was $\sim 10^{-4}$ mbar, using a dry scroll pump [52].

The array of $CeBr_3$ scintillators is placed around the main part of the gas chamber, that contains the active volume of the TPC. The wall thickness of the chamber in this region is 3 mm and thus the attenuation of the γ-rays emitted from the reaction vertex inside the TPC toward the scintillation detectors is minimal. The array has three rings of detectors, with 15 crystals in each ring. During the characterisation measurements described in this thesis the scintillation array contained 39 detectors.

All detectors in the array are kept together by a 3D printed nylon support. A single scintillation detector is shown in Fig. 2.2. This detector contains a $CeBr_3$ crystal with dimensions 48x48x48 mm^3. Each crystal works in combination with a silicon photomultiplier (SiPM) that collects the scintillation photon and converts it in the electronic signal to be analysed. The SiPM contains a built-

Figure 2.2: The scintillation detector. Figure provided by Oleksii Poleshchuk.

in temperature compensated bias generator, a built-in pre-amplifier and requires +5 V of external bias for operation. When a scintillator detects an incident γ-ray, the SiPM produces two signals as response: an energy signal which is optimised for energy resolution and a fast signal optimised and used for timing resolution. The outer dimension of the detector are 55x55x110 mm^3. The thickness of the γ-ray entrance window is 1 mm and the side walls of the detector are 3 mm thick.

The $CeBr_3$ scintillators have a good energy resolution ($\sim$ 4% FWHM at $\sim$ 662 keV), high efficiency and low intrinsic activity. The crystals and the SiPMs are tolerant to external magnetic fields, which allows them to operate in a magnetic field without performance degradation. A prototype of this detector has been tested in a magnetic field [55]. This makes the $CeBr_3$ scintillators suitable to work in combination with the active target of SpecMAT to allows both gamma spectroscopy and charged particles detection in presence of a magnetic field.

2.2 GET electronics for SpecMAT

Both the Micromegas and scintillation array are read out with the General Electronics for TPCs (GET) [56]. GET is a generic electronics and data acquisition system developed for nuclear physics. GET can process data flow up to 33792 electronic channels. The GET design includes all the electronic systems from the front-end electronics for the acquisition of the data, to the processing and the storage of the data acquired. In Figure 2.3 a schematic representation of the GET electronics is illustrated.

The signals provided from the SpecMAT Micromegas pads are guided via ZAP boards to the front-end AsAd boards. The ZAP boards are protection circuit cards which preserve the AsAd boards from possible discharges, which may occur in the detector. The AsAd cards are the front-end electronics of the GET system and are based on a versatile Application Specific Integrated Circuit (ASIC) design, combined with an Analog-to-Digital Converter (ADC).

A photo of a SpecMAT ZAP connected to the AsAd board is presented in Fig. 2.4.

For a convenience of time correlation of the particle tracks acquired with the TPC and the γ-rays detected by the $CeBr_3$ crystals, both the Micromemgas Pad Plane and the scintillation array were read out with GET electronics. The interface between the scintillation array and the AsAd board is a custom designed adaptation board, used to introduce the DC offset to the input signal, required by the processing stages of the AsAd.

The AsAd board is constituted by four Asic chips (AGET). Each AGET contains 68 channels, four of which are FPN (Fixed-Pattern Noise) channels. This channels are used to determine the intrinsic noise level of the readout stage. The other 64 channel per AGET (256 for one AsAd board) process the

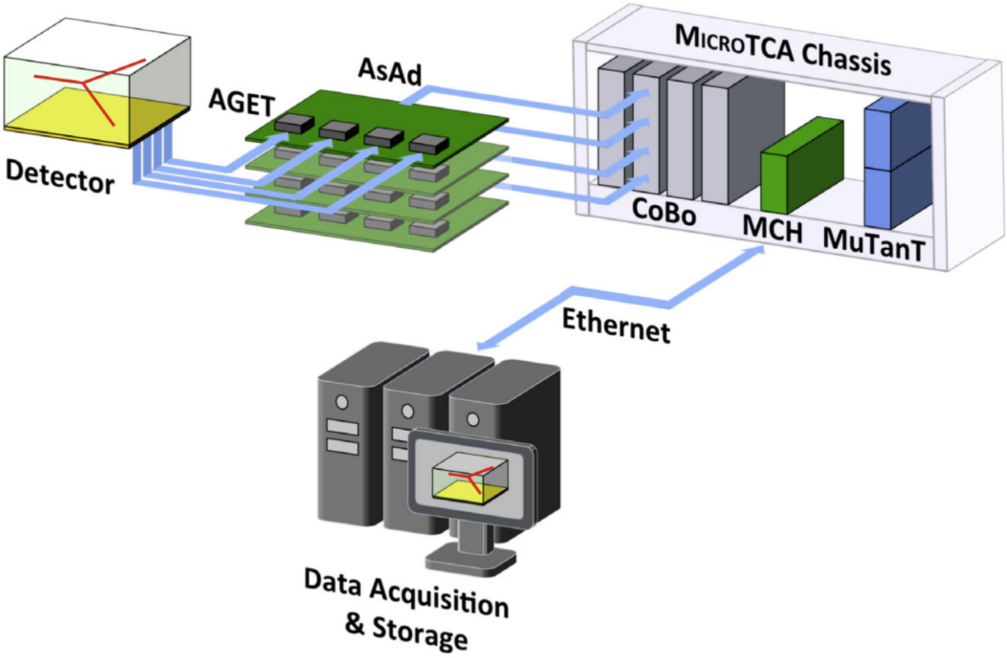

Figure 2.3: Schematic view of the GET electronics system. Figure taken from Fig.1 of reference [56].

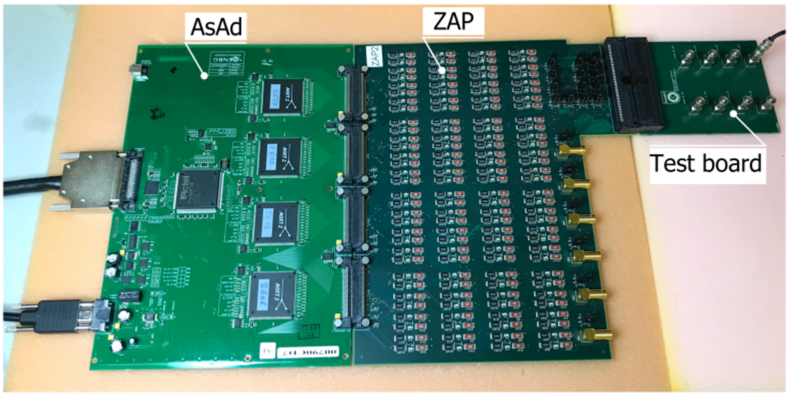

Figure 2.4: ZAP card and AsAd board for GET electronics. The figure is taken from Fig. 20 of [53].

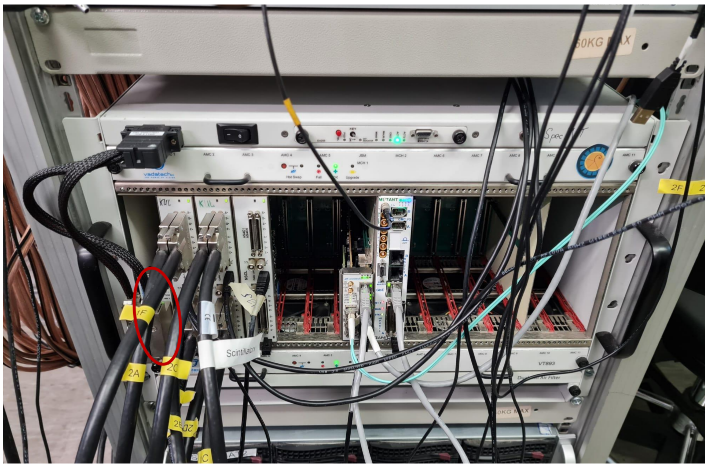

Figure 2.5: Modules housed in the MicroTCA crate. Starting from the left: power supply for the modules (highlighted with the red circle), 3 CoBos, a MCH (MicroTCA carrier hub, a network switch) and the MuTanT (Multiplicity Trigger and Time module).

signal of the detectors and deliver the data to an ADC (Analog to Digital Converter). Each channel is composed of a Charge-Sensitive pre-Amplifier (CSA) stage, an analog filter (to shape the signal) and an amplifier which inverts and amplifies the signal. The analog signal of each channel is sampled in time and stored in a Switch Capacitor Array (SCA). The SCA is a 512-cell deep circular buffer which has the memory function for the data acquired by the electronics. The memory is continuously written with data until an event is accepted.

The Micromegas Pad Plane of SpecMAT is divided into 6 sectors. Each sector is designed for readout with two AsAd boards. The array of scintillation crystals is coupled to a single AsAd card of the GET system. The AsAd board receives the data from the detectors, processes the signals through the AGET chips and stores the events information into the SCA analog memory. The data are then digitized through the ADC and guided to the Concentration Boards (CoBo) for further analysis.

The Concentration Board (CoBo) is an electronic module developed for the GET system to process the data. It is compatible with the MicroTCA (Micro Telecom Computing Architecture) chassis, a bus standard that allows to reduce cables and external point-to-point contacts between the electronic devices. The power supply is used to power the modules plugged in the MicroTCA crate. The information between the modules is transmitted via the back-plane of the chassis.

The back-end GET electronics used for the detector characterisation with the $HeCF_4$ gas mixture is shown in Fig. 2.5.

A single CoBo module can be connected to a maximum of 4 AsAd boards and thus processes data from a maximum of 1024 signal channels. The resulting hit-pattern of channels together with multiplicity values are sent to MuTanT (Multiplicity Trigger and Time module).

The trigger module through the MicroTCA backplane provides the CoBo with the Global Master Clock (GMC), which permits to synchronize the signals coming from the different modules. The clock frequencies can be changed to select the time/bin to be used.

The MuTanT module can manage three levels of triggers for the whole electronic system. It is possible to set manually as trigger an external signal, such as the signal detected by the scintillation array. In this case, when a γ-ray is recorded, the trigger gives input to start the data acquisition within the time window. The internal trigger is instead considered as set to the multiplicity values within the TPC itself (TPC multiplicity trigger). The trigger can also be based on the event pattern. Algorithms to select or reject specific events from the hit-pattern can be programmed.

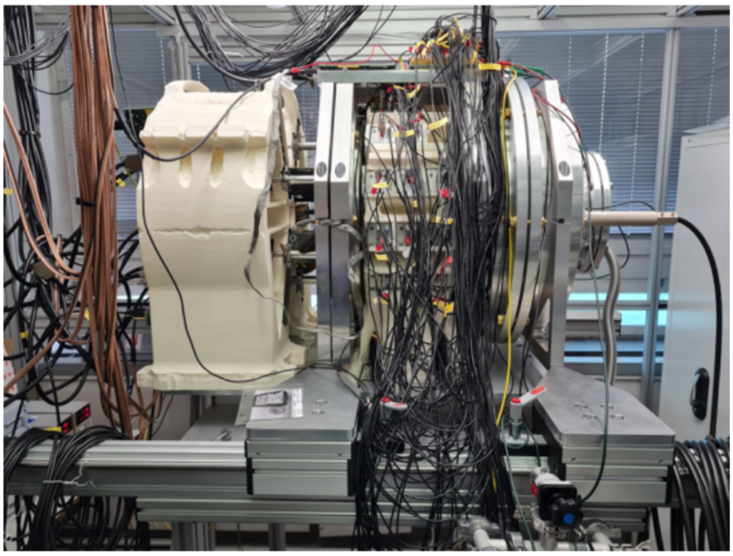

Figure 2.6: The assembled detector SpecMAT at KU Leuven.

When an event is accepted, the MuTanT module assigns the event number and the time stamp. This information is transmitted to all the CoBos connected to the electronic system and read out over the MicroTCA backplane. From the MicroTCA backplane the full event information is then transmitted to external computers for the off-line analysis.

In the future experiments with the beam at ISOLDE, in which SpecMAT will be used, the detector together with the AsAd and the ZAP boards will be placed in the magnetic field provided by ISS, that can provide a magnetic field up to ~2.5 T. The components are indeed insensitive to a strong magnetic field. Cables will then deliver the data acquired to the MicroTCA with Cobos, located outside ISS. In figure 2.6, the SpecMAT detector assembled at KU Leuven for the characterisation with a helium gas mixture, which is presented in the next section, is shown.

2.3 Characterisation of the detector

The goal behind this thesis work is to assess the viability of using SpecMAT to study the shell evolution along the neutron closed shell with N=50. To study the nuclear structure, reactions that add a neutron to the N=50 closed shell can be employed. By performing this reaction on nuclides with different proton numbers, the shell evolution can be studied systematically. This strategy will allow to explore the non-central component of the nuclear force, which takes into account the interaction between nucleons. In this work the structure of ^{87}Kr through the (α, ^{3}He) reaction is studied. Excited single-particle states in ^{87}Kr are populated in the transfer reaction by using a beam of ^{86}Kr on a He-filled gas target. This reaction uses a stable beam but can be extended to RIBs for the investigation of the nuclear structure of the other nuclides along N=50.

For the production of this transfer reaction, SpecMAT will be filled with helium gas, that will be used both as the target for nuclear reaction and as the detection medium for the charged particles emitted in the reaction (in our case ^{3}He). It is therefore important to characterise the detector in presence of helium gas, in preparation for the experiments with the beam. Knowing how SpecMAT performs in helium, it is possible to produce a realistic simulation of the $\alpha(^{86}\mathrm{Kr},^{3}\mathrm{He})^{87}\mathrm{Kr}$ transfer reaction inside the active target. This will show if the detector is suitable for the study of the nuclear structure of ^{87}Kr through this reaction in an experimental laboratory such as at ISOLDE/CERN.

The SpecMAT active target is a new experimental detector developed in recent years and for which the first characterisation measurements have been done only in 2021 [53] with a Ar(95%)CF_4(5%) gas mixture at 400 mbar. In this work SpecMAT has been characterised for the first time with a helium gas mixture He(98%)CF_4(2%). The results have been then compared with the ones obtained from the characterisation with the argon gas.

Usually the gas employed in the TPCs is not composed of a single gas but it is instead a mixture which contains a noble gas as the main component and few percentages of a quencher gas. The choice of the gas influences the energy deposition along the ionisation track and how charged particles behave in the gas volume. In the amplification stage many electronic avalanches are produced with the generation of electron/ion pairs. From the recombination of the gas atoms UV photons can be emitted and hence induce new ionisations and consequent cascades. The quencher gas is added because of its higher cross section to absorb the emitted electromagnetic radiation in comparison to the noble gas. The quencher gas allows to avoid discharges in the active volume which would possibly damage the detector. Thanks to the quencher gas it is then possible to apply higher voltages to the electrodes and to reach higher drift velocities and gains.

The SpecMAT active target has been characterised with a triple α-source. The performance has been evaluated by the capability of the detector to distinguish the three alphas emitted from the different isotopes contained in the alpha source, ^{239}Pu, ^{241}Am and ^{244}Cm. A second aspect that has been evaluated is the possibility to correlate the charge particles tracked by the TPC and the gamma rays detected in the scintillation array emitted during the nuclear reactions inside the active volume. For this purpose, attention was paid to the alpha decay of ^{241}Am into ^{237}Np and to the correlation between the 5485.6 keV α-particle and the 59.5 keV γ-ray emitted in the de-excitation of the daughter nucleus, ^{237}Np [19]. The triple-α source was placed behind the central hole of the Micromegas detector that will be used for the passage of the beam, at a distance of 8 mm from the mesh. The active area of the source was a disk with a diameter of 7 mm.

These measurements were performed in the laboratory at KU Leuven without a magnetic field. The trajectories of charged particles inside the TPC were therefore linear.

2.3.1 Calibration of the scintillation array

Three calibration sources, one composed of ^{60}Co atoms, one of ^{137}Cs isotopes and the other composed of ^{152}Eu, were used for the calibration of the $CeBr_3$ scintillators. The sources were placed outside and around the array. The detectors were calibrated by using the known energy values of the γ-rays emitted from the decay of the sources. In the tables the energy values of the γ-rays, reported in literature [19] and used for the calibration, are reported. In the tables are indicated also the calibration source and the daughter nucleus which decays to its ground state by emission of gamma-rays. Cobalt-60 has an half life of ~ 5 years and decays in Nichel-60 by β^- decay. Cesium-137 has an half life of ~ 30 years and decays by β^- emission to Barium-137 . Europium-152 has an an half life of ~ 13.5 years and can decay into Gadolinium-152 by β^- emission (~ 28 %) or into Samarium-152 by β^+ emission (~ 72 %).

Source	**Daughter**	**γ-ray energy (keV)**
$^{60}_{27}$Co	$^{60}_{28}$Ni	1173.228 ± 0.003
$^{60}_{27}$Co	$^{60}_{28}$Ni	1332.492 ± 0.004
$^{137}_{55}$Cs	$^{137}_{56}$Ba	661.657 ± 0.003

Source	**Daughter**	**γ-ray energy (keV)**
$^{152}_{63}$Eu	$^{152}_{62}$Sm	40.118 ± 0.001
$^{152}_{63}$Eu	$^{152}_{62}$Sm	121.7817 ± 0.0003
$^{152}_{63}$Eu	$^{152}_{62}$Sm	244.6974 ± 0.0008
$^{152}_{63}$Eu	$^{152}_{64}$Gd	344.279 ± 0.001
$^{152}_{63}$Eu	$^{152}_{64}$Gd	778.905 ± 0.002
$^{152}_{63}$Eu	$^{152}_{62}$Sm	964.057 ± 0.005
$^{152}_{63}$Eu	$^{152}_{62}$Sm	1408.013 ± 0.003

With this choice of the γ-rays sources, a good estimation of the calibration parameters for the scintil-

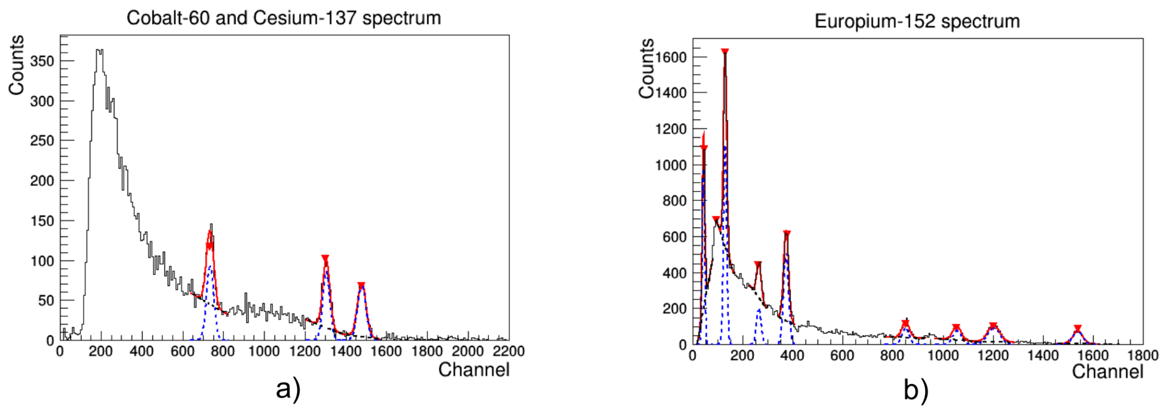

Figure 2.7: Calibration spectra. Fig. a) represents the spectrum obtained from the detection of the γ-rays emitted from the $^{60}_{27}$Co and the $^{137}_{55}$Cs sources by a single scintillation crystal. Fig. b) is the gamma spectrum obtained with the ^{152}Eu source. The peaks have been fitted by the convolution of a Gaussian (represented with the blue dashed line) and a first-order polynomial function (in the black dashed line) to remove the background from the photo-peak. The red lines represent the fits from which the centroids of the Gaussian have been obtained.

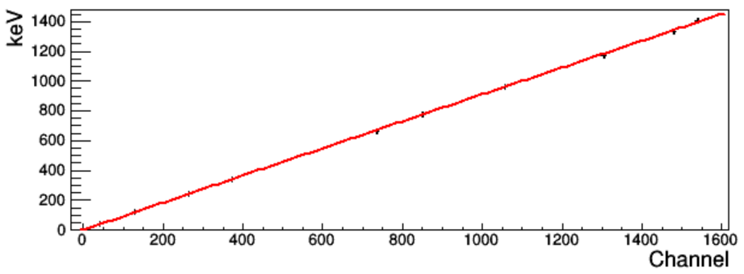

Figure 2.8: Calibration plot for one CeBr$_3$ scintillator. On the x-axis the γ-rays energy registered in channel units by the crystal is reported. The y-axis reports the corresponding energy values in literature in keV. From the interpolation of the points (the red curve), a second-order polynomial function, it was possible to obtain the calibration parameters for the crystal.

lators can be obtained in the energy range $\sim$ 40 keV - $\sim$ 1408 keV. Because of the low energy gamma rays present in the decay of ^{152}Eu, this calibration is also reliable for the identification of the 59.5 keV γ rays emitted from the ^{241}Am source, which is used for the characterisation of SpecMAT.

The array of CeBr$_3$ detectors, placed around the TPC, was equipped with 39 crystals. The data were acquired with a sampling frequency of 50 Ms/s, the same used for the first characterisation measurements in argon gas mixture.

For each crystal the gamma spectrum and the calibration curve were obtained. As an example, in Fig. 2.7-2.8 the graphs for one single CeBr$_3$ scintillator are shown. The photo-peaks in the gamma spectra recorded by each crystal of the array were fitted by the convolution of a Gaussian and a first-order polynomial function (respectively the blue and the black dashed lines in figure 2.7) in order to obtain the centroids of the peaks. These values corresponds to the γ-ray energies in channel units registered by the detectors. A plot with the centroids obtained experimentally and the corresponding values in literature of the γ-rays energy (in keV) was produced. The interpolation of the points was done with a second-order polynomial function: E[keV] = a*Channel^2 + b*Channel + c. The calibration parameters a,b and c have been obtained for each crystal of the array. Once the scintillators were calibrated, the characterisation measurement was performed.

In the future experiments in which SpecMAT will be used, the CeBr$_3$ crystals will detect the γ-rays emitted during the nuclear reactions inside the active volume. Because of this the the array was also

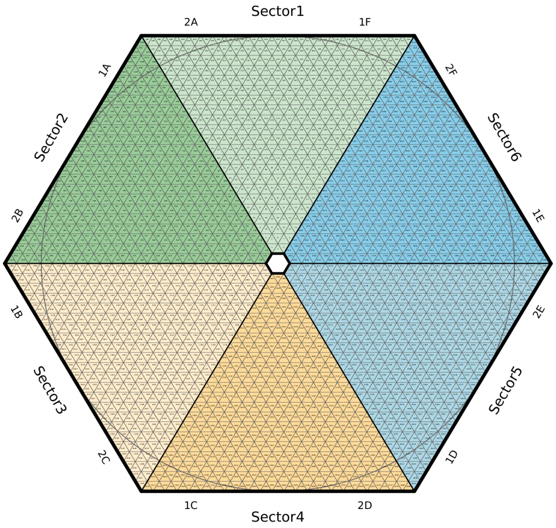

Figure 2.9: Micromegas Pad Plane. The hexagonal shape was considered in the algorithm to assign the IDs to the pads. The circle black line inscribed delimits the physical detector. The two green sectors (Sector 1 and Sector 2) are the ones that were connected for the characterisation measurements of SpecMAT. The figure is taken from Fig. C.2 of [52].

calibrated with a linear Europium-152 source placed inside the TPC volume, along the TPC axis. The γ-rays have to pass through the chamber walls and their intensity is thus reduced. In the measurement with the Europium-152 source placed inside the chamber, the low energy peaks (visible in Fig. 2.7 b)) are no longer visible. The calibration of the array is still possible although at low energy it results less accurate with respect to the calibration conducted with data acquired when the source is placed outside the chamber. The array was therefore calibrated with the sources placed outside the chamber and around the array, with the sampling frequency of 12.5 MS/s that was used for the characterisation of SpecMAT in helium gas mixture. The graphs for a single crystal for the two cases mentioned above are reported in Appendix A.

2.3.2 Characterisation with an argon gas mixture

For the first characterisation measurement the SpecMAT TPC was filled with the argon gas mixture Ar(95%)CF_4(5%) at 400 mbar. This pressure was selected in order to have a long trajectory ($\sim$ 10 cm) inside the active volume and a low probability that the charged particles reach the TPC walls. The long track allows for a good distribution of the electronic charge over the activated pads.

For the characterisation of SpecMAT, only two of the six sectors composing the complete configuration of the Micromegas detector were connected. They corresponds to the green sectors (Sector 1 and Sector 2) of Fig. 2.9.

As each sector is connected to two AsAd boards, a total of four AsAd were connected for the readout of the Micromegas sectors. Moreover, one AsAd card was used for the readout of the scintillation array. In this characterisation measurement, the trigger for the GET electronics was set by the internal multiplicity trigger. The bunch of data inside the acquisition time window was considered an event when the signals of at least five pads within the central seven rows of the Micromegas Pad Plane were recorded.

The setting applied to the electronics is the same as the setting used in the previous measurement, reported in [53]. The voltages applied to the TPC electrodes are: cathode -5 kV, last inner electrode of the field cage -250 V, mesh of Micromegas -240 V. The last external electrode of the field cage and the gas chamber were grounded. By applying these voltages to the TPC, which is 323.5 mm long, the electric field was set to $\sim$ 147 V/cm. The measurement was done at a sampling frequency of 50 MS/s,

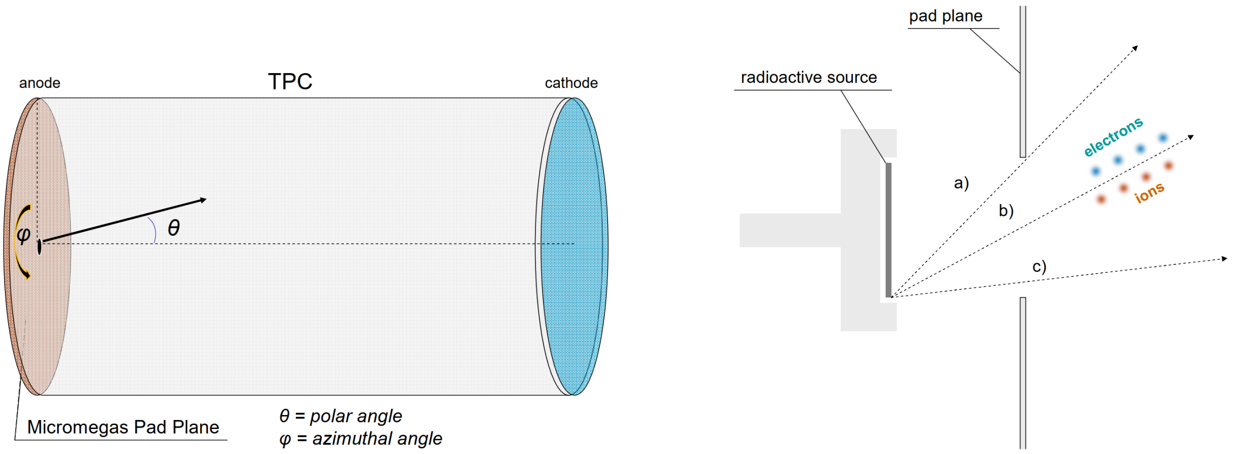

Figure 2.10: The figure on the left is a schematic view of the TPC with the Micromegas detector. The polar and the azimuthal angles of the particles emission are reported. On the right is shown the radioactive source placed before the entrance of the TPC and three possible cases of radiation emission are presented. The starting position in which the particle is emitted is considered at the limit of the radioactive source, but the following discussion is valid for each position. a) corresponds to the limit-case in which the radiation can be recorded by the detector. Beyond this angle limit, the radiation hits the Pad Plane before reaching the TPC active volume. b) represents all the events that can be recorded by the activated pads which collect the electronic charge. The ionisation tracks visualised in c) are also events lost by the detector because the ionisation electrons drift toward the hole in the center of the Micromegas and they never reach the Pad Plane.

which corresponds to one sample every 20 ns.

When the alpha particles pass through the active volume they ionise the atoms of the gas and produce an ionisation track. From the 3D reconstruction of the tracks it is then possible to obtain the angle of emission, the distance travelled inside the active volume and the kinetic energy lost by the particle traversing the gas. The energy information is provided by the charge signal generated by the pads which record the electrons during the event. In order to extract the track length information the 2D projection of the tracks in the Pad Plane and the distance travelled from the particle along the beam direction have to be obtained. The 2D projection is obtained from the activated pads of the Micromegas detector during an event. The third dimension, along the TPC axis, can be calculated from the timing information of the activated detector pads and from the drift velocity of electrons. The electron drift velocity in the TPC under the applied voltages in the Ar(95%)CF$_4$(5%) mixture at 400 mbar is $\sim$ 0.1 mm/ns. A graph with the drift velocity of electrons in the argon gas mixture in function of the electric field applied (in V/cm) is reported in section 2.3.4.

From these two parameters (energy and length) it is possible to reconstruct the energy spectrum of the charged particles emitted from the triple alpha source as a function of the emission angles. The emission angles are the polar angle θ, defined with respect to the beam line and perpendicular to the Micromegas detector and the azimuthal angle ψ, referred with respect to the plane of the Micromegas. A schematic view of the emission angles in the TPC is shown in Fig. 2.10.

The limits on the azimuthal angle are due to the Pad Plane sectors connected during the measurements ($0° < \psi < 30°$ and $270° < \psi < 360°$). The polar angle is limited from the walls of the Micromegas detector because of the recessed position of the source, placed behind the hole center of the Pad Plane. The lower limit is reached when the trajectory of the alpha particle is entirely (or almost) contained inside the cylinder with base the disk of the source. For these events either the electrons are not collected on the Micromegas or the number or activated pads is lower than the trigger threshold. Because of this fact the electronic system does not record them as an event.

The number of recorded events as function of the track length and the angle of particles emission and as function of the deposited charge in the Pad Plane and the angle is shown in Fig. 2.11. The

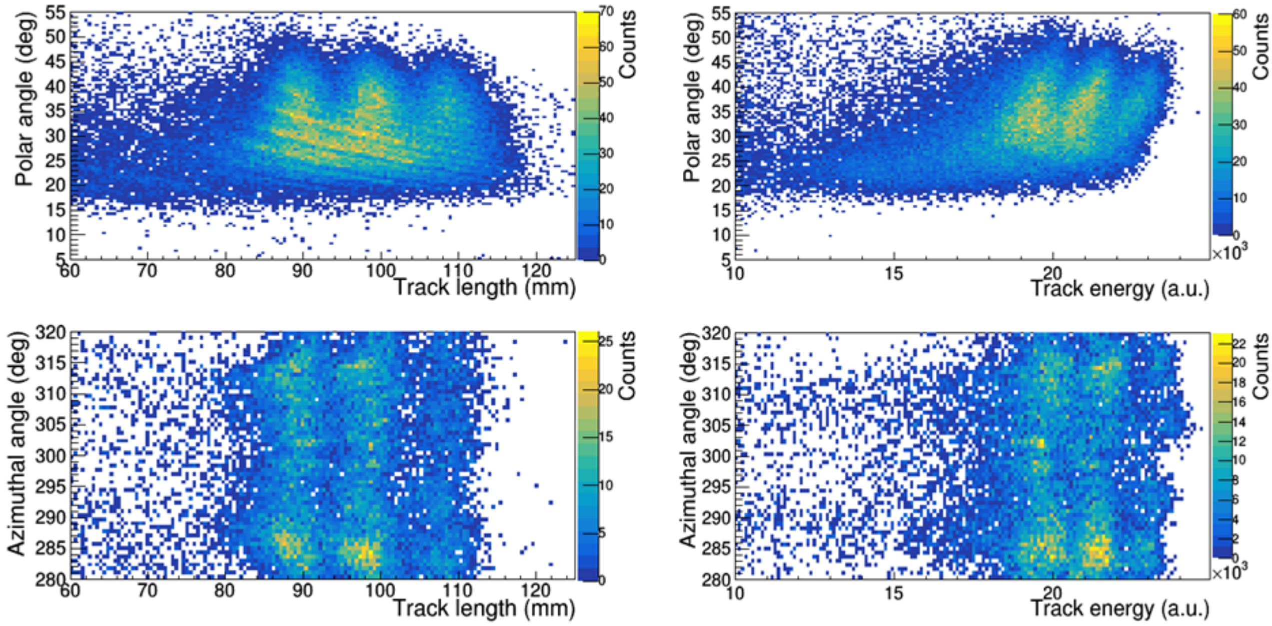

Figure 2.11: Number of recorded events as function of the track length and the angle of the particles emission (or as function of the deposited energy and the angle) inside the active volume of the TPC in argon gas mixture. The two plots on the left are based on the ionisation tracks length of the particles produced inside the TPC. The graphs on the right are based on the collected charge produced by the particles crossing the TPC volume. In each graph it is possible to distinguish the three region corresponding to the three different isotopes contained in the alpha source (^{239}Pu, ^{241}Am and ^{244}Cm). The zoom on the azimuthal angle was applied for a better visualisation of the data.

distortion of the energy spectrum as a function of the charge collected (the top right figure in 2.11) happens when the α-particles emitted within small polar angles. These alphas produce ionisation tracks in which charge is distributed above only few pads. The charge is not precisely estimated if the signals from the pads are saturated. Moreover, the charge corresponding to electrons that drift trough the hole in the center of the Micromegas is not recorded and this causes a loss of charge collected on the pad plane. For small polar angles the energy loss due to not collected electrons is a larger fraction of the total energy released in the gas by the particle during the ionisation. As a consequence, for tracks with a small polar angle, the total energy is not accurately reconstructed and the spectrum is shifted towards lower energies, producing a worsening on the energy resolution. In the graphs, based on the length of the tracks and on the energy of the particles, it is possible to distinguish the three different isotopes contained in the alpha source, both in the polar and in the azimuthal angles.

In order to have a better separation of the three isotopes it is possible to correlate the two analysed parameters, particles energy and tracks length, as shown in the correlation plot reported at the top in Fig. 2.12. A gate on the polar angle ($38° < \theta < 50°$) was applied to avoid the events for which the energy was not correctly estimated. The three coloured lines in figure 2.12 a) indicate the gates chosen to select events which belong to a specific alpha decay. The green line delimits the events of Plutonium-239 (the 5.17 MeV alphas), the red line the Americium-241 events (the 5.49 MeV alphas) and the blue line the events of Curium-244 (the 5.80 MeV alphas).

From the projection of the correlation plot on the track length, the length-based energy spectrum was obtained. It is reported in the middle of figure 2.12 as the histogram in black of figure b). The y-axis is in logarithmic scale. By gating on the α-particle clusters of top figure a) it is possible to obtain the separation of the three isotopes, as shown in figure b) by the coloured-line peaks. The coloured-filled peaks in figure show events corresponding to particles recorded in coincidence with γ-rays, for which a gate on the energy range 30 keV - 110 keV was applied.

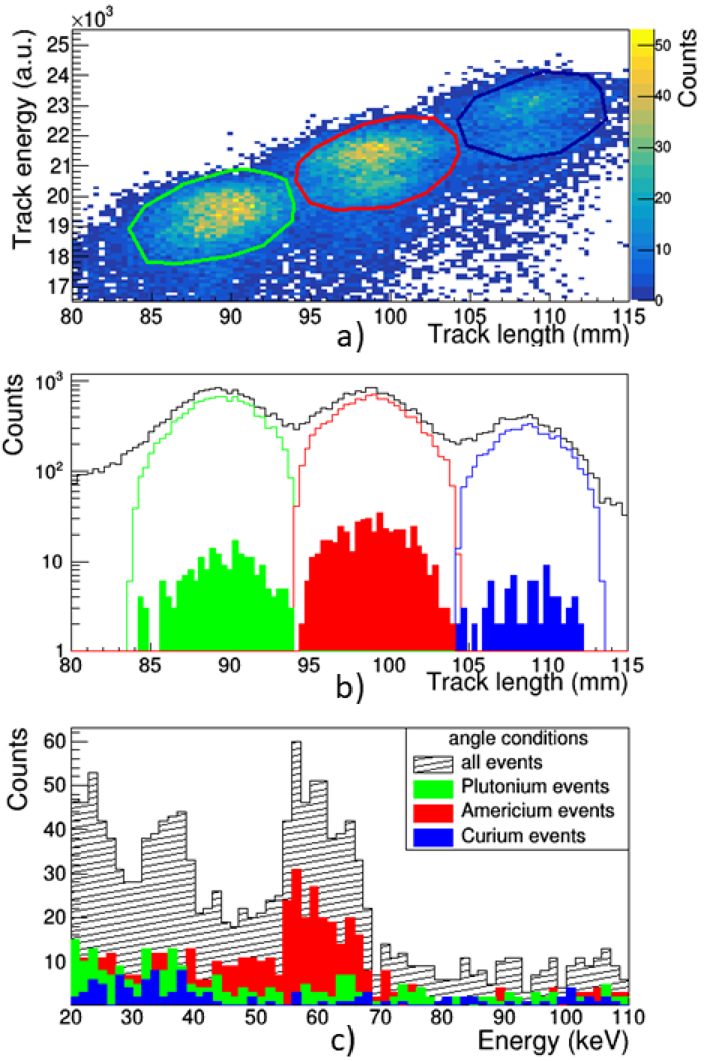

Figure 2.12: Correlation plots in argon gas mixture. A gate on the polar angle (38° $< \theta <$ 50°) was applied. Fig. a) correlates the energy of the charged particles (measured as collected charge) and the tracks length. The three clusters highlighted enclose the events which correspond to the alpha decay of ^{239}Pu, ^{241}Am and ^{244}Cm. Respectively indicated in green, red and blue. The black histogram of Fig. b) was obtained by the projection of the top figure on the track length. The coloured-line peaks in the figure represent the events contained in each singular alpha cluster. The coloured-filled peaks in figure are constituted by particle events recorded in coincidence with γ-rays with an energy range 30 keV - 110 keV. Figure c) reports the total γ-rays spectrum in gray and the spectra with events containing a γ ray in coincidence with an alpha particle in one of the clusters. The red peak at $\sim$ 60 keV contains the gammas emitted from the ^{237}Np decay (daughter nucleus of ^{241}Am).

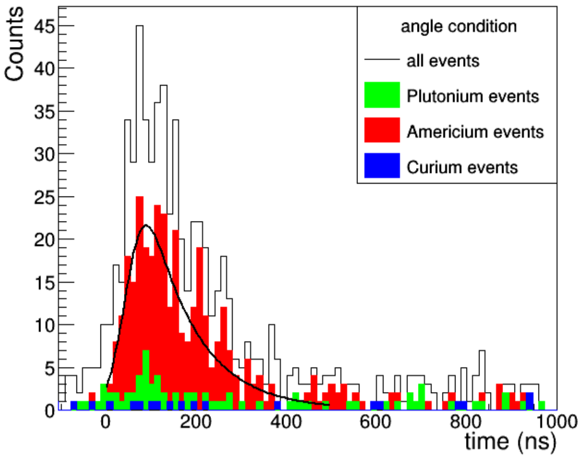

Figure 2.13: Spectrum of time coincidences between the particle events recorded in the Micromegas and the γ-rays detected by the scintillation array. To obtain the total spectrum, in white, only the gate on the polar angle was applied. For the data shown as coloured histograms a further gate on the alpha particle clusters of Fig. 2.12 a) was applied. The exponential trends of the red histogram is due to the alpha decay of ^{241}Am and the subsequent gamma decay of ^{237}Np. In black, the fit used for the measurement of the half-life of ^{237}Np is shown.

When a trigger is generated in correspondence of an event after the activation of pads due to the collection of electronic charge in the Pad Plane, signals are acquired by the scintillation array. The time window of GET electronics is 10.24 μs, which corresponds to the 512 memory cells of GET times 20 ns, derived from the sampling frequency applied to the acquisition system (50 MS/s). Within this period of time the array of CeBr$_3$ crystals records γ-rays which are related to that particular event. During the data acquisition was therefore possible to correlate the gammas and the alpha particles. The γ-ray spectrum recorded during the characterisation measurement is shown in grey in the Fig. 2.12 c). As for the plots before mentioned, a cut was applied based on the events with an emission polar angle between 38° and 50°.

The three coloured histograms superimposed on the γ-ray spectrum are obtained by gating on the α-particle clusters of the top figure. The correlation between the signal of α-particles emitted from the decay of ^{241}Am and the 59.5 keV γ-ray due to the gamma decay of the daughter nucleus (^{237}Np) is observed as the peak in the red histogram in the gamma spectrum figure.

In Fig. 2.13, the time coincidence spectra between the α-particles detected as charge deposited in the Micromegas and the γ-rays detected by the scintillation array is shown. The histogram delimited by the black line was obtained by gating only on the polar angle. The red histogram represents the gamma events in correlation with the alphas emitted from the Americium-241 decay. They corresponds to the 59.5 keV γ-rays of the ^{237}Np decay.

In the figure the typical exponential trend of radioactive decay appears. The law that governs decays is an exponential function: $\mathrm{N(t)} = \mathrm{N_0 e}^{-\frac{ln2}{t_{1/2}}t}$ where N(t) is the number of radioactive atoms at the time t, $\mathrm{N_0}$ the initial number of radioactive atoms at time $\mathrm{t_0}$ and $\mathrm{t_{1/2}}$ is the half life. For the fit of the red spectrum in figure an exponential convoluted with a Gaussian function was used. The Gaussian function takes into account the uncertainty on the determination of the starting time of the emission of the alpha particles from the radioactive source. Indeed, the time of the charge collection depends on the trajectory and emission angle of the alpha particle. The fitted curve is shown as a black line. The measured half-life is $\mathrm{t_{1/2}} = 73(8)$ ns. This value is in good agreement with the 67.2(7) ns value in literature [19].

If the goal of the data analysis is not to correlate the alphas with the γ-rays but to measure the energy

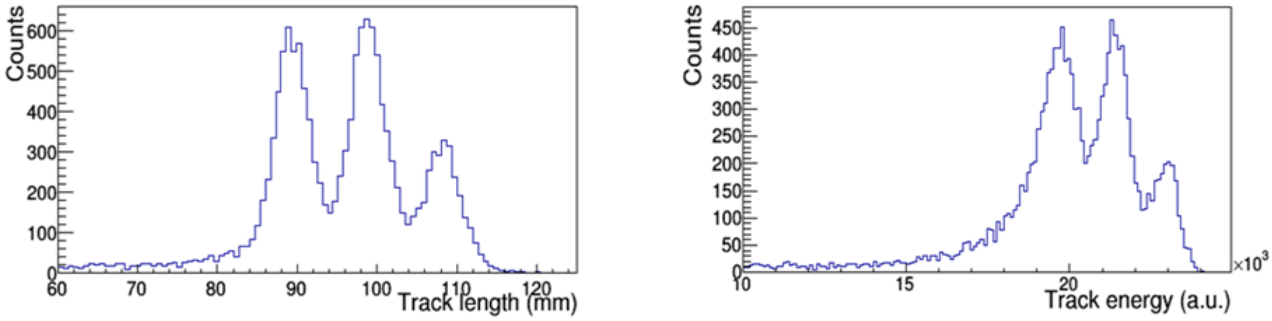

Figure 2.14: Energy spectra of the alpha tracks inside the TPC with respect to the reconstructed length and the collected charge. In order to measure the better value of energy resolution achievable by the SpecMAT detector for the particular setting applied and argon gas mixture used, a smaller gate on the emission angles were applied (see text for details).

resolution of the TPC, high statistics is not needed. It is possible to filter the total amount of events acquired on a smaller range of the emission angles of the particles, in order to disentangle the three alpha distributions (^{239}Pu, ^{241}Am, ^{244}Cm). By observing the projection of the angular distribution based on the track length in Fig. 2.11 on the x-axis, the gate for the polar angle was chosen $38° < \theta < 50°$ and the gates on the azimuthal angle were chosen $270° < \theta < 285°$ and $315° < \theta < 340°$. By observing the projection of spectrum based on the track energy, the cuts chosen were $38° < \theta < 50°$for the polar angle and $0° < \theta < 20°$ and $280° < \theta < 300°$ for the azimuthal angle.

The projections of the spectra based on the track length and the track energy, obtained after the angle cuts, are reported in Fig. 2.14. The energy resolution of the TPC can be expressed as the FWHM (Full Width Half Maximum) of the peaks in figure, measured by fitting the histograms in the region of the peaks with three Gaussians and a linear background. The resolution achieved with these specific gates on the angles is $\sim$ 5.4 mm for the ^{241}Am peak, which is equivalent to $\sim$ 185 keV at $\sim$ 5.5 MeV α-particles. The energy spectrum based on the particles energy (as charge collected) has a lower resolution of $\sim$ 195 keV at $\sim$5.5 MeV. The resolution values are affected by the finite dimensions of the triple alpha source. The exact emission point of the particles can not be reconstructed and this affects the time measurement, which depends on the time of charge collection.

2.3.3 Characterisation with an helium gas mixture

All the energy spectra obtained from the alpha tracks inside the TPC and the γ-rays detected in the scintillation array together with the correlation plots have been reproduced for the SpecMAT characterisation in a mixture of He(98%)CF$_4$(2%).

As for argon, the total target thickness and the energy range of the particles have to be taken into account for the choice of the gas pressure. The pressure inside the gas chamber of SpecMAT was stabilized at 1000 mbar. The internal multiplicity trigger and a sampling frequency of 12.5 MS/s, which corresponds to a sample every 80 ns, were set in GET electronics. The voltages applied to the TPC electrodes are: cathode -5.74 kV, last inner electrode -250 V, mesh of Micromegas -240 V. The last external electrodes and the gas chamber were grounded. By applying these voltages to the TPC, which is 323.5 mm long, the electric field was set to $\sim$ 170 V/cm. The electron drift velocity in the TPC under the applied voltages in the He(98%)CF$_4$(2%) mixture at 1000 mbar is $\sim$ 0.01 mm/ns. In section 2.3.4 a graph of the electron drift velocity in function of the electric field in the helium gas mixture is reported in Fig. 2.18 and discussed.

The number of recorded events as function of the distance traveled in the active volume and the angle of emission is shown in Fig. 2.15. The three regions representing the different isotopes contained in the calibration source are well separated. The apparent line at high polar angles is due to the alpha

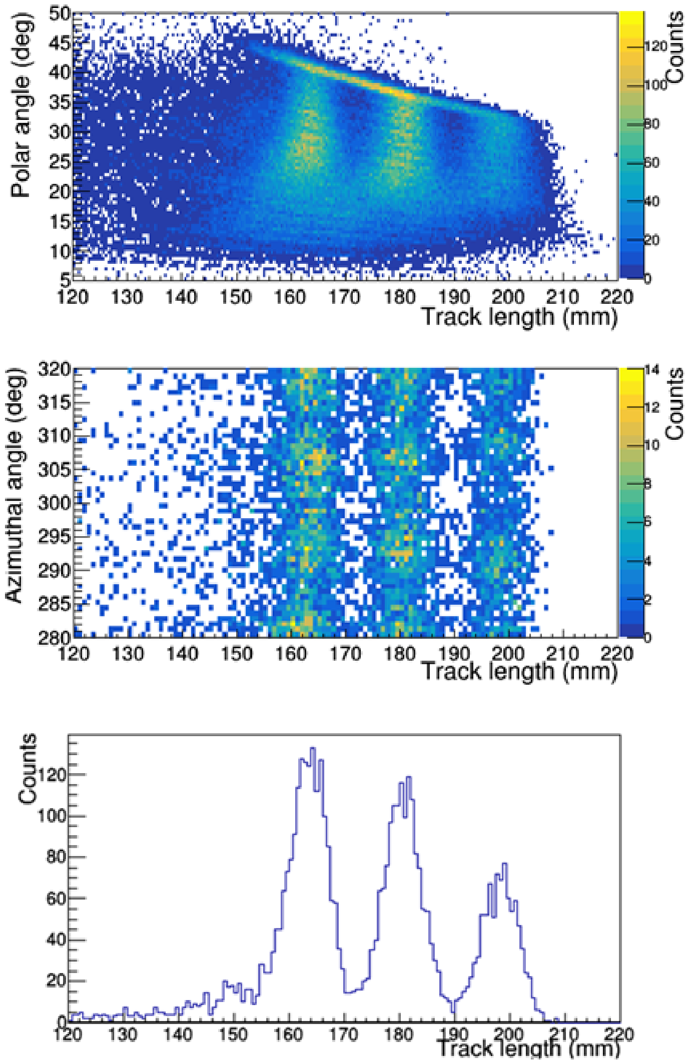

Figure 2.15: The top and the middle figure are the number of recorded events as a function of the distance traveled inside the active volume of SpecMAT in helium gas mixture and the angle of emission of the α-particles. In each graph it is possible to distinguish the three regions corresponding to the three different isotopes contained in the alpha source (^{239}Pu, ^{241}Am and ^{244}Cm). The zoom on the azimuthal angle was applied for a better visualisation of the data. The bottom figure represents the spectrum of the alpha particles based on the tracks length used for the measurement of energy resolution.

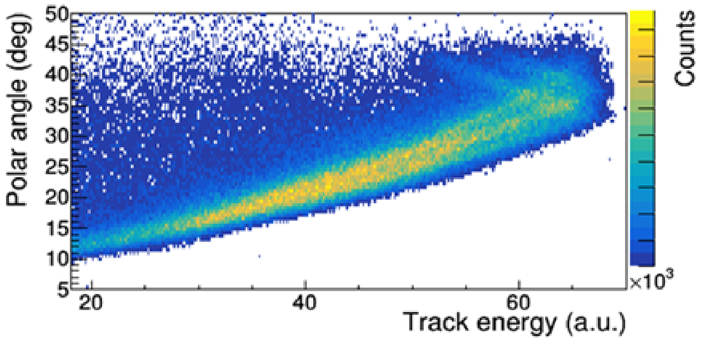

Figure 2.16: Number of recorded events relative to the polar angle of emission of the alpha particles as a function of the collected charge by the Pad Plane of SpecMAT. The separation of the three regions corresponding to the three isotopes in the alpha source is not possible. This phenomenon was investigated and it is discussed in section 2.3.4.

particles which reach the TPC walls and for which, as a consequence, the total track length can not be completely reconstructed. Small ranges on emission angles were considered to obtain the optimal energy resolution that the detector can achieve with these settings and in helium gas mixture. The gates selected were $28° < \theta < 31°$ for the polar angle and $290° < \theta < 310°$ for the azimuthal angle. The length-based spectrum obtained is reported at the bottom of figure 2.15. From the fit of the peaks in the histogram an energy resolution of $\sim$ 146 keV FWHM at $\sim$ 5.5 MeV α-particles was obtained.

From the number of recorded events as a function of the charge collected in the Micromegas Pad Plane it was not possible to distinguish the three separate isotopes of the alpha source. In Fig. 2.16 it can be noticed how the distribution of events does not allow to obtain the energy spectrum based on the charge collected with the well separated regions for ^{239}Pu, ^{241}Am and ^{244}Cm.

It was however still possible to properly separate the three clusters of isotopes by using the correlation between the length of the tracks and the energy deposited, because of the good separation based on the track length. A cut on the events with a polar angle $22° < \theta < 31°$ was applied. As shown in the plot at the top of Fig. 2.17, it is still possible to distinguish the three cluster regions corresponding to the three isotopes contained in the alpha source. The clusters in figure are highlighted with three different colours, green for Plutonium-239 events, red for Americium-241 events and blue for Curium-244 events. The correlation plots between the alpha particles and the gammas are shown in the middle and bottom figures. The γ-rays emitted in the decay of ^{241}Am appear as the red peak in the bottom figure. With the helium gas mixture He(98%)CF$_4$(2%) the SpecMAT active target is capable to correlate charged particles recorded from the TPC and the γ-rays detected from the scintillation array.

From the time coincidence spectrum it was not possible to obtain the half-life of ^{237}Np. Indeed the uncertainly on the starting time of emission of the alpha particles made impossible to analyse the data information recorded by the detector. This is due to a bad timing resolution of the SpecMAT TPC when performing in the helium gas mixture He(98%)CF$_4$(2%). The timing properties were investigated and the discussion is presented in the following section.

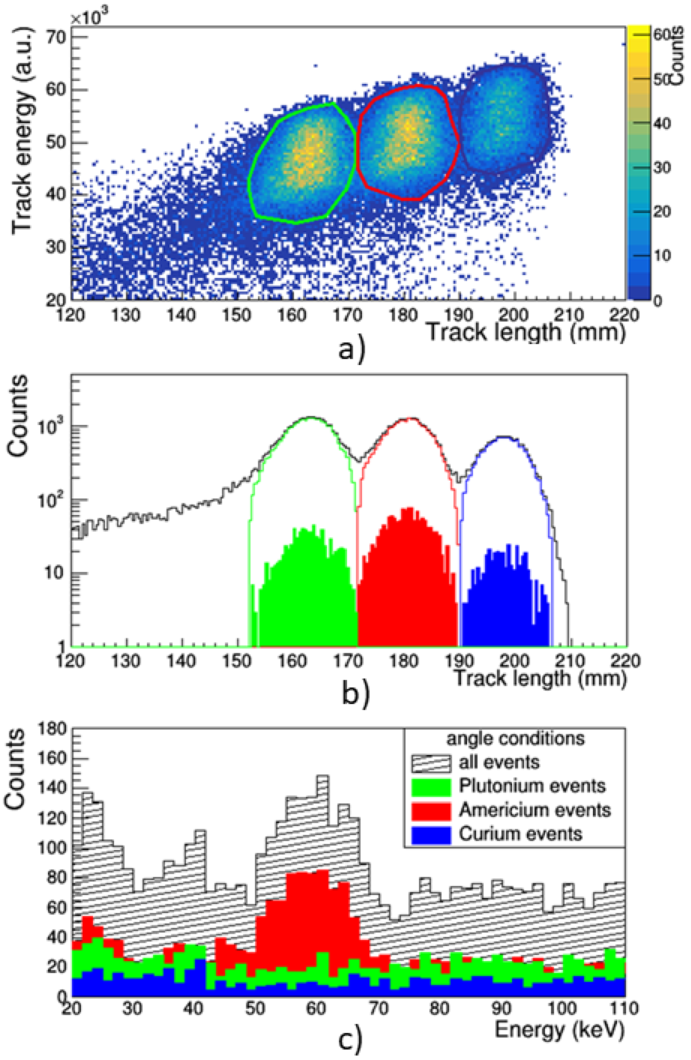

Figure 2.17: Correlation plots in helium gas mixture. A gate on the polar angle ($22° < \theta < 31°$) was applied. Fig. a) correlates the energy of the charged particles (measured as collected charge) and the tracks length. The three clusters highlighted enclose the events which correspond to the alpha decay of ^{239}Pu, ^{241}Am and ^{244}Cm, respectively indicated in green, red and blue. The black histogram of Fig. b) was obtained by the projection of the top figure on the track length. The coloured-line peaks in the figure represent the events contained in each singular alpha cluster. The coloured-filled peaks in figure are constituted by particle events recorded in coincidence with γ-rays with an energy range 30 keV - 90 keV. Figure c) reports the total γ-rays spectrum in gray and the spectra with events relative to the γ-rays correlated to the alpha particles inside the clusters with fill-coloured histograms. The red peak at $\sim$ 60 keV contains the gammas emitted from the ^{237}Np decay (daughter nucleus of ^{241}Am).

2.3.4 Performance comparison with different settings

This section is dedicated to the investigation of the causes that can lead to a worsening of the energy resolution observed with the SpecMAT detector in presence of the He(98%)CF_4(2%) gas mixture and inferior timing properties with respect to the performance in Ar(95%)CF_4(5%) gas mixture.

The working condition of GET electronics was the first item studied. Particularly the electronics acquisition and processing of data were analysed by changing different aspects of the settings (voltages applied and sampling rate), that were applied for the characterisation measurement in helium.

Attention was focused on the electronic avalanches produced in the amplification region between the mesh and the Pad Plane of the Micromegas detector. Different values of the voltage (which are reported in the following tables) applied to the mesh electrode were tested, in order to collect more charges relative to the same incoming electron and to achieve a higher signal on the pads. The graphs obtained from the measurements are shown in Appendix B in Fig. B.10- B.13. They do not show a better energy resolution and timing property of the detector with respect to the previous measurements with helium gas.

Then, to make a proper comparison with the performance in argon gas, the characterisation was conducted again in presence of the argon mixture but with a sampling frequency set to 12.5MS/s, as was the case for the measurements with the helium mixture. This value corresponds to one sample every 80 ns and it was chosen for the helium measurement in order to cover all the signal acquired in a time window. For the characterisation in argon gas mixture, a sampling frequency of 50 MS/s (which corresponds to a sample every 20 ns) is sufficient to cover all the signal, but can be changed to lower values.

Using the drift velocities obtained from the Garfield simulation, the electron drift velocity in the gas mixtures ($\sim$ 0.1 mm/ns in Ar(95%)CF_4(5%) and $\sim$ 0.01 mm/ns in He(98%)CF_4(2%) at the pressure and electric field applied during the measurements) it is possible to evaluate the maximum time window needed to collect the electronic charge, produced by the ionisation of the gas atoms by the incoming charged particles. The maximum time is the time that an electron generated in the active volume of the TPC just before the cathode needs to reach the Pad Plane. The TPC being 323.5 mm long, the time window needed in argon gas is $\sim 3\ \mu$s while in helium gas $\sim 32\ \mu$s. The maximum memory space allowed from GET electronics is limited by the SCA (Switch Capacitor Array), which contains 512-cells. Selecting a sampling frequency of 50 MS/s results in a total time interval of 20 ns x 512 = 10 μs, while for 12.5 MS/s this increases to 80 ns x 512 = 40 μs. Because of this a sampling frequency of 50 MS/s and 12.5 MS/s are the optimised values to be set in the electronics during measurements in argon and helium respectively, in order to sample all the signal.

The results obtained with 12.5 MS/s (Fig. B.1- B.3 in Appendix B) in presence of the argon gas mixture show a better performance of SpecMAT with respect to the measurements in helium gas mixture. Therefore it was concluded that the sampling frequency setting in GET electronics is not responsible for the bad timing properties of the active target observed in helium.

Another aspect that was evaluated, for the bad energy resolution, was the time of collecting the charge and the distribution of the charge collected along the Pad plane. A characterisation in argon was done at 50MS/s and by applying a pressure of 250 mbar to produce longer tracks in the gas, with a similar length with respect to the ones in helium at 1000 mbar. For the 5.5 MeV alpha particles the length is $\sim$ 16cm in argon gas mixture at 250 mbar and $\sim$ 18cm for helium gas mixture at 1000 mbar. Fig. B.4- B.6 of Appendix B show the graphs obtained for these characterisation measurements and do not explain the first results obtained in helium mixture.

To complete the investigation a new characterisation measurement in argon gas was made at 250 mbar of pressure with a sampling frequency of 12.5 MS/s. The results, even if worse than the others, still allows to evaluate the energy resolution via the charge collected and to measure the half-life of the

Argon run	**Pressure (mbar)**	**S. rate (MS/s)**	**Cathode (kV)**	**Last el. (V)**	**Mesh (V)**
1	400	50	-5	-250	-240
2	400	12.5	-5	-250	-240
3	250	50	-2.83	-250	-240
4	250	12.5	-2.83	-250	-240

Table 2.1: The pressure stabilized in the TPC, the sample rate of GET electronics and the voltages applied to the TPC electrodes for each characterisation measurement, using the argon gas mixture Ar(95%)CF_4(5%), are indicated in table. For all the measurements the triple alpha source ^{239}Pu/^{241}Am/^{244}Cm was used. The trigger was set to the internal multiplicity for all the measurements.

Helium run	**Pressure (mbar)**	**S. rate (MS/s)**	**Cathode (kV)**	**Last el. (V)**	**Mesh (V)**
1	1000	12.5	-5.74	-250	-240
2	1000	12.5	-5.75	-260	-250
3	1000	12.5	-5.82	-325	-315

Table 2.2: The pressure stabilized in the TPC, the sampling rate of GET electronics and the voltages applied to the TPC electrodes for each characterisation measurement, using the helium gas mixture He(98%)CF_4(2%), are indicated in table. For all the measurements the triple alpha source ^{239}Pu/^{241}Am/^{244}Cm was used. The trigger was set to the internal multiplicity for all the measurements.

daughter nucleus of the Americium-241 decay (Fig. B.7- B.9 of Appendix B).

In Tables 2.1, 2.2 all the information of the settings are reported for each run, for the argon and helium gas mixture respectively. During all the measurements, the pressure inside the gas chamber was stabilised with a maximum variation of 1 mbar. Refer to Tab. C.1 - C.4 of Appendix C for the FWHM energies resolution and the half-life (only for argon) that were obtained from the characterisation measurement.

As a conclusion, the working conditions of GET electronics have been discarded as possible factors causing the bad energy resolution (from charge collection) and the bad timing propriety observed in helium gas characterisation. It is possible that the SpecMAT performances in the He(98%)CF_4(2%) gas mixture are due to the different drift velocity of electrons in the helium mixture with respect to the behaviour inside the Ar(95%)CF_4(5%) gas mixture. Indeed, both the energy and the time resolution are related to the collection of electrons that drift towards the Micromegas Pad Plane. The electron drift velocity as a function of the electric field applied was analysed and it is reported in Fig. 2.18. On the left the velocity graph simulated in Ar(95%)CF_4(5%) gas mixture at 400 mbar, while on the right in He(98%)CF_4(2%) gas mixture, are shown. At the voltages applied to the TPC electrodes during the characterisation measurements, the electric field inside the active volume of SpecMAT was $\sim$ 146 V/cm at 400 mbar in argon and $\sim$ 170 V/cm in helium at 1000 mbar. At these E-field values the electrons drift velocity inside the active volume is estimated to be $\sim$ 0.1 mm/ns in argon gas and $\sim$ 0.01 mm/ns in helium mixture, an order of magnitude less.

It is hence possible that electrons in He(98%)CF_4(2%) recombine with the gas atoms and diffuse much more with respect electrons in argon gas, causing worse working performance in helium mixture. Further future analysis could be performed by adding a higher concentration of the CF_4 quencher gas to the helium gas mixture. This will allow higher voltages to be set at the TPC electrodes an therefore to apply a higher electric field within the active volume of SpecMAT. Indeed, in the measurements carried out during this thesis work, the maximum voltage limit was applied to avoid the production of sparks inside the detector, and thus avoid the possibility of damaging it. Consequently to the larger electric field applied, the electron drift velocity would increase and their diffusion would be lower. This phenomenon would then affect the measurement of charge collection.

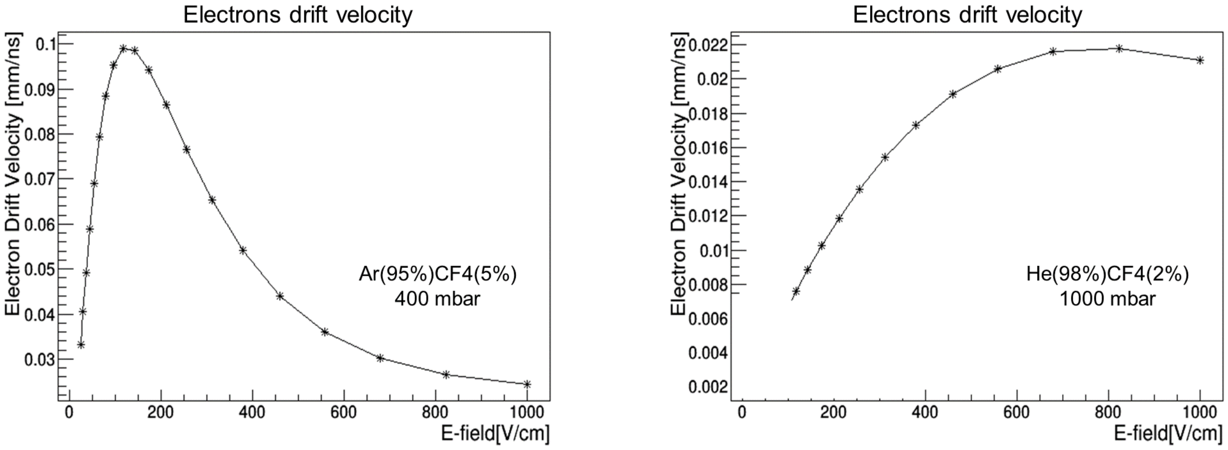

Figure 2.18: Velocity of electrons inside argon gas mixture (left) and helium gas mixture (right) mixtures when an electric field is applied. The images are provided by A. Ceulemans and were obtained by Garfield++ simulations.

Chapter 3

Simulation of the $\alpha(^{86}\text{Kr},^{3}\text{He})^{87}\text{Kr}$ transfer reaction

Transfer reactions are an important tool to investigate the structure of nuclei and hence to study the nuclear interaction. Particularly, one-nucleon transfer reactions are very useful for the study of low-lying single-particle states of the nuclei. The kinematics and cross sections of transfer reactions were discussed in Chapter 1 in section 1.3.

By using one-nucleon transfer reactions, it is possible to perform measurements of the purity of the single-particle configuration of nuclei. This allows to better investigate the role of nucleon interactions in the nuclear force.

An interesting aspect which can be investigated is the shell evolution. One of the techniques to study it is one-nucleon transfer reaction. By moving through a sequence of isotopes or isotones, within the vicinity of a closed shell, it is possible to measure with a transfer reaction the changing position of the orbitals.

The motivation to study the $\alpha(^{86}\text{Kr},^{3}\text{He})^{87}\text{Kr}$ transfer reaction in this thesis work was to extend the studies performed in [57] about the shell evolution in the structure of N = 51 nuclei (N is the number of neutrons), with one neutron outside the N=50 shell closure. By using the (d,p) and (α,^{3}He) neutron-adding reactions on N=50 isotones, they aimed to study the properties of ^{89}Sr, ^{91}Zr, and ^{93}Mo, ^{87}Kr nuclei. For ^{87}Kr, only (d,p) measurement was carried out, because no suitable targets were available to perform the (α,^{3}He) reaction in inverse kinematics. The analysis of the (α,^{3}He) reaction is important because it allows to transfer a higher momentum and reach energy states with higher angular momentum. Because of this, one of the goals of the thesis (and the focus of this chapter) was to evaluate of the feasibility to study the $\alpha(^{86}\text{Kr},^{3}\text{He})^{87}\text{Kr}$ transfer reaction with the active target SpecMAT. The detector could then be potentially used to perform the (α, ^{3}He) reaction on nuclides with different proton numbers, in order to study systematically the shell evolution along N=50.

In this chapter, a simulation of the $\alpha(^{86}\text{Kr},^{3}\text{He})^{87}\text{Kr}$ reaction with a population of the ground state and the first few low-lying states in ^{87}Kr is discussed.

3.1 Simulation of Helium-3 tracks in a magnetic field

From the characterisation measurements discussed in Chapter 2, it was possible to obtain the information about the feasibility to detect charged particles in the He(98%)CF$_4$(2%) gas mixture with the SpecMAT active target.

Once confirmed that SpecMAT can detect the charged particles and hence the reaction products in the helium gas mixture, the $\alpha(^{86}\text{Kr},^{3}\text{He})^{87}\text{Kr}$ transfer reaction was simulated with SPMTsim simulation

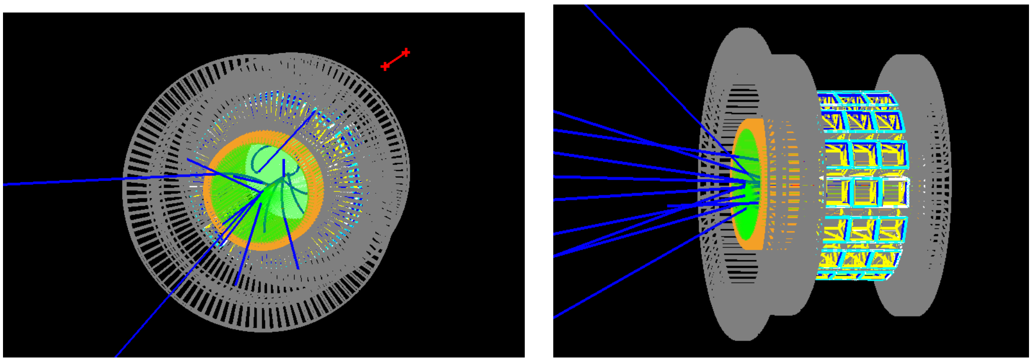

Figure 3.1: Visualisation of ^{3}He particles simulated inside SpecMAT, when a magnetic field of 2.5 T is applied.

by using Geant4 packages. In the simulation, a beam of ^{86}Kr isotopes was delivered to the TPC active volume of the SpecMAT detector, filled with the He(98%)CF$_4$(2%) gas mixture. Low-lying states of ^{87}Kr were populated in the reaction together with production of the ^{3}He ejectile. Three states of ^{87}Kr were populated in the reaction: the ground state and the two low-lying energy states at $\sim$ 1.476 MeV and the $\sim$ 1.420 MeV. With the simulation, an evaluation of the SpecMAT capability to separate in energy the two excited states was conducted. The levels differ in energy by only $\sim$ 60 keV, so high-energy resolution is required. The simulation was performed with a 2.5 T magnetic field applied with direction opposite to the beam direction. This corresponds to the condition of SpecMAT working inside the ISS magnet at ISOLDE/CERN. The ionisation tracks produced by ^{3}He ejectiles crossing the active volume will have therefore a curved shape. The ^{3}He particle tracks inside the active volume of SpecMAT were simulated. In Fig. 3.1 a representation of the alpha particles bending inside the SpecMAT detector, due to the magnetic field applied, is shown.

As an input of the simulation, the beam energy was set at 7 MeV/u, which is the value that will be delivered at ISOLDE/CERN for the future experiments. The total kinetic energy of the beam results E_{beam} = 602 MeV. When the beam crosses the active volume of SpecMAT, it will decrease in energy due to interaction with the gas atoms. The simulation of the beam energy loss inside the active target allows to estimate the beam energy at the reaction vertex, which is important for the reconstruction of the dynamic of the transfer reaction. In the simulation the beam energy loss was applied. A plot of the energy beam loss along the TPC volume is reported in Fig. D.1 of Appendix D. The pressure of the helium gas mixture was set at 250 mbar. The temperature in the simulation was set to 293.15 K. The transfer reactions were simulated along the beam path, in the whole length of the TPC, therefore the reaction vertices have a uniform distribution along the TPC central axis. In the analysis both the ^{3}He ejectile and the γ-rays produced from the de-excitation of ^{87}Kr were simulated and the energy loss of ^{3}He crossing the gas volume was considered. The same number of events was simulated for each state considered (the ground state and the two excited states at $\sim$ 1.420 MeV and the $\sim$ 1.476 MeV of ^{87}Kr).

From the activated pads in the simulation, it was possible to reconstruct the 2D track projected on the Pad Plane. In Fig. 3.2 two graphs are shown for the visualisation of a single event. The graph on the left is a schematic view of the Pad Plane (in blue) in which the points (in red) that indicate the activated pads within the time window of the event are superimposed. The X-Y projection of the 3D ionisation tracks generated in the TPC is thus represented in the graph. For each event a fit of the 2D track projection with a circular trajectory was computed. An example of a projected track and the circle reconstructed from the fit parameters is shown on the right of Fig. 3.2.

The XY-plane represents the plane of the Micromegas detector. The parametric equation which describes a circle on a X-Y plane is:

$$r^2 = (x - X_{center})^2 + (y - Y_{center})^2 \tag{3.1}$$

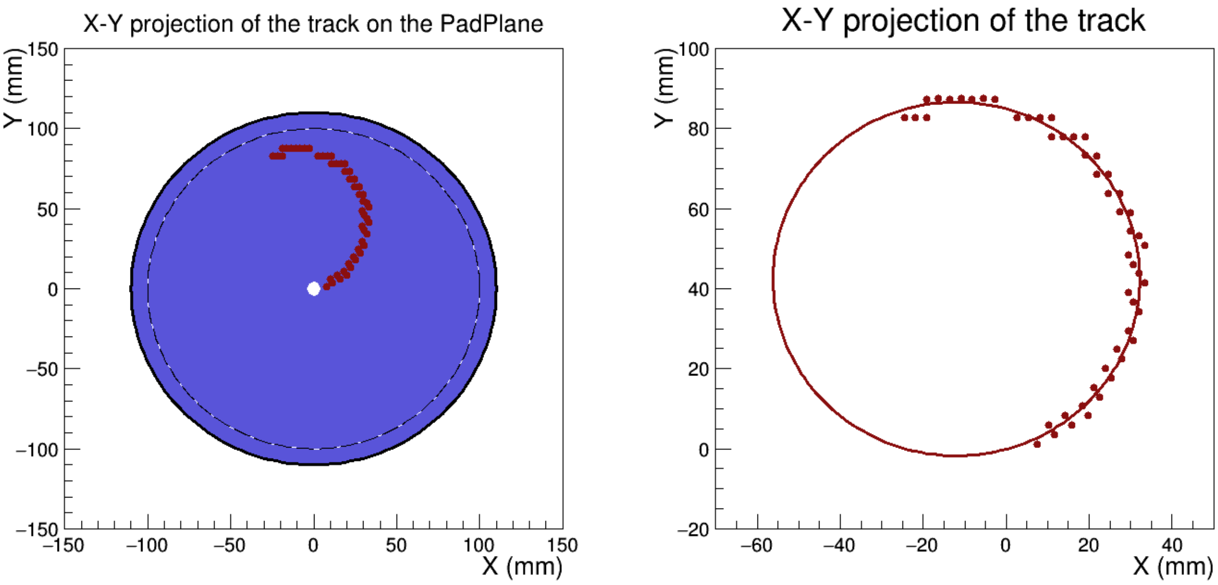

Figure 3.2: Graphs representing the data acquired for one ^{3}He particle event. Schematic view of the Pad Plane (left) with the activated pads in the event (in red), which give information about the 2D ionisation track projection on the Pad Plane. Zoom on the projected track with the circular fit applied (right).

where r is the radius of the circle, X_{center} and Y_{center} are the coordinates of the circle center, x and y are the coordinates of each point in the circumference. By fitting the points with this formula it was possible to obtain the radius of the total circumference reconstructed and the coordinates of the center of the circle (X_{center}, Y_{center}).

In order to reconstruct the 3D circular helix track, the fit parameters just obtained and the information along the Z axis were used. The z-axis is oriented along the TPC axis, hence along the beam direction.

The information about the third dimension of the track is given by the TPC trough the measurement of the charge collection time. This is the time electrons need to travel from the original production point, along the ionisation track, towards the Micromegas pads. The z coordinate (z_{point}) of each point of Fig. 3.2 was obtained:

$$z_{point}[mm] = t[bin] \cdot T[ns/bin] \cdot v_{drift}[mm/ns] \tag{3.2}$$

The time of collection of electrons, indicated with t, is measured in bin by the electronics and has to be converted in fraction of seconds. With 50 MS/s being selected as sampling frequency for the simulation of GET, the period of time corresponding to a single bin is T = 20 ns/bin. v_{drift} is the electron drift velocity inserted as input in the simulation.

The 3D trajectory of each particle can thus be obtained as shown in Fig. 3.3, where a representation of a 3D portion of the active volume of SpecMAT is shown. The blue line is a visualisation of the helix trajectory inside the TPC volume. In Fig. 3.4 the projection over the X-Z plane and the Y-Z plane of the ionisation track generated in the gas volume and the whole helical trajectory are reported for completeness.

The circular helix can be described by the following parametric equations:

$$x(\theta) = rcos(\theta) + X_{Center} \tag{3.3}$$

$$y(\theta) = rsin(\theta) + Y_{Center} \tag{3.4}$$

$$z(\theta) = \frac{p}{2\pi}(\theta - \Phi) = \frac{(\theta - \Phi)}{\Omega} \tag{3.5}$$

where r and X_{center}, Y_{center} are respectively the radius and the x, y coordinates of the center obtained by the circular fit. The angle θ, the independent variable, is the angle which the radius (which connects the considered point and the circle's center) forms with the x-axis, while Φ is the initial angle value. p is the pitch, the helix path along the z axis between two consequential spires. As deduced from the eq. 3.5, Ω is defined as $\Omega = \frac{2\pi}{p}$.

In function of z, the equations for x and y become:

$$x(z) = rcos(\Omega z + \Phi) + X_{Center} \tag{3.6}$$

$$y(z) = rsin(\Omega z + \Phi) + Y_{Center} \tag{3.7}$$

From the helix fit it is possible to measure the angle β of the helix with respect to the z-axis, which is the polar angle of emission of the ^{3}He particle with respect to the axis of the TPC.

From geometric considerations:

$$tan(\beta) = 2\pi r/p = r\Omega \tag{3.8}$$

Being the angle value measured in radians, the value of β in degrees is:

$$\beta\ [deg] = tan^{-1}(r\Omega) \cdot 180/\pi \tag{3.9}$$

3.2 Q-value from Radius Vs Polar Angle

For each event, from the circular fit of the 2D projection of the ^{3}He track, the circle radius was obtained. For the same event, from the helical fit of the 3D trajectory of ^{3}He inside the TPC, the polar angle of the particle emission with respect the TPC axis was also obtained.

These two parameters have been correlated in a graph which is reported in Fig. 3.5, with the polar angle as a function of the radius. In figure, two separated regions are visible. They enclose the radius and β parameters of the ^{3}He particles generated by a transfer reaction in which the ^{87}Kr nucleus was produced in the ground state or in an excited state (the events corresponding to the two excited states at 1.470 MeV and 1.420 MeV cannot be distinguished). The observed limit value of the polar angle of ^{3}He emission ($\sim 50°$) is the maximum value allowed by the kinematics of the transfer reactions simulated. The kinematics curve of the α(^{86}Kr,^{3}He)^{87}Kr is reported in Fig. D.2 of Appendix D.

From these two parameters of the ^{3}He ejectile it was possible to reconstruct the dynamics of the transfer reaction occurred for each event acquired by the electronics and to obtain the Q-value of the reaction.

In the simulation produced (as will be in future experiments at ISS/ISOLDE), both an electric and a magnetic field are applied inside the active volume of SpecMAT. The fields are responsible for the helical 3D trajectory of the charged particle generated by simulation. The charged particles indeed experience the Lorentz force $\mathbf{F}_{Lor}$= q($\mathbf{E}$ + $\mathbf{v}$ x $\mathbf{B}$) which is due to the electromagnetic field. In the formula, $\mathbf{E}$ is the electric field, $\mathbf{B}$ is the magnetic field, $\mathbf{v}$ is the velocity of the particle and q its charge. With $\mathbf{v}$ x $\mathbf{B}$ the cross product between the two vectors is denoted.

Thanks to the magnetic component of the Lorentz force, when a charged particle travels through a magnetic field it experiences a force that causes its trajectory to deflect. By reconstructing the radius of curvature of the charged particle (in our case ^{3}He particles) trajectory, it is possible to calculate its velocity $\mathbf{v}$.

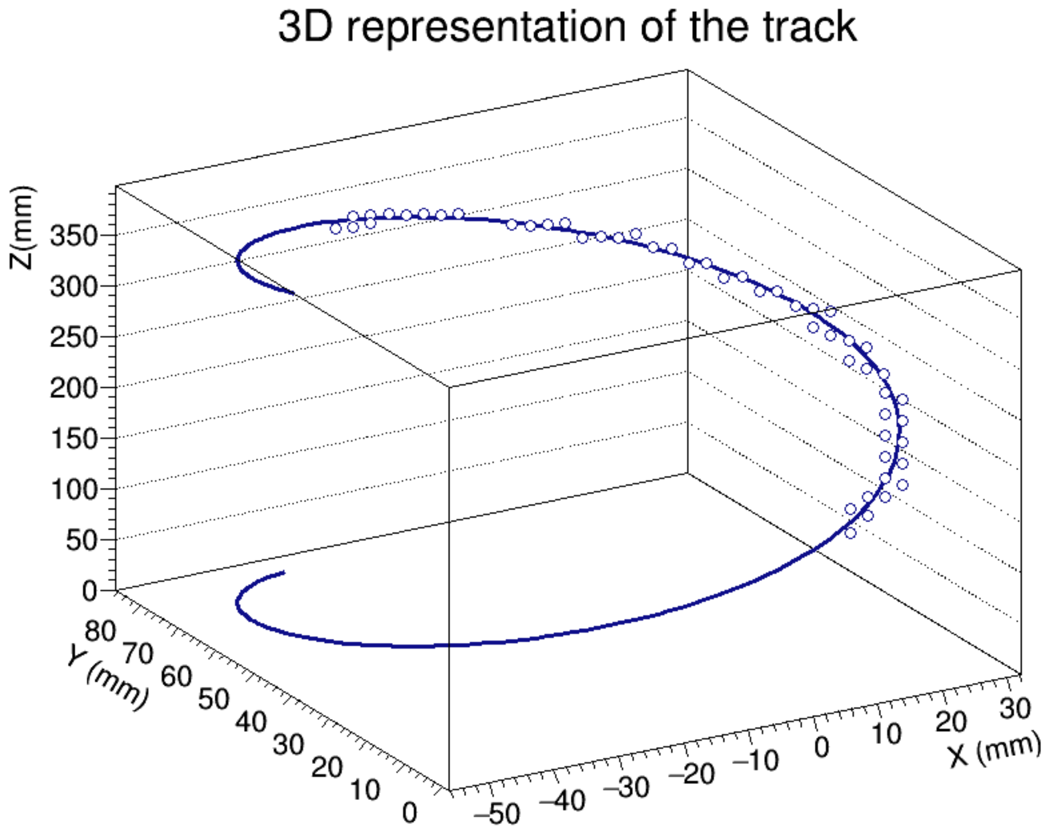

Figure 3.3: Visualisation of the 3D ionisation track generated by ^{3}He crossing the active volume of SpecMAT (points) and reproduced by the 2D projection of Fig. 3.2 and the charge collection time. The 3D volume represents a portion of the SpecMAT TPC, being X-Y the plane of Micromegas and the Z axis the TPC axis. The whole helix trajectory inside the TPC volume is represented by the blue line.

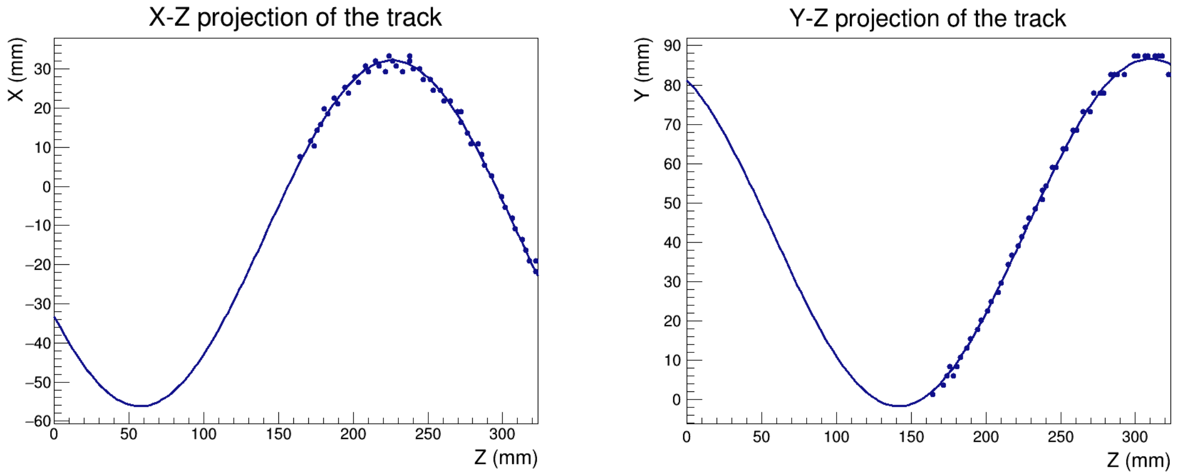

Figure 3.4: Projection on the X-Z plane (left) and on the Y-Z plane (right) of the ionisation track of Fig. 3.3

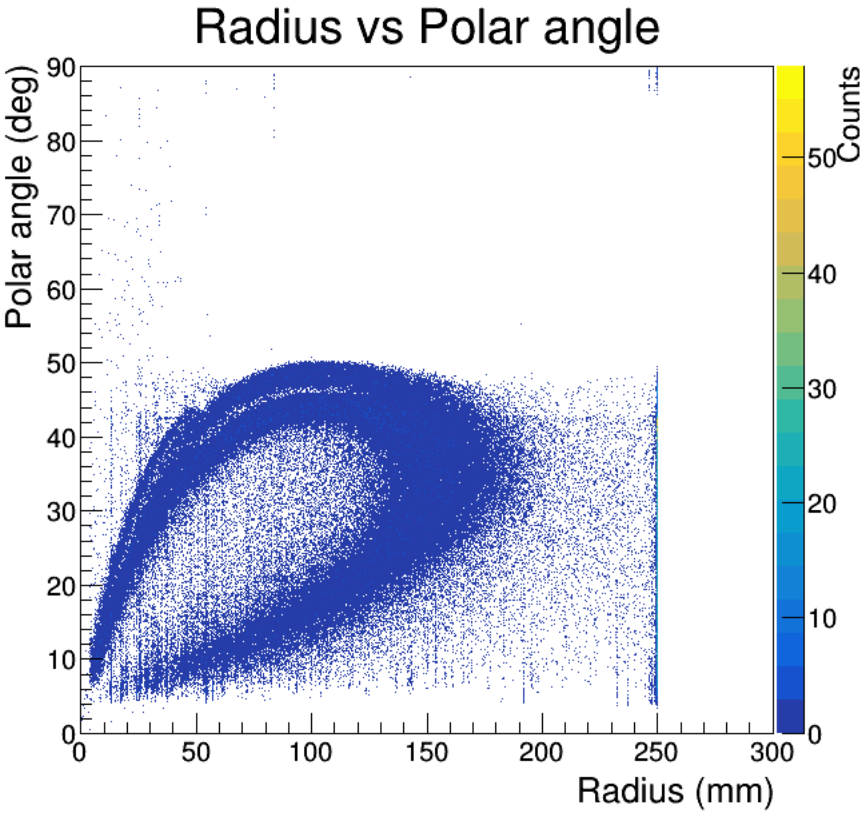

Figure 3.5: Correlation graph of the ^{3}He polar angle of the helical trajectory as a function of the circle radius. The limit value of the polar angle emission ($\sim 50°$) is the maximum value allowed by the kinematics of the transfer reactions simulated. The limit on the radius (250 mm) was imposed for the fits of the circular tracks. Two separated regions are visible at the top.

By comparison of the Lorentz force and the general centripetal force:

$$qv_{\perp}B = m\frac{v_{\perp}^2}{r} \tag{3.10}$$

where $v_{\perp}$ is the velocity perpendicular to the direction of the magnetic field.

$$v_{\perp} = vsin(\theta) \qquad \mathbf{v} = \mathbf{v}_{\parallel} + \mathbf{v}_{\perp} \tag{3.11}$$

By considering from now the specific case of the $\alpha(^{86}\mathrm{Kr},^{3}\mathrm{He})^{87}\mathrm{Kr}$ transfer reaction, the total velocity (in the laboratory frame) of the ejectile (indicated as $v(^3He)$) can be obtained:

$$v(^3He) = \frac{qrB}{sin(\theta)m(^3He)} \tag{3.12}$$

and hence its energy $E(^3He)$.

$$E(^3He) = \frac{mv^2(^3He)}{2} \tag{3.13}$$

In order to measure the Q-value of the reaction, the initial energy and the final energy of the Center-of-Mass of the system (CM) have to be obtained.

The initial motion of the CM (in the laboratory frame) can be easily reconstructed in the entrance channel, before the reaction occurs. From the momentum conservation the initial velocity of the CM $V_{CM,in}$ can be measured as:

$$V_{CM,in} = v_{beam}\frac{m(^4He)}{(m(^{86}Kr) + m(^4He))} \tag{3.14}$$

The tabulated values in atomic masses [u] of the nuclei considered (both in the entrance and exit channel), were converted to [MeV/c^2] for the calculations through the conversion factor 931.5 MeV/u. The precise value of the masses of isotopes inserted in the calculations were taken from [19].

The masses values (in atomic unit) for the nuclei in the entrance and exit channel are reported in Tab. 3.1.

	$m(^{86}Kr)$	$m(^4He)$	$m(^{87}Kr)$	$m(^3He)$
$mass(u)$	85.9106	4.0026	86.9134	3.0160

Table 3.1: Tabulated value of isotope masses (in atomic unit). Only 4 decimals are reported for each value. Refer to [19] for the precise values.

The velocity of the beam nucleus v_{beam} in the equation can be measured from the value in energy that was set as input parameter in the simulation (E_{beam} = 7·86 MeV/u, where 86 is the mass number of the beam nucleus $m(^{86}Kr)$):

$$v_{beam} = \sqrt{\frac{2E_{beam}}{m(^{86}Kr)}} \tag{3.15}$$

The initial energy of the CM, with respect to the laboratory frame, can be defined as:

$$E_{CM,in} = \frac{1}{2}m(^4He)V_{CM,in}^2 + \frac{m(^{86}Kr)}{2}(v_{beam} - V_{CM,in})^2 \tag{3.16}$$

It is then possible to compute $E_{CM,in}$ by taking into account only the masses of isotopes in the entrance channel and the energy of the beam nucleus:

$$E_{CM,in} = \frac{m(^4He)E_{beam}}{m(^4He) + m(^{86}Kr)} \tag{3.17}$$

In order to compute the final energy of the CM, $E_{CM,fin}$, for geometric considerations, the following formula ([58]) was used:

$$E_{CM,fin} = E(^3He) + \frac{m(^3He)V_{CM,in}^2}{2} - \frac{m(^3He)V_{CM,in}z(^3He)}{T_{cyc}} \tag{3.18}$$

$z(^3He)=v_{\parallel}T_{cyc}$ is the distance along the z-axis the ^{3}He travels in a single loop of the helix. T_{cyc} is the period of the helix trajectory that can be measured:

$$T_{cyc} = \frac{2\pi r}{v_{\perp}(^3He)} = \frac{2\pi m(^3He)}{Bq} \tag{3.19}$$

where the radius of curvature $r = \frac{m(^3He)v_{\perp}(^3He)}{qB}$ has been substituted in the formula.

The Q-value of each reaction simulated can be now be measured as:

$$Q = E_{CM,fin} - E_{CM,in} \tag{3.20}$$

The values obtained were reported in a graph, in the Q-value spectrum of Fig. 3.6. The two peaks in figure correspond to the Q-values of transfer reactions in which the ^{87}Kr isotope was produced in the ground state or in an excited state.

It is then possible to make the substitutions:

$$Q = Q_{g.s.} + E_{ex}(^{87}Kr) \qquad Q_{g.s.} = m(^4He)c^2 + m(^{86}Kr)c^2 - m(^3He)c^2 - m(^{87}Kr)c^2 \tag{3.21}$$

where $E_{ex}(^{87}Kr)$ is the excitation energy level of ^{87}Kr that is populated in the reaction and $Q_{g.s.}$ is the Q-value of the reaction when ^{87}Kr is produced in the ground state ($Q_{g.s.} \sim$ -15.06 MeV). By using these substitutions, the excitation energy $E_{ex}(^{87}$Kr) of the populated shell level of ^{87}Kr can be computed:

$$E_{ex}(^{87}Kr) = E_{CM,in} + Q_{g.s.} - E_{CM,fin} \tag{3.22}$$

The values obtained for the excitation energies were plotted in the graph shown on the right of Fig. 3.6.

The values of the Q-value and of the excitation energies were obtained by fitting the peaks in each spectrum. In each spectra two peaks are visible. One contains the reaction events in which $E_{ex}(^{87}$Kr) is produced on the ground state and the other to excited states. The peaks relative to the events in which an excited state of ^{87}Kr was populated contain both the two excited levels simulated,

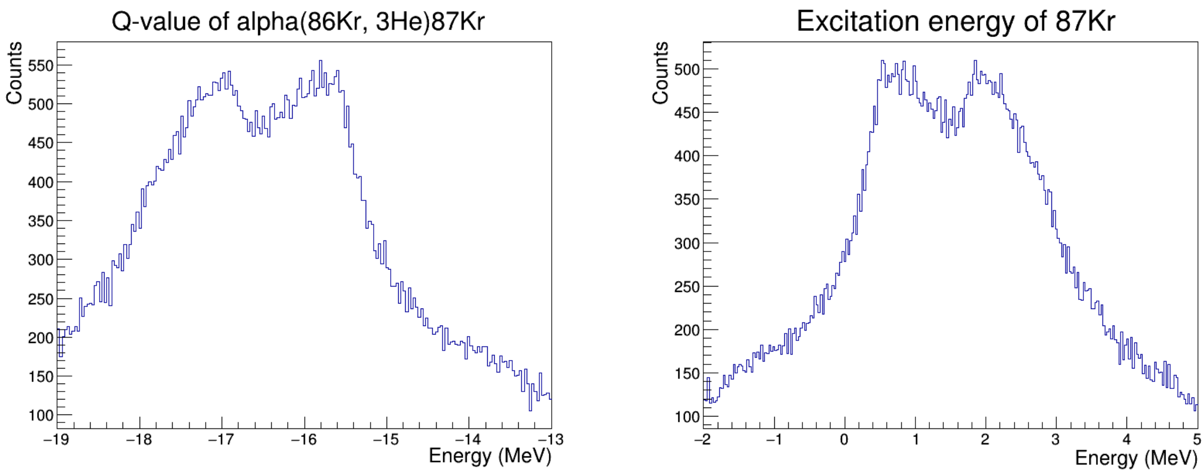

Figure 3.6: Spectrum of the Q-value of the reactions produced by the simulations (left). The two peaks in figure correspond to the Q-values of transfer reactions in which the ^{87}Kr isotope was produced in the ground state or in an excited state. The two peaks in the excitation energy spectrum (right) enclose the energies of the ground state and excited levels populated in the reactions.

	Energy g.s. (MeV)	**Energy excited states (MeV)**
Q_{value}	-15.71 ± 0.02	-17.11 ± 0.04
FWHM(Q_{value})	0.75 ± 0.06	0.8 ± 0.2
$E_{ex}(^{87}Kr)$	0.65 ± 0.02	2.06 ± 0.08
FWHM($E_{ex}(^{87}Kr)$)	0.74 ± 0.06	1.2 ± 0.4

Table 3.2: Results obtained in the simulation. Q-value, E_{ex}(^{87}Kr) and FWHM.

at 1.476 MeV and 1.420 MeV. The energy gap ΔE between the ground state and the combination of the two excited states was measured from the excitation energy spectrum and it is ΔE = (1.41 ± 0.08) MeV.

The peaks are a bit shifted to the right. To obtain the Q_{value} and the E_{ex}(^{87}Kr) spectra, classic kinematics calculations were used. A next step could be to perform relativistic kinematics calculations in order to observe if a better value of the Q-value can be obtained.

3.3 Q-value from Energy Vs Polar Angle

From the simulated data it was also possible to obtain the energy of the ejectile ^{3}He nucleus as the sum of charge collected in pads for the single event considered. A correlation graph of the polar angle as a function of the energy collected on the Pad Plane was obtained and it is shown in Fig. 3.7.

By knowing the energy of the ejectile particle in the laboratory frame, the first part of the calculations illustrated in Section 3.2, up to eq. 3.13, can be skipped. By using the same formulas from eq. 3.14 it was then possible to reconstruct the Q-value of the $\alpha(^{86}$Kr,^{3}He)^{87}Kr transfer reaction and the excitation energy of ^{87}Kr, produced in the reaction. The spectra obtained are shown in Fig. 3.8.

The results obtained are reported in table 3.3. With this method, only the events in which the tracks of the ejectile particles are confined inside the active volume of SpecMAT contribute to the Q-value measurement. Indeed, for the ^{3}He isotopes which escape the volume, the total energy cannot be reconstructed because of the energy loss that cannot be measured by the detector.

In the Energy - Polar angle plot, the two separated regions on the right contain the parameters which correspond to the confined particle tracks (a visualisation of the two regions can be seen in Fig. 4.9).

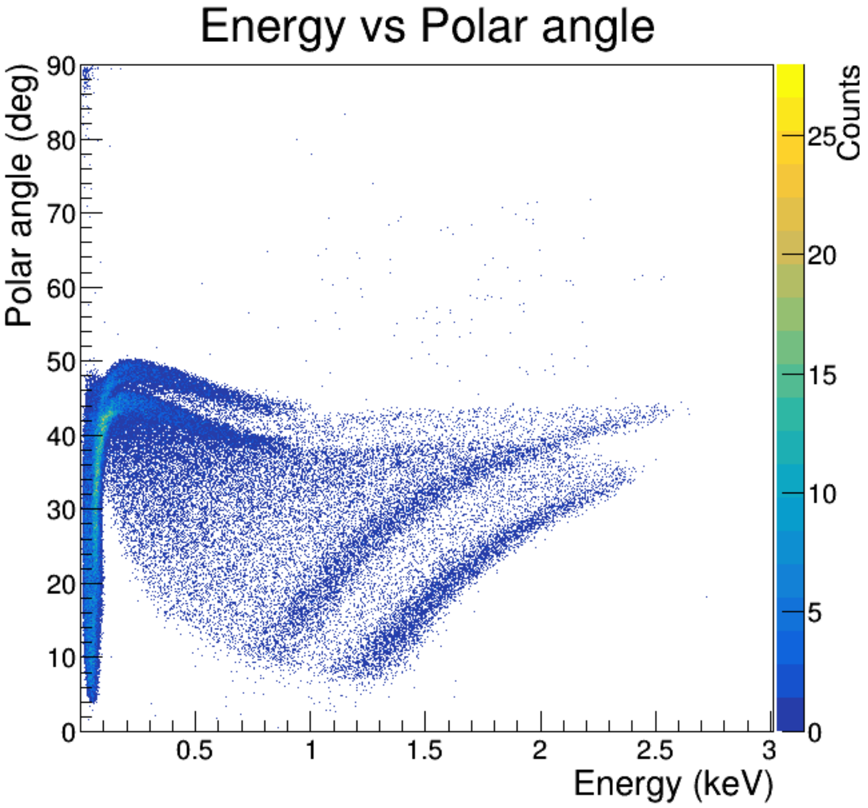

Figure 3.7: Correlation graph of the polar angle of ^{3}He emission as a function of its energy measured by the Pad Plane of SpecMAT (from the collected charge). The limit value of the polar angle (~ 50 degree) is the maximum value allowed by the kinematics of the transfer reaction. Two separated regions, corresponding to the events in which ^{87}Kr was produced in the ground states or in an excited stare, are visible.

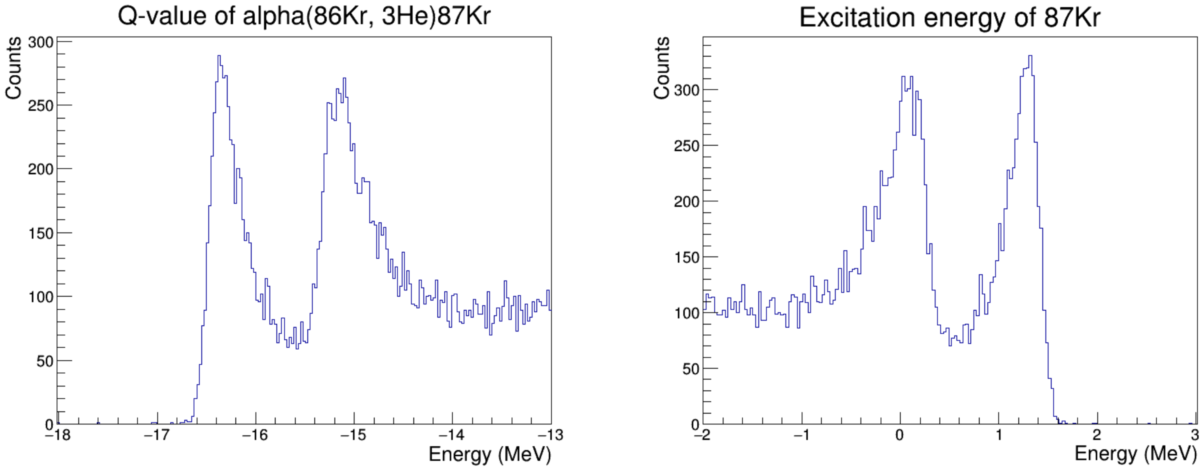

Figure 3.8: Spectrum of the Q-value of the $\alpha(^{86}\text{Kr},^{3}\text{He})^{87}\text{Kr}$ transfer reaction (left) and excitation energy spectrum of the ^{87}Kr produced in the reaction (right).

	Energy g.s. (MeV)	**Energy excited states (MeV)**
Q_{value}	-15.189 ± 0.009	-16.371 ± 0.007
FWHM(Q_{value})	0.30 ± 0.03	0.22 ± 0.03
$E_{ex}(^{87}Kr)$	0.092 ± 0.007	1.311 ± 0.007
FWHM($E_{ex}(^{87}Kr)$)	0.35 ± 0.02	0.23 ± 0.03

Table 3.3: The table contains the values of the Q-value of the $\alpha(^{86}\text{Kr},^{3}\text{He})^{87}\text{Kr}$ transfer reaction, the excitation energy of ^{87}Kr produced and the FWHM, obtained from the Energy Vs Polar Angle plot. The theoretical ground state Q-value, used to measure the excitation energy $E_{ex}(^{87}Kr)$ is ∼ -15.06.

The statistics for the energy spectra (in Fig. 3.8) is therefore lower with respect to the Q-value excited energy spectra obtained starting from the measurement of the track radius. The energy gap ΔE between the ground state and the combination of the two excited states as reconstructed from the excitation energy spectra is ΔE = (1.22 ± 0.01) MeV.

Although for most of the events in this simulation the ^{3}He particles escape the active volume, the events for which they are confined are the most interesting ones, because they correspond to small centre-of-mass scattering angles. Firstly the cross section is expected to be maximum for these angles, while in the simulation performed in this work an isotropic distribution was assumed; secondly, from data at small centre-of-mass angles it is possible to reconstruct the transferred angular momentum and thus put constraints on the spin of the populated states.

3.4 Analysis of confined/escaped tracks

In order to reduce unwanted background and improve the resolution in the Q-value and excitation energy spectra (Fig. 3.8) obtained from the ^{3}He energy information measured by the TPC of SpecMAT, the analysis was reproduced by considering only the events in which the whole particle track is kept inside the gas volume of the detector. An event was considered in the analysis only if no pads outside of a 100 mm radius were fired. In the left plot of Fig. 3.2 the circular limit used in the analysis is the black circular dashed line. The limit imposed on the z-axis was instead considered at z = 315 mm. If a hitted pad in one event was outside of at least one of the limits imposed, the event was rejected. The event shown in Fig. 3.4, taken as an example, corresponds to an escaped particle (because of the z limit) and was therefore rejected in this analysis.

In Fig. 3.9 the Energy vs Polar angle and the excitation energy graphs obtained by using only the events representative of particles that remain for all their motion within the limits of the active detector (called "confined tracks") are reported. The results of the fits on the two peaks in figure are indicated in Tab. 3.4. The energy gap value ΔE between the ground state and the combination of the two excited states is ΔE = (1.22 ± 0.05) MeV.

In order to complete the discussion, a final calculation was done for the events corresponding to ^{3}He escaped particles. For escaped particles it is not possible to reconstruct the energy of the ejectiles starting from the collected charge on the Pad Plane but it is possible to reconstruct the dynamics of the transfer reaction by using the information of the ^{3}He track radius. From the Radius vs Polar angle graph for the event in which ^{3}He escaped, it is still possible to evaluate the Q-value of the reaction and the excitation energy of the ^{87}Kr isotopes produced. Furthermore, for the events in which the ejectile particles escape, the fitting process of the helix trajectory is more precise. Indeed the energy loss by a charged particle inside a gas follows the Bragg curve and the particle loses most of its energy at the end of the track. For the particles which escaped from the TPC the energy loss is minimised and the trajectory inside the volume of SpecMAT follows a more circular-based path. This allows to eliminate some background values due to a bad reconstruction of the circle radius. However, no substantial change in energy resolution was observed with respect to the measurement in which all

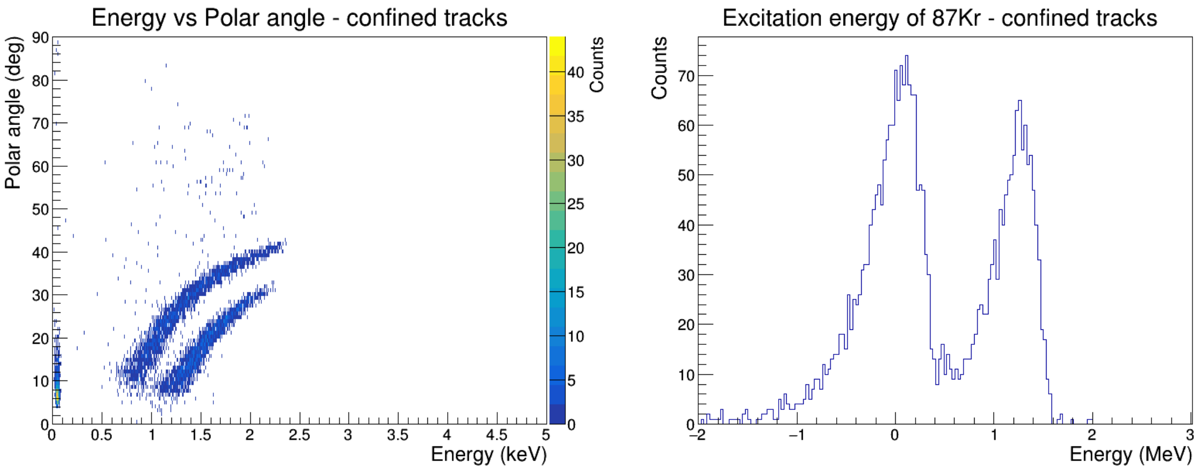

Figure 3.9: Correlation graph between the polar angle of emission and the energy of ^{3}He particles confined within the TPC volume of SpecMAT (left). Spectrum of the measured excitation energy of the nuclear states of the ^{87}Kr isotope produced in the $\alpha(^{86}\mathrm{Kr},^{3}\mathrm{He})^{87}$Kr transfer reaction, for the events in which the ^{3}He particle was confined (right).

events were considered. The graphs obtained for the escaped tracks are shown in Fig. 3.10.

	Energy g.s. (keV)	**Energy excited states (keV)**
$\mathrm{E}_{ex}(^{87}Kr)$	0.1 ± 0.05	1.32 ± 0.02
$\mathrm{FWHM}(\mathrm{E}_{ex}(^{87}Kr))$	0.3 ± 0.3	0.3 ± 0.1

Table 3.4: The table contains the values of the excitation energy of ^{87}Kr produced in the $\alpha(^{86}\mathrm{Kr},^{3}\mathrm{He})^{87}$Kr reaction and the FWHM measurements of the energy resolution, measured by fitting the peaks in the spectra obtained starting from the Energy Vs Polar Angle plot for confined ^{3}He particles (Fig. 3.9).

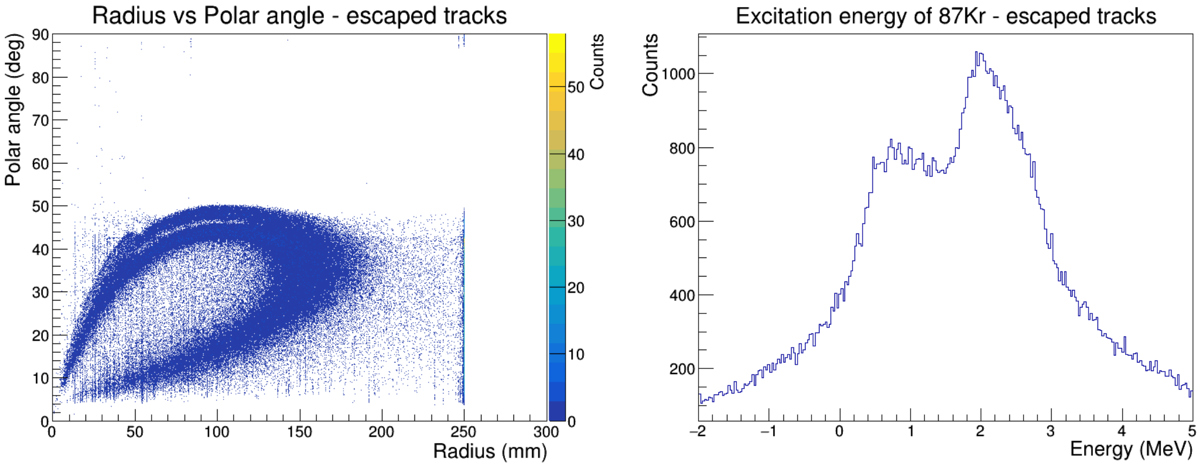

Figure 3.10: Correlation graph between the polar angle of emission and the track radius of the ^{3}He particles which escape from the TPC volume of SpecMAT (left). Spectrum of the measured excitation energy of the nuclear states of the ^{87}Kr isotope produced in the $\alpha(^{86}\mathrm{Kr},^{3}\mathrm{He})^{87}$Kr transfer reaction, for the events in which the ^{3}He particle escaped (right).

The excitation energy of ^{87}Kr and the FWHM obtained from the energy spectra in Fig. 3.10 are reported in Tab. 3.5. The ΔE energy gap between the ground state and the excited states was calculated and the value obtained is $\Delta\mathrm{E} = (1.39 \pm 0.02)$ MeV.

One of the reasons which cause a lower energy resolution in the energy spectra obtained by using the

	Energy g.s. (keV)	**Energy excited states (keV)**
$E_{ex}(^{87}Kr)$	0.64 ± 0.02	2.03 ± 0.01
$FWHM(E_{ex}(^{87}Kr))$	0.70 ± 0.06	1.4 ± 0.1

Table 3.5: The table contains the values of the excitation energy of ^{87}Kr produced in the α(^{86}Kr,^{3}He)^{87}Kr reaction and the FWHM measurements of the energy resolution, measured by fitting the peaks in the spectra obtained starting from the Radius Vs Polar Angle plot for escaped ^{3}He particles (Fig. 3.10).

radius parameter can still be attributed to the circular fits applied in the analysis. Further investigation on this aspect could be performed by measuring the radius of ^{3}He tracks using a model for fitting which takes into account the energy loss of the ejectile inside the TPC volume of SpecMAT.

Chapter 4

Conclusion

In this thesis, the performance of the SpecMAT active target was evaluated with a measurement of α-decays in a helium gas mixture. Then a simulation of the $\alpha(^{86}\mathrm{Kr},^{3}\mathrm{He})^{87}\mathrm{Kr}$ transfer reaction was made for the evaluation of the feasibility to study this reaction with the SpecMAT detector in future experiments.

The SpecMAT active target was assembled at KU Leuven and for the first time it was characterised with off-line measurements of α-decay of ^{239}Pu, ^{241}Am and ^{244}Cm isotopes in a He(98%)CF$_4$(2%) gas mixture at 1000 mbar. The characterisation was carried out also with a Ar(95%)CF$_4$(5%) gas mixture at 400 mbar, in order to reproduce the measurements previously performed with SpecMAT ([53]) and to compare the performance of the detector in both gas mixtures.

By studying the signal generated by the alpha particles in the TPC and by the γ-rays in the scintillator array it was possible to observe in all the measurements the correlation between 5485.6 keV α-particles and 59.5 keV γ-rays emitted in the ^{237}Np decay (daughter nucleus of ^{241}Am). Energy spectra of the α-particles based on their track length within the TPC volume were obtained. Similar to the case of the argon gas, the three isotopes of the alpha source can be distinguished in the helium gas mixture. This confirms that this gas mixtures can be used in SpecMAT for detection of the charged particles emitted in nuclear reactions. The measured energy resolution is $\sim$ 185 keV in the argon gas mixture (400 mbar, -5 kV cathode voltage, -240 V voltage at the mesh of the micromegas) and $\sim$ 146 keV in the helium mixture (1000 mbar, -5.7 kV cathode voltage, -240 V at the mesh of the micromegas), at $\sim$ 5.5 MeV α-particles.

Energy spectra based on the amount of ionisation electrons collected with the pad plane, were obtained for both argon and helium gas mixtures. With the argon gas mixture the energy resolution of the energy spectrum is $\sim$ 195 keV at $\sim$ 5.5 MeV. In presence of the helium gas it was not possible to obtain the energy spectrum with a separation of the three clusters of isotopes of the alpha source.

Moreover, while in the argon mixture it was possible to measure the half-life of the 59.5 keV populated state in ^{237}Np from the time coincidence spectrum, this was not the case in the helium mixture.

In this work were excluded several aspects that may lead to the worsening of the energy and timing resolution in the helium gas mixture with systematic measurements and analysis of the detector performance under different conditions.

The pressure of the argon mixture was lowered to reach the same track length of α-particles as in the helium mixture. Nevertheless was measured almost no degradation in the detector performance under such conditions in the argon gas mixture, which excludes the geometrical factor of the TPC in the worsening of the observed resolution.
To exclude the worsening of the timing resolution with the low sampling frequency of the GET electronics that was used for the measurements in the He(98%)CF$_4$(2%) gas mixture, the similar GET

settings were used in Ar(95%)CF$_4$(5%) measurements. Still no significant effect was observed that can cause similar worsening of the spectra as in the helium mixture case.
Also the electron amplification in the pad plane was increased with elevated polarisation values of the mesh. Such settings did not improve the observed spectra.

As a conclusion on the investigation conducted, it was evaluated that the lower performances of the He(98%)CF$_4$(2%) gas mixture can be due to the difference in motion of electrons comparing to the Ar(95%)CF$_4$(5%) gas mixture.
The drift velocity of electrons in the helium mixture is nearly an order of magnitude smaller than in the argon gas, in the same values of the electric field generated within the TPC during the measurements. The drift velocities are $\sim$ 0.1 mm/ns in argon gas and $\sim$ 0.01 mm/ns in helium mixture. It is hence possible that the electrons in helium recombine with the gas atoms and diffuse much more with respect to the electrons in argon gas, causing worse performance of this helium gas mixture.

A future step to investigate the performance of SpecMAT in helium gas could be to perform a characterisation measurement by adding a higher concentration of CF$_4$ quencher gas to helium gas. Thanks to this addition higher voltages could be applied to the TPC electrodes, so increasing the electrons drift velocity. This parameter will thus allow to study the effect of even higher drift velocities of electrons in the mixture on the resulting energy and timing resolutions.

Neverthless, the characterisation measurements of SpecMAT with the He(98%)CF$_4$(2%) gas mixture showed the feasibility to study the α(^{86}Kr,^{3}He)^{87}Kr reaction with the detector in this mixture relying only on the tracks length of the light ejectiles. A similar helium mixture could be used as a target for the α(^{86}Kr,^{3}He)^{87}Kr reaction.

The α(^{86}Kr,^{3}He)^{87}Kr transfer reaction was simulated with SPMTsim simulation with the Geant4 package. In this model, the collisions between the ^{86}Kr isotopes and the ^{4}He particles were simulated. 3D ^{3}He particle tracks were produced inside the TPC volume of SpecMAT. The energy beam was set at 7 MeV/u and an applied magnetic field of 2.5 T was simulated inside the TPC volume, in order to reproduce the working condition of SpecMAT inside the ISS at ISOLDE/CERN. Reactions to the ground state and to the two low-lying excited states in the ^{87}Kr isotope at $\sim$ 1.420 MeV and at $\sim$ 1.476 MeV were reproduced in this simulation.

From the radius of the ^{3}He particles tracks and its emission angle, obtained from the helical function fit, it was possible to reconstruct the kinematics of the reactions produced.
The Q-value of the reaction measured for the events in which the ^{87}Kr was produced in its ground state was Q_{value}= (-15.71 ± 0.02) MeV, while for the events in which the excited states were populated is Q_{value} = (-17.11 ± 0.04) MeV (the two excited states were indistinguishable and only one Q-value was extracted for these two states).
These values correspond to the excitation energy $E_{g.s}$ = (0.65 ± 0.02) MeV for the ground state and E_{ex} = (2.06 ± 0.08) MeV for the excited states.
In the obtained spectrum it was not possible to distinguish the events corresponding to the two different excited states that were populated in the simulation. Furthermore, the ground state Q-value obtained differs from the Q-value in literature (Q_{value} $\sim$ -15.06 MeV).
The difference in energy between the ground and the excited states was measured from the excitation energy spectra and it is ΔE = (1.41 ± 0.08) MeV. This value is compatible with the simulated energy levels.

The Q-value and excitation energy were also measured by using the charge collected (and simulated) on the pad plane. The uncertainty that can arise from the helix fits was thus removed. The values obtained for the excitation energy are $E_{g.s}$ = (0.092 ± 0.007) MeV for the ground state and E_{ex} = (1.311 ± 0.007) MeV for the excited state.
These results are more accurate and also have a better energy resolution with respect to the values obtained by using the radius information. It was still not possible to separate the two excited states.

Also, the difference in energy between the ground and the excited states, measured by this method is less accurate: $\Delta E = (1.22 \pm 0.01)$ MeV.

As the ^{3}He energy reconstruction is possible only for the particles confined inside the TPC volume in which they lose all their energy, the calculations were performed by studying only the events corresponding to confined particles. These events are referred to ^{3}He scatterings at small Centre-of-Mass (CM) angles and are the most important. Indeed, for small CM angles, it is possible to reconstruct the angular momentum transferred in the reaction and thus investigate the spin of the populated states in ^{87}Kr.
The analysis was then carried out also for the events with escaped ^{3}He particles for the reconstruction of the kinematics of the reaction using the radius parameter. For these particles the fits are more accurate thanks to a more exact circular trajectory generated by the ejectiles (because of the lower energy loss inside the volume).
In both cases, no substantial improvement was observed in the final results.

The lower energy resolution observed in the energy spectra, obtained by using the radius parameter, can be attributed to the circular fits applied in the analysis. By using a model for the fits of the ^{3}He tracks which takes into account the energy loss of the ejectile crossing the active volume of SpecMAT, a better energy resolution could be observed.

In order to separate the two excited states an improvement of the performed simulation could be done by adding the information from the scintillation array and by performing the measurements in coincidence. This will allow to correlate the α-particles with γ-rays emitted in the de-excitation of the populated states in ^{87}Kr and further rely on the resolution of the scintillation detectors.

Appendices

Appendix A

Calibration of the scintillation array

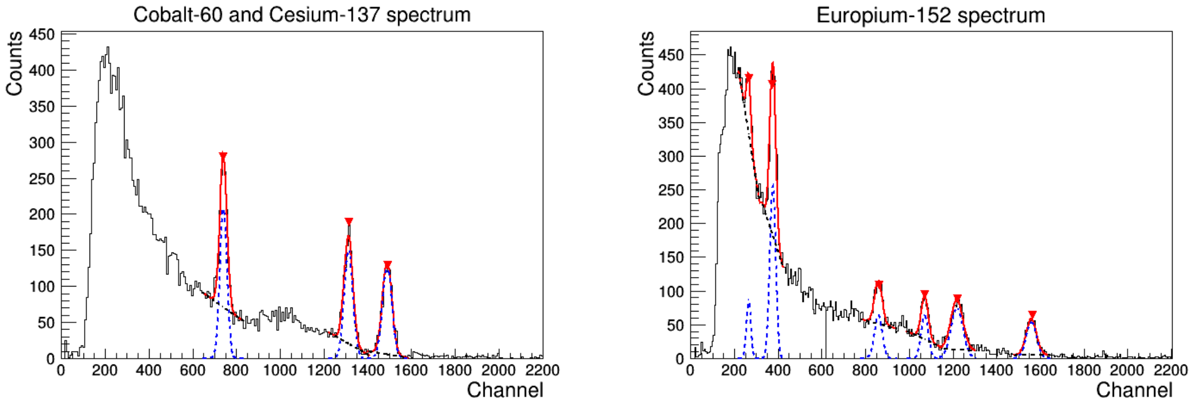

Figure A.1: Calibration spectra. The figure on the left represents the spectrum obtained from the detection of the γ-rays emitted from the decay of $^{60}_{27}$Co and $^{137}_{55}$Cs sources, placed outside and around the scintillation array. The figure on the right is the gamma spectrum obtained with a ^{152}Eu source, placed inside the TPC. The spectra shown were recorded by a single CeBr$_3$ crystal. Each spectrum was recorded by each crystal of the scintillation array. From the spectra recorded by each crystal, the peaks have been fitted by the convolution of a Gaussian (represented with the blue dashed line) and a first-order polynomial function (in the black dashed line) to remove the background from the photo-peak. The red lines represent the fits from which the centroids of the Gaussian have been obtained. A sampling frequency of 50 MS/s was set to GET electronics for the calibration measurement. The known energy values of the γ-rays used for the calibration: ~ 662 keV (Cobalt-60), ~ 1173 keV and ~ 1332 keV (Cesium-137), ~ 245 keV, ~ 344 keV, ~ 779 keV, ~ 964 keV, ~ 1408 keV (Europium-152).

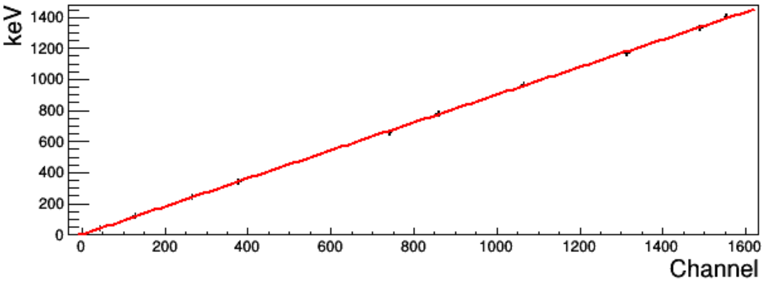

Figure A.2: Calibration plot for one CeBr$_3$ scintillator. On the x-axis the γ-rays energy registered in bin units by the crystal is reported. The y-axis reports the corresponding energy values in literature in keV. From the interpolation of the points (the red curve), the second-order polynomial function E [keV] = a*Channel^2 + b*Channel + c, was possible to obtain the a,b and c calibration parameters for the crystal. This procedure was applied for each crystal of the array.

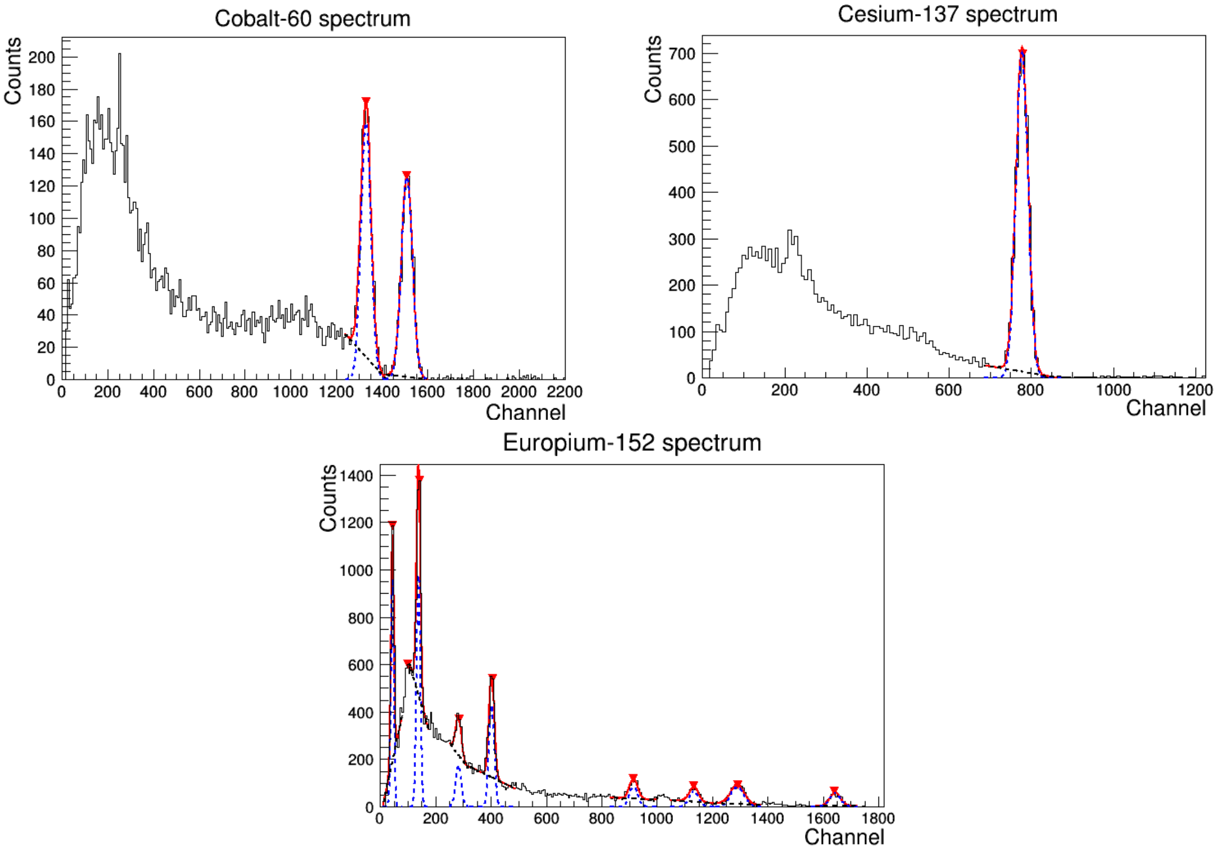

Figure A.3: Calibration spectra. The figures at represent the spectra obtained from the detection of the γ-rays emitted from the decay of $^{60}_{27}$Co, $^{137}_{55}$Cs and ^{152}Eu sources. All the sources were placed outside and around the scintillation array. The spectra shown were recorded by a single CeBr$_3$ crystal. Each spectrum was recorded by each crystal of the scintillation array. From the spectra recorded by each crystal, the peaks have been fitted by the convolution of a Gaussian (represented with the blue dashed line) and a first-order polynomial function (in the black dashed line) to remove the background from the photo-peak. The red lines represent the fits from which the centroids of the Gaussian have been obtained. A sampling frequency of 12.5 MS/s was set to GET electronics for the calibration measurement. The known energy values of the γ-rays used for the calibration: ∼ 662 keV (Cobalt-60), ∼ 1173 keV and ∼ 1332 keV (Cesium-137), ∼ 40 keV, ∼ 122 keV, ∼ 245 keV, ∼ 344 keV, ∼ 779 keV, ∼ 964 keV, ∼ 1408 keV (Europium-152).

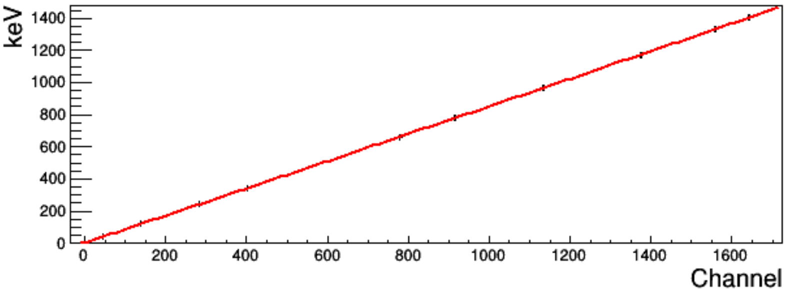

Figure A.4: Calibration plot for one CeBr$_3$ scintillator. On the x-axis the γ-rays energy registered in bin units by the crystal is reported. The y-axis reports the corresponding energy values in literature in keV. From the interpolation of the points (the red curve), the second-order polynomial function E [keV] = a*Channel^2 + b*Channel + c, was possible to obtain the a,b,c calibration parameters for the crystal. This procedure was applied for each crystal of the array.

Appendix B

Characterisation of SpecMAT - graphs

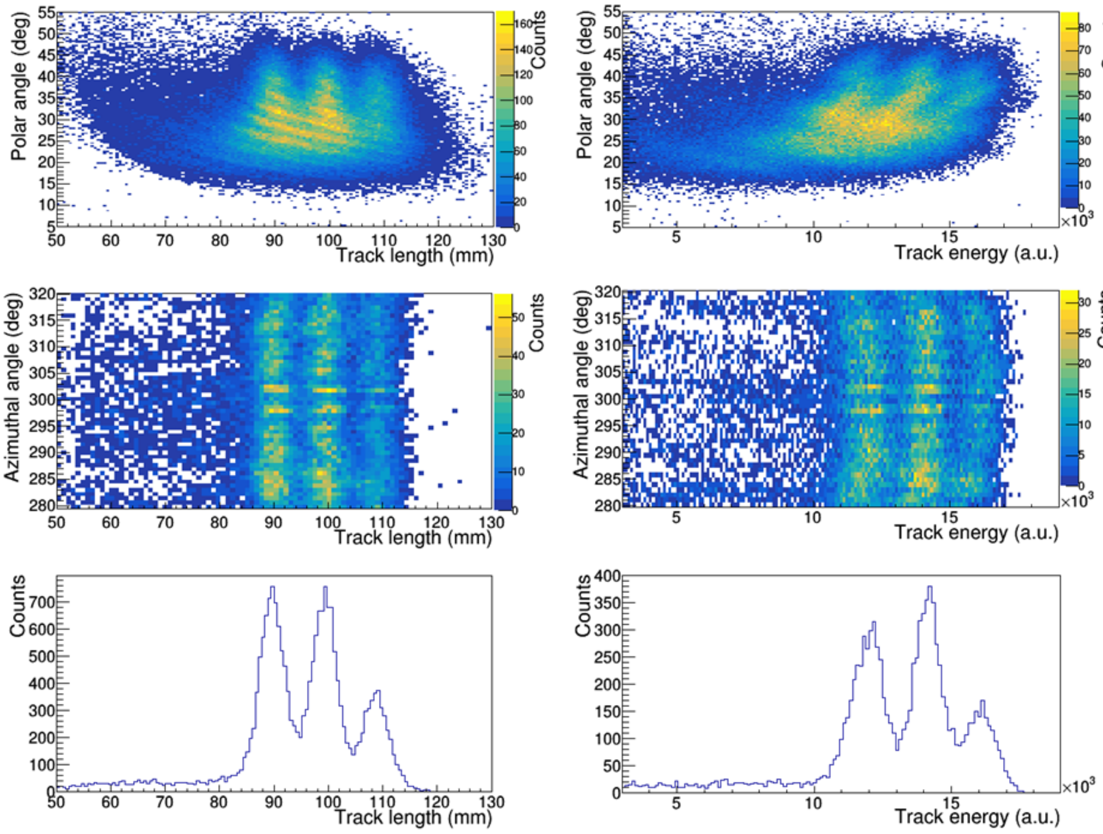

Figure B.1: Number of recorded events as function of the alpha tracks length and the angles of the particles emission, inside the active volume of the TPC (left). Number of recorded events as function of the deposited charge on the pad plane and the polar and azimuthal emission angles (right). The characterisation measurement was performed with a triple alpha source (^{239}Pu, ^{241}Am and ^{244}Cm) in a argon gas mixture Ar(95%)CF$_4$(5%) at 400 mbar. The internal multiplicity trigger and sampling frequency of 12.5 MS/s were set in GET electronics. The voltages applied to the TPC electrodes: cathode -5 kV, last inner electrode -240 V, mesh of Micromegas -250 V. The last external electrodes and the gas chamber were grounded. The plots on the left are based on the ionisation tracks length of the particles produced inside the TPC. The graphs on the right are based on the collected charge produced by the particles crossing the TPC volume. The zoom on the azimuthal angle was applied for a better visualisation of the data. The bottom figures represent the energy spectra of the alpha particles used for the measurement of energy resolution. The gates on the polar and azimuthal angles, together with the FWHM values obtained, are reported in Tab. C.1 - C.2 of Appendix C with reference to Argon run 2.

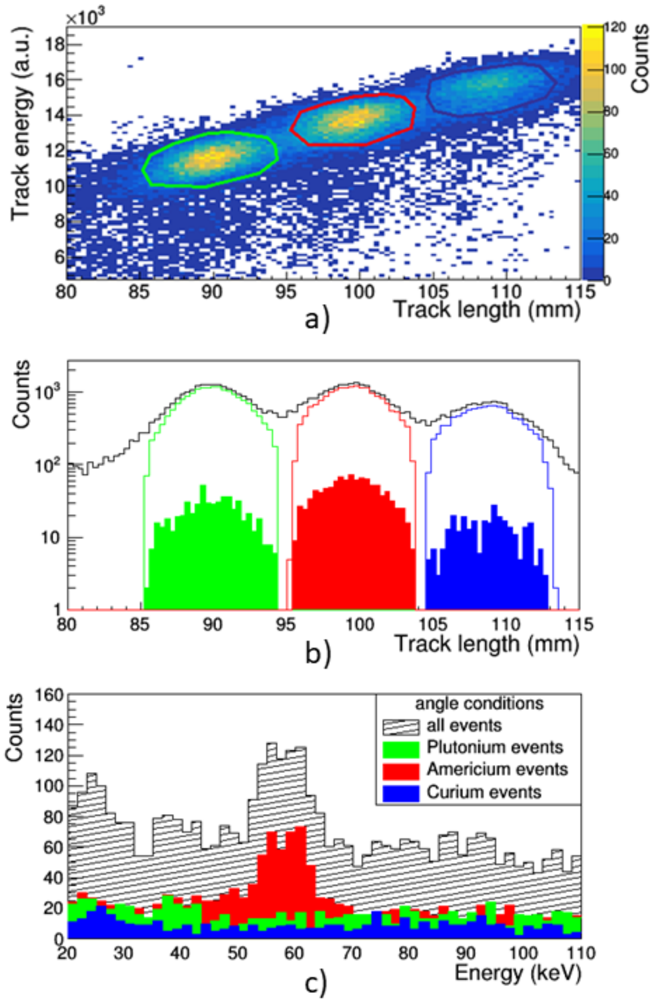

Figure B.2: Correlation plots. The characterisation measurement was performed with a triple alpha source (^{239}Pu, ^{241}Am and ^{244}Cm) in a argon gas mixture Ar(95%)CF$_4$(5%) at 400 mbar. The internal multiplicity trigger and sampling frequency of 12.5 MS/s were set in GET electronics. The voltages applied to the TPC electrodes: cathode -5 kV, last inner electrode -240 V, mesh of Micromegas -250 V. The last external electrodes and the gas chamber were grounded. A gate on the polar angle ($35° < \theta < 50°$) was applied. Fig. a) correlates the energy of the charged particles (measured as collected charge) and the tracks length. The three clusters highlighted enclose the events which correspond to the alpha decay of ^{239}Pu, ^{241}Am and ^{244}Cm. Respectively indicated in green, red and blue. The black histogram of Fig. b) was obtained by the projection of the top figure on the track length. The coloured-line peaks in the figure represent the events contained in each singular alpha cluster. The coloured-filled peaks in figure are constituted by particle events recorded in coincidence with γ-rays with an energy range 30 keV - 90 keV. Figure c) reports the total γ-rays spectrum in gray and the spectra with events relative to the γ-rays correlated to the alpha particles inside the clusters with fill-coloured histograms. The red peak at $\sim$ 60 keV contains the gammas emitted from the ^{237}Np decay (daughter nucleus of ^{241}Am).

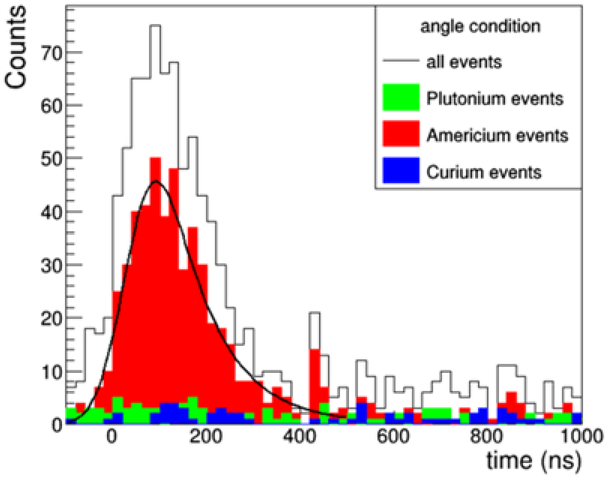

Figure B.3: Spectrum of time coincidences between the particle events recorded in the Micromegas and the γ-rays detected by the scintillation array. The characterisation measurement was performed with a triple alpha source (^{239}Pu, ^{241}Am and ^{244}Cm) in a argon gas mixture Ar(95%)CF$_4$(5%) at 400 mbar. The internal multiplicity trigger and sampling frequency of 12.5 MS/s were set in GET electronics. The voltages applied to the TPC electrodes: cathode -5 kV, last inner electrode -240 V, mesh of Micromegas -250 V. The last external electrodes and the gas chamber were grounded. The total spectrum represents all the data information on which the gate on the polar angle was applied. For the data shown as coloured histograms a further gate on the alpha particle clusters was applied. The exponential trends of the red histogram is due to the alpha decay of ^{241}Am and the subsequent gamma decay of ^{237}Np. In black, the fit used for the measurement of the half-life of ^{237}Np, which value obtained is reported in Tab. C.3 of Appendix C (with reference to Argon run 2), is shown.

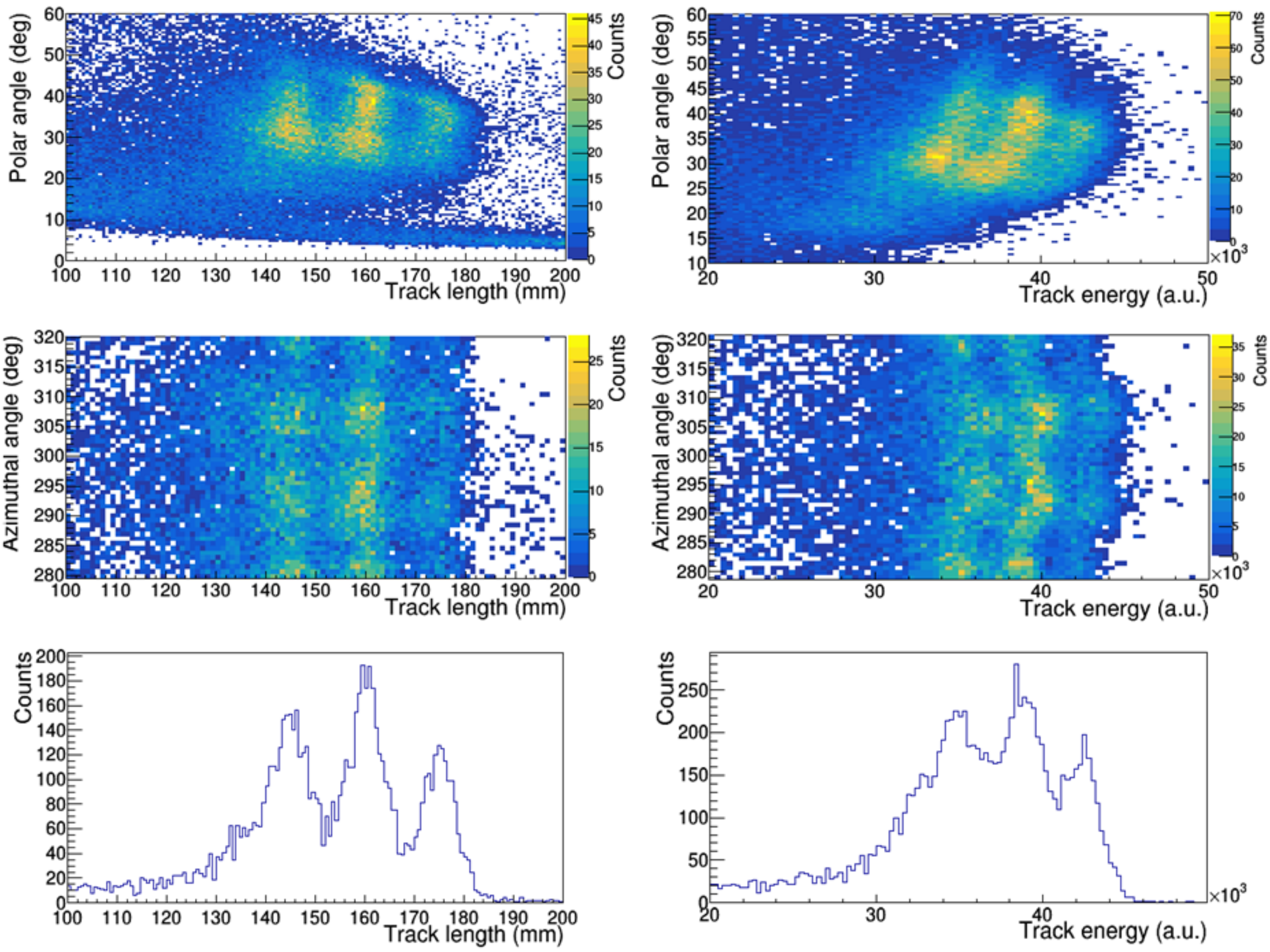

Figure B.4: Number of recorded events as function of the alpha tracks length and the polar and azimuthal angles of the particles emission, inside the active volume of the TPC (left). Number of recorded events as function of the deposited charge on the pad plane and the emission angle (right). The characterisation measurement was performed with a triple alpha source (^{239}Pu, ^{241}Am and ^{244}Cm) in a argon gas mixture Ar(95%)CF$_4$(5%) at 250 mbar. The internal multiplicity trigger and sampling frequency of 50 MS/s were set in GET electronics. The voltages applied to the TPC electrodes: cathode -2.8 kV, last inner electrode -240 V, mesh of Micromegas -250 V. The last external electrodes and the gas chamber were grounded. The plots on the left are based on the ionisation tracks length of the particles produced inside the TPC. The graphs on the right are based on the collected charge produced by the particles crossing the TPC volume. The zoom on the azimuthal angle was applied for a better visualisation of the data. The bottom figures represent the energy spectra of the alpha particles used for the measurement of energy resolution. The gates on the polar and azimuthal angles, together with the FWHM values obtained, are reported in Tab. C.1-C.2 of Appendix C with reference to Argon run 3.

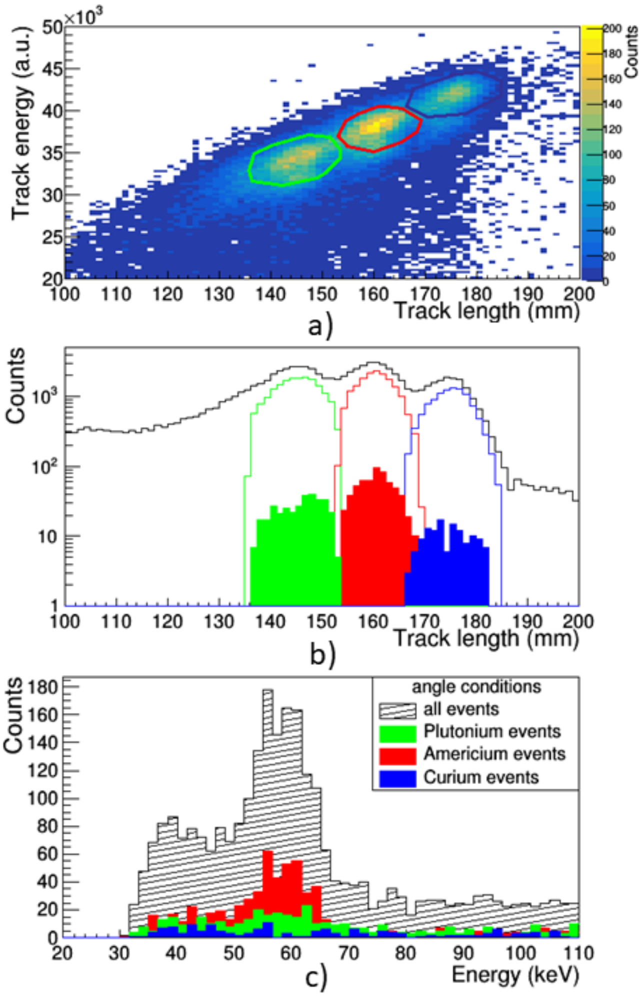

Figure B.5: Correlation plots. The characterisation measurement was performed with a triple alpha source (^{239}Pu, ^{241}Am and ^{244}Cm) in a argon gas mixture Ar(95%)CF$_4$(5%) at 250 mbar. The internal multiplicity trigger and sampling frequency of 50 MS/s were set in GET electronics. The voltages applied to the TPC electrodes: cathode -2.8 kV, last inner electrode -240 V, mesh of Micromegas -250 V. The last external electrodes and the gas chamber were grounded. A gate on the polar angle ($25° < \theta < 40°$) was applied. Fig. a) correlates the energy of the charged particles (measured as collected charge) and the tracks length. The three clusters highlighted enclose the events which correspond to the alpha decay of ^{239}Pu, ^{241}Am and ^{244}Cm. Respectively indicated in green, red and blue. The black histogram of Fig. b) was obtained by the projection of the top figure on the track length. The coloured-line peaks in the figure represent the events contained in each singular alpha cluster. The coloured-filled peaks in figure are constituted by particle events recorded in coincidence with γ-rays with an energy range 30 keV - 90 keV. Figure c) reports the total γ-rays spectrum in gray and the spectra with events relative to the γ-rays correlated to the alpha particles inside the clusters with fill-coloured histograms. The red peak at $\sim$ 60 keV contains the gammas emitted from the ^{237}Np decay (daughter nucleus of ^{241}Am).

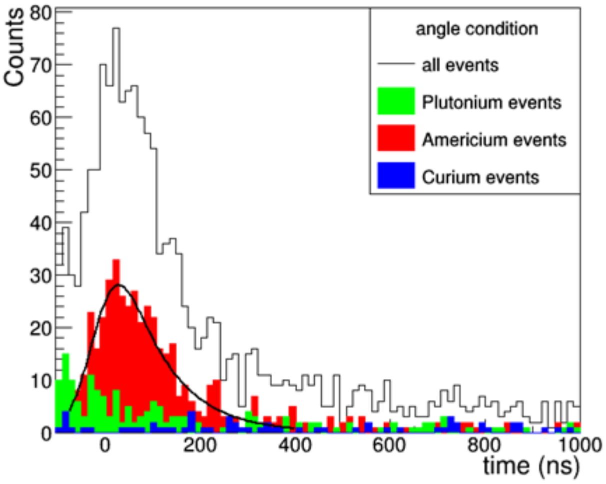

Figure B.6: Spectrum of time coincidences between the particle events recorded in the Micromegas and the γ-rays detected by the scintillation array. The characterisation measurement was performed with a triple alpha source (^{239}Pu, ^{241}Am and ^{244}Cm) in a argon gas mixture Ar(95%)CF$_4$(5%) at 250 mbar. The internal multiplicity trigger and sampling frequency of 50 MS/s were set in GET electronics. The voltages applied to the TPC electrodes: cathode -2.8 kV, last inner electrode -240 V, mesh of Micromegas -250 V. The last external electrodes and the gas chamber were grounded. The total spectrum represents all the data information on which the gate on the polar angle was applied. For the data shown as coloured histograms a further gate on the alpha particle clusters was applied. The exponential trends of the red histogram is due to the alpha decay of ^{241}Am and the subsequent gamma decay of ^{237}Np. In black, the fit used for the measurement of the half-life of ^{237}Np, which value obtained is reported in Tab. C.3 of Appendix C (with reference to Argon run 3), is shown.

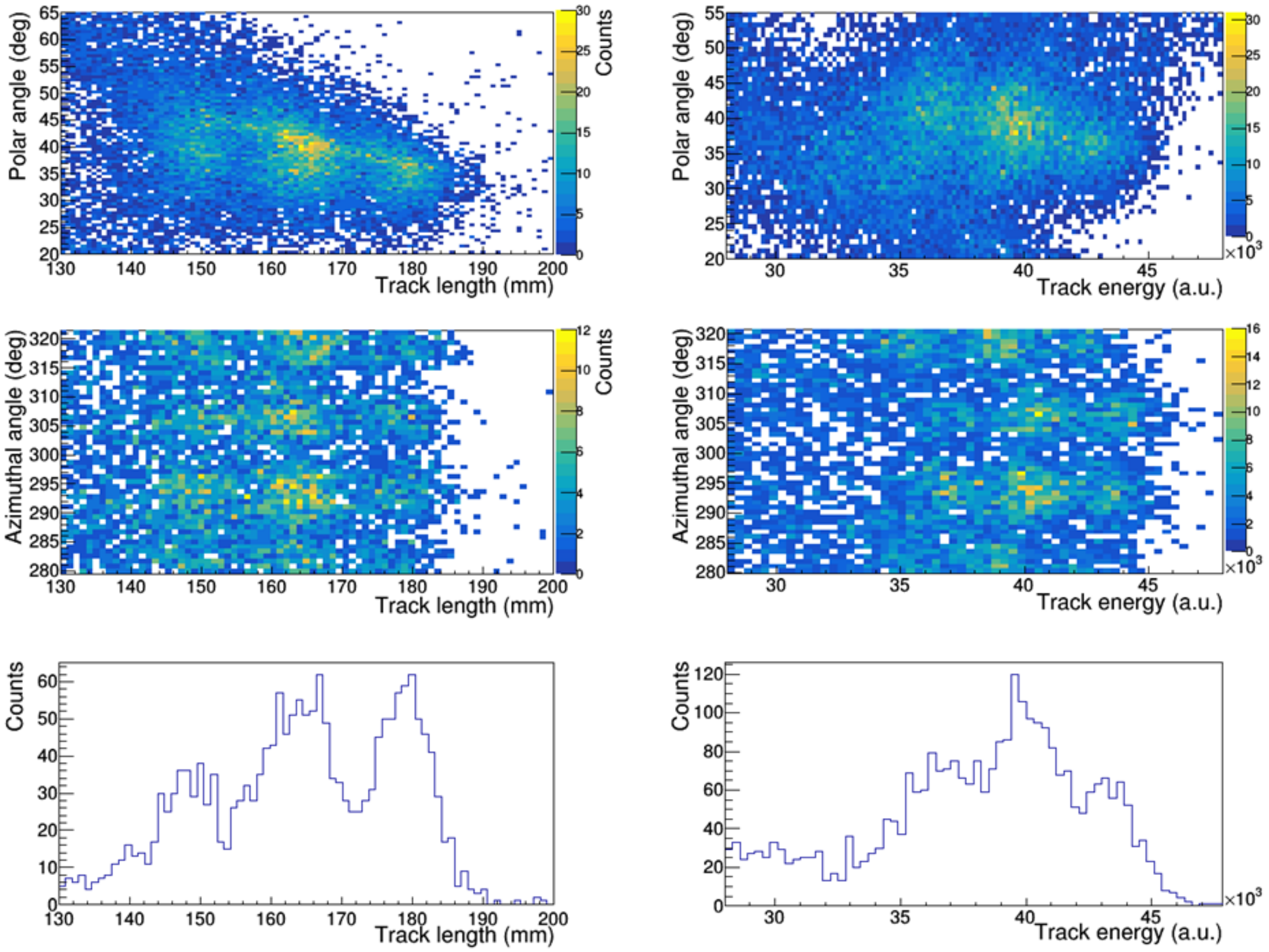

Figure B.7: Number of recorded events as function of the alpha tracks length and the polar and azimuthal angles of the particles emission, inside the active volume of the TPC (left). Number of recorded events as function of the deposited charge on the pad plane and the emission angle (right). The characterisation measurement was performed with a triple alpha source (^{239}Pu, ^{241}Am and ^{244}Cm) in a argon gas mixture Ar(95%)CF$_4$(5%) at 250 mbar. The internal multiplicity trigger and sampling frequency of 12.5 MS/s were set in GET electronics. The voltages applied to the TPC electrodes: cathode -2.8 kV, last inner electrode -240 V, mesh of Micromegas -250 V. The last external electrodes and the gas chamber were grounded. The plots on the left are based on the ionisation tracks length of the particles produced inside the TPC. The graphs on the right are based on the collected charge produced by the particles crossing the TPC volume. The zoom on the azimuthal angle was applied for a better visualisation of the data. The bottom figures represent the energy spectra of the alpha particles used for the measurement of energy resolution. The gates on the polar and azimuthal angles, together with the FWHM values obtained, are reported in Tab. C.1-C.2 of Appendix C with reference to Argon run 4.

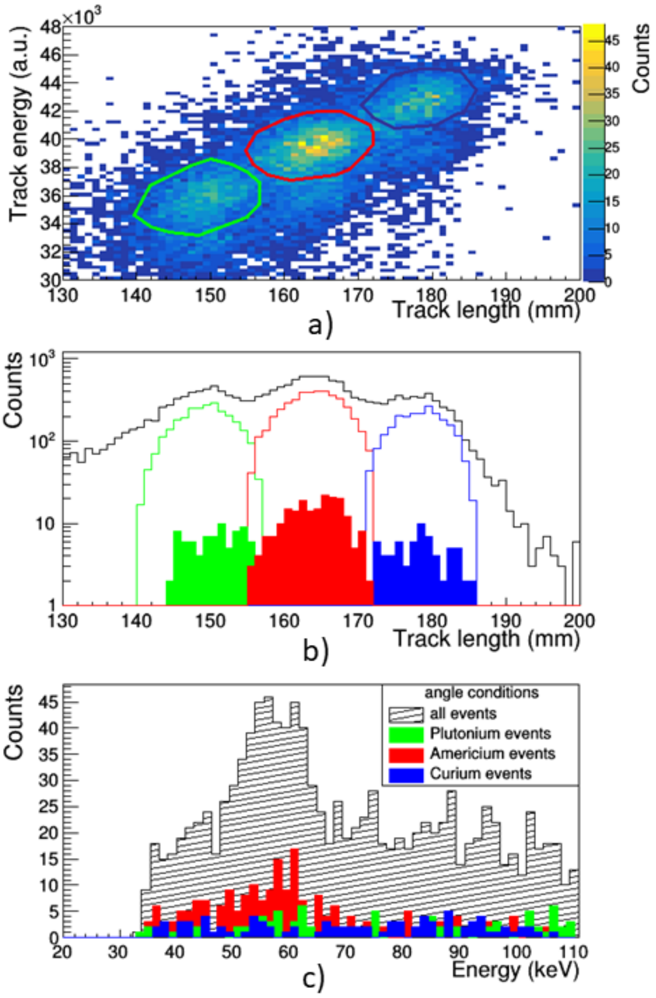

Figure B.8: Correlation plots. The characterisation measurement was performed with a triple alpha source (^{239}Pu, ^{241}Am and ^{244}Cm) in a argon gas mixture Ar(95%)CF$_4$(5%) at 250 mbar. The internal multiplicity trigger and sampling frequency of 12.5 MS/s were set in GET electronics. The voltages applied to the TPC electrodes: cathode -2.8 kV, last inner electrode -240 V, mesh of Micromegas -250 V. The last external electrodes and the gas chamber were grounded. A gate on the polar angle ($25^\circ < \theta < 46^\circ$) was applied. Fig. a) correlates the energy of the charged particles (measured as collected charge) and the tracks length. The three clusters highlighted enclose the events which correspond to the alpha decay of ^{239}Pu, ^{241}Am and ^{244}Cm. Respectively indicated in green, red and blue. The black histogram of Fig. b) was obtained by the projection of the top figure on the track length. The coloured-line peaks in the figure represent the events contained in each singular alpha cluster. The coloured-filled peaks in figure are constituted by particle events recorded in coincidence with γ-rays with an energy range 30 keV - 90 keV. Figure c) reports the total γ-rays spectrum in gray and the spectra with events relative to the γ-rays correlated to the alpha particles inside the clusters with fill-coloured histograms. The red peak at $\sim$ 60 keV contains the gammas emitted from the ^{237}Np decay (daughter nucleus of ^{241}Am).

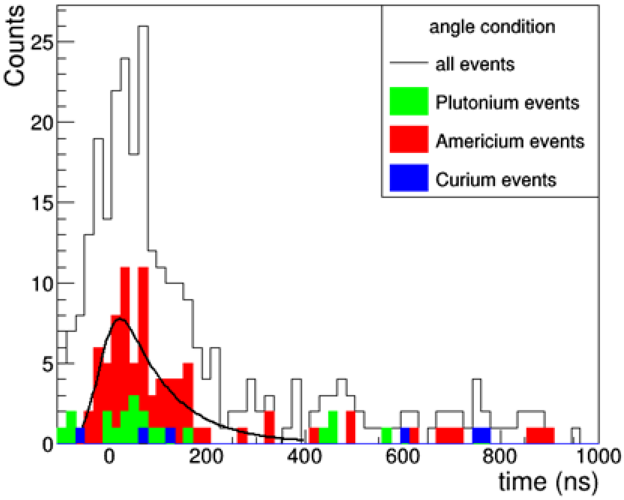

Figure B.9: Spectrum of time coincidences between the particle events recorded in the Micromegas and the γ-rays detected by the scintillation array. The characterisation measurement was performed with a triple alpha source (^{239}Pu, ^{241}Am and ^{244}Cm) in a argon gas mixture Ar(95%)CF$_4$(5%) at 250 mbar. The internal multiplicity trigger and sampling frequency of 12.5 MS/s were set in GET electronics. The voltages applied to the TPC electrodes: cathode -2.8 kV, last inner electrode -240 V, mesh of Micromegas -250 V. The last external electrodes and the gas chamber were grounded. The total spectrum represents all the data information on which the gate on the polar angle was applied. For the data shown as coloured histograms a further gate on the alpha particle clusters was applied. The exponential trends of the red histogram is due to the alpha decay of ^{241}Am and the subsequent gamma decay of ^{237}Np. In black, the fit used for the measurement of the half-life of ^{237}Np, which value obtained is reported in Tab. C.3 of Appendix C (with reference to Argon run 4), is shown.

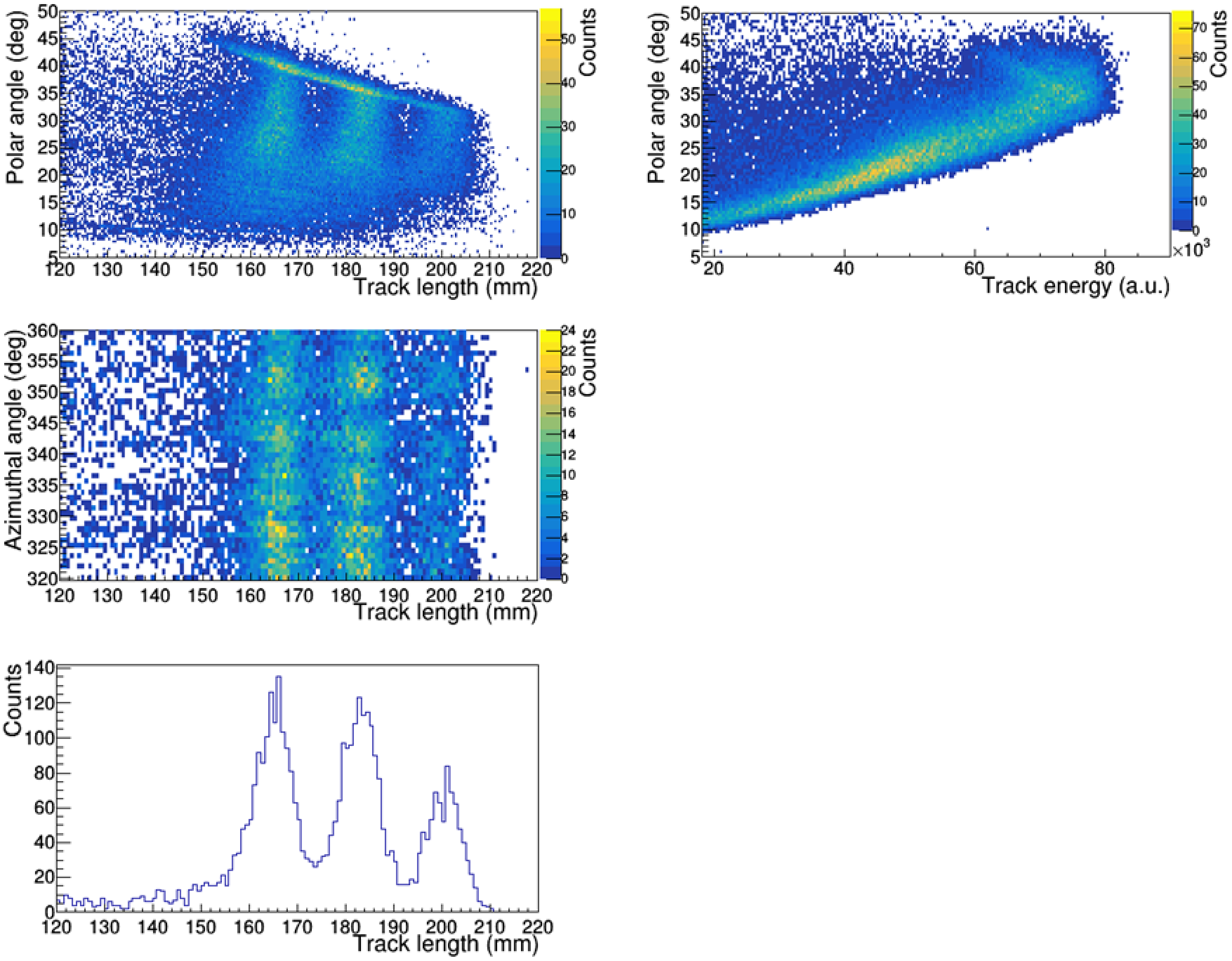

Figure B.10: Number of recorded events as function of the alpha tracks length and the polar and azimuthal angles of the particles emission, inside the active volume of the TPC (left). Number of recorded events as function of the deposited charge on the pad plane and the polar angle of particles emission (right). The characterisation measurement was performed with a triple alpha source (^{239}Pu, ^{241}Am and ^{244}Cm) in a helium gas mixture He(98%)CF$_4$(2%) at 1000 mbar. The internal multiplicity trigger and sampling frequency of 12.5 MS/s were set in GET electronics. The voltages applied to the TPC electrodes: cathode -5.8 kV, last inner electrode -250 V, mesh of Micromegas -260 V. The last external electrodes and the gas chamber were grounded. The plots on the left are based on the ionisation tracks length of the particles produced inside the TPC. The graph on the right is based on the collected charge produced by the particles crossing the TPC volume. The zoom on the azimuthal angle was applied for a better visualisation of the data. The bottom figure represents the energy spectrum based on the track length used for the measurement of the energy resolution. The gates on the polar and azimuthal angles, together with the FWHM value obtained, are reported in Tab. C.4 of Appendix C with reference to Helium run 2.

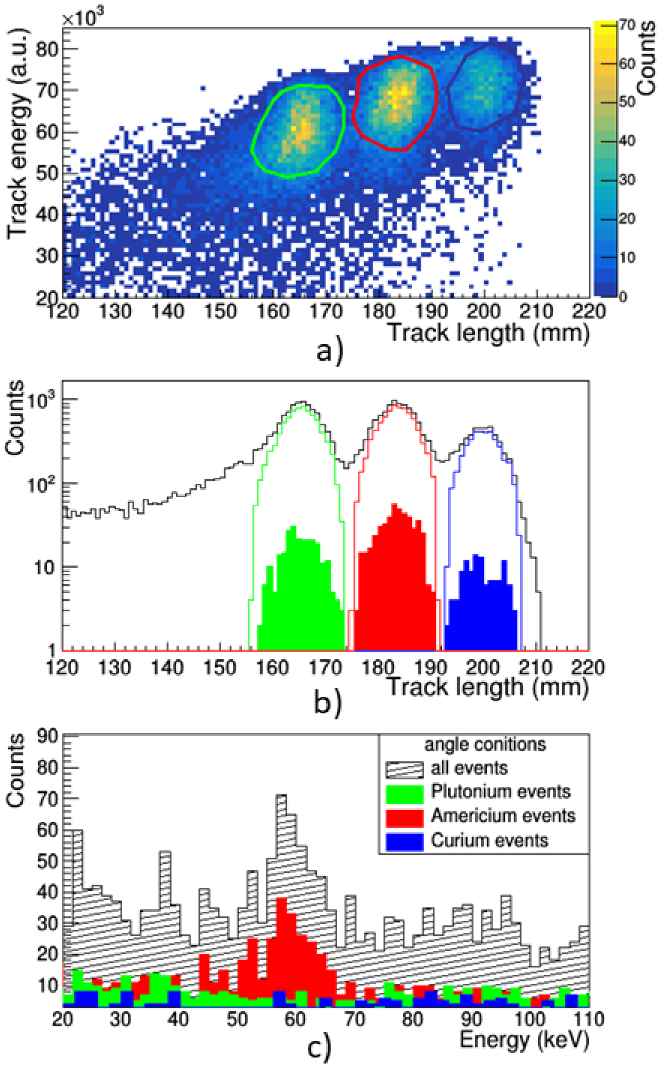

Figure B.11: Correlation plots. The characterisation measurement was performed with a triple alpha source (^{239}Pu, ^{241}Am and ^{244}Cm) in a argon gas mixture He(98%)CF$_4$(2%) at 1000 mbar. The internal multiplicity trigger and sampling frequency of 12.5 MS/s were set in GET electronics. The voltages applied to the TPC electrodes: cathode -5.8 kV, last inner electrode -250 V, mesh of Micromegas -260 V. The last external electrodes and the gas chamber were grounded. A gate on the polar angle ($26^{\circ} < \theta < 35^{\circ}$) was applied. Fig. a) correlates the energy of the charged particles (measured as collected charge) and the tracks length. The three clusters highlighted enclose the events which correspond to the alpha decay of ^{239}Pu, ^{241}Am and ^{244}Cm. Respectively indicated in green, red and blue. The black histogram of Fig. b) was obtained by the projection of the top figure on the track length. The coloured-line peaks in the figure represent the events contained in each singular alpha cluster. The coloured-filled peaks in figure are constituted by particle events recorded in coincidence with γ-rays with an energy range 30 keV - 90 keV. Figure c) reports the total γ-rays spectrum in gray and the spectra with events relative to the γ-rays correlated to the alpha particles inside the clusters with fill-coloured histograms. The red peak at $\sim$ 60 keV contains the gammas emitted from the ^{237}Np decay (daughter nucleus of ^{241}Am).

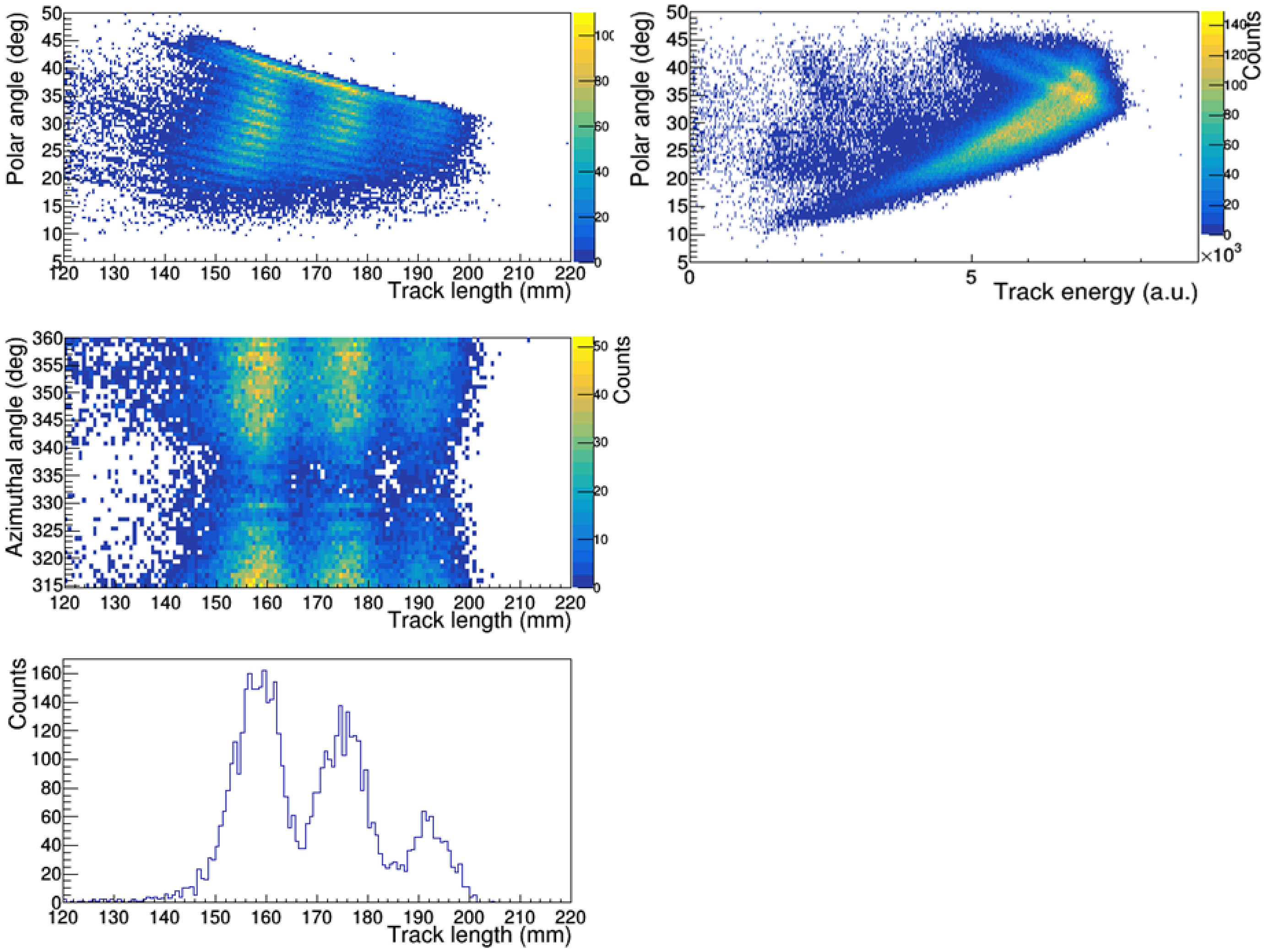

Figure B.12: Number of recorded events as function of the alpha tracks length and the polar and azimuthal angles of the particles emission, inside the active volume of the TPC (left). Number of recorded events as function of the deposited charge on the pad plane and the polar angle of alpha emission (right). The characterisation measurement was performed with a triple alpha source (^{239}Pu, ^{241}Am and ^{244}Cm) in a helium gas mixture He(98%)CF$_4$(2%) at 1000 mbar. The internal multiplicity trigger and sampling frequency of 12.5 MS/s were set in GET electronics. The voltages applied to the TPC electrodes: cathode -5.8 kV, last inner electrode -315 V, mesh of Micromegas -325 V. The last external electrodes and the gas chamber were grounded. The plots on the left are based on the ionisation tracks length of the particles produced inside the TPC. The graph on the right is based on the collected charge produced by the particles crossing the TPC volume. The zoom on the azimuthal angle was applied for a better visualisation of the data. The bottom figure represents the energy spectrum based on the track length used for the measurement of the energy resolution. The gates on the polar and azimuthal angles, together with the FWHM value obtained, are reported in Tab. C.4 of Appendix C with reference to Helium run 3.

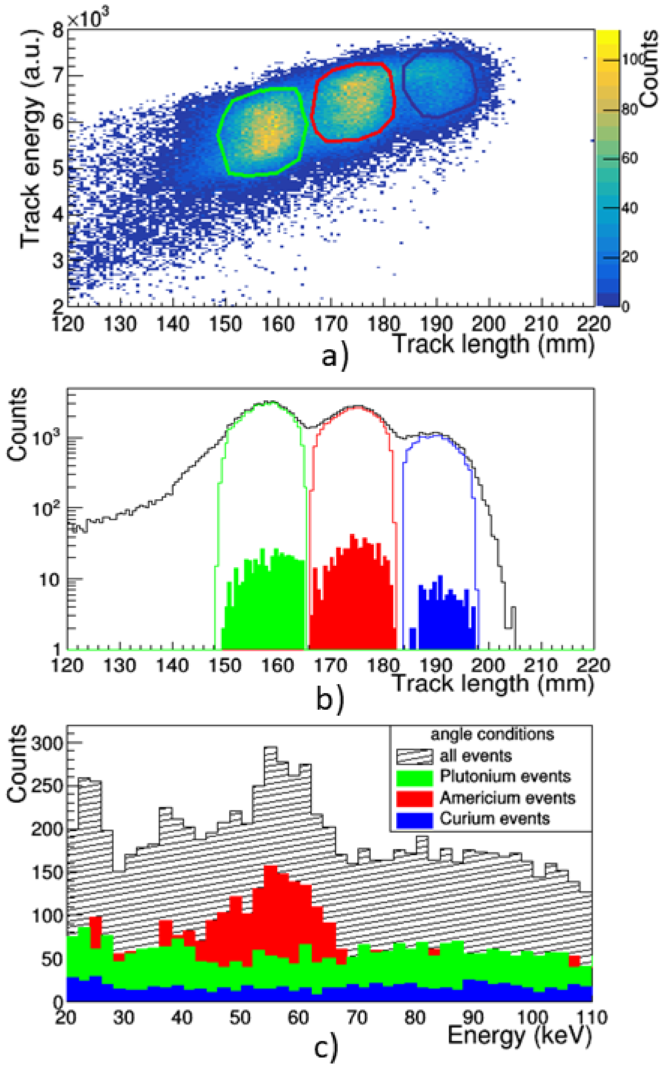

Figure B.13: Correlation plots. The characterisation measurement was performed with a triple alpha source (^{239}Pu, ^{241}Am and ^{244}Cm) in a argon gas mixture He(98%)CF$_4$(2%) at 1000 mbar. The internal multiplicity trigger and sampling frequency of 12.5 MS/s were set in GET electronics. The voltages applied to the TPC electrodes: cathode -5.8 kV, last inner electrode -315 V, mesh of Micromegas -325 V. The last external electrodes and the gas chamber were grounded. A gate on the polar angle ($26° < \theta < 35°$) was applied. Fig. a) correlates the energy of the charged particles (measured as collected charge) and the tracks length. The three clusters highlighted enclose the events which correspond to the alpha decay of ^{239}Pu, ^{241}Am and ^{244}Cm. Respectively indicated in green, red and blue. The black histogram of Fig. b) was obtained by the projection of the top figure on the track length. The coloured-line peaks in the figure represent the events contained in each singular alpha cluster. The coloured-filled peaks in figure are constituted by particle events recorded in coincidence with γ-rays with an energy range 30 keV - 90 keV. Figure c) reports the total γ-rays spectrum in gray and the spectra with events relative to the γ-rays correlated to the alpha particles inside the clusters with fill-coloured histograms. The red peak at $\sim$ 60 keV contains the gammas emitted from the ^{237}Np decay (daughter nucleus of ^{241}Am).

Appendix C

Characterisation of SpecMAT - results

Argon run	**FWHM (keV) (from track length)**	**θ gates (deg)**	**ψ gates (deg)**
1	185 ± 3	38-50	270-285 & 315-340
2	184 ± 3	40-50	5-355
3	185 ± 6	35-38	270-300 & 320-345
4	256 ± 21	31-34	no gate

Table C.1: For each set of data acquired in the argon gas mixture the values obtained for the energy resolution, by using the information of the tracks length of the alpha particles inside the active volume of the TPC, are indicated in table. The energy resolution values are reported as FWHM of the peaks corresponding to Americium-241 in the energy spectra reported in Appendix B (converted from mm to keV). The values given here are for the alpha particles with an energy of $\sim$ 5.5 MeV. The gates on the emission angles (on the polar angle θ and on the azimuthal angle ψ) applied to obtain the energy spectra are also indicated in table.

Argon run	**FWHM (keV) (from collected charge)**	**θ gates (deg)**	**ψ gates (deg)**
1	195 ± 6	38-50	0-20 & 280-300
2	177 ± 4	40-50	280-315
3	230 ± 15	35-38	0-30 & 270-320
4	230 ± 38	31-50	280-300

Table C.2: For each set of data acquired in the argon gas mixture the energy resolution values, obtained by using the information of the collected charge generated by the incoming alpha particles in the TPC, are indicated in table. The energy resolution values are reported as FWHM of the peaks corresponding to Americium-241 in the energy spectra reported in Appendix B. The values given here are for the alpha particles with an energy of $\sim$ 5.5 MeV. The gates on the emission angles (on the polar angle θ and on the azimuthal angle ψ) applied to obtain the energy spectra are also indicated in table.

Argon run	**half-life of ^{237}Np**	**θ gates (deg)**
1	73 ± 8	38-50
2	70 ± 8	35-50
3	67 ± 8	25-40
4	68 ± 23	25-46

Table C.3: In the table, the half-life of ^{237}Np measured is reported. The values were obtained from the parameters of the fits on the the time coincidence spectra. The time difference was measured between the arrival time of the γ-rays, emitted from the ^{237}Np decay and recorded by the CeBr$_3$ crystals of the scintillation array, and the alpha particles detected by the Micromegas detector of SpecMAT.

Helium run	**FWHM (keV) (from tracks length)**	**θ gates (deg)**	**ψ gates (deg)**
1	146 ± 4	28-31	290-310
2	165 ± 5	26-30	320-360
3	196 ± 6	28-31	315-330

Table C.4: For each set of data acquired in the helium gas mixture the values obtained for the energy resolution, by using the information of the tracks length of the alpha particles inside the active volume of the TPC, are indicated in table. The energy resolution values are reported as FWHM of the peaks corresponding to Americium-241 in the energy spectra reported in Appendix B (converted from mm to keV). The values given here are for the alpha particles with an energy of $\sim$ 5.5 MeV. The gates on the emission angles (on the polar angle θ and on the azimuthal angle ψ) applied to obtain the energy spectra are also indicated in table.

Appendix D

Beam energy loss and kinematics curve of $\alpha(^{86}\mathbf{Kr},^{3}\mathbf{He})^{87}\mathbf{Kr}$

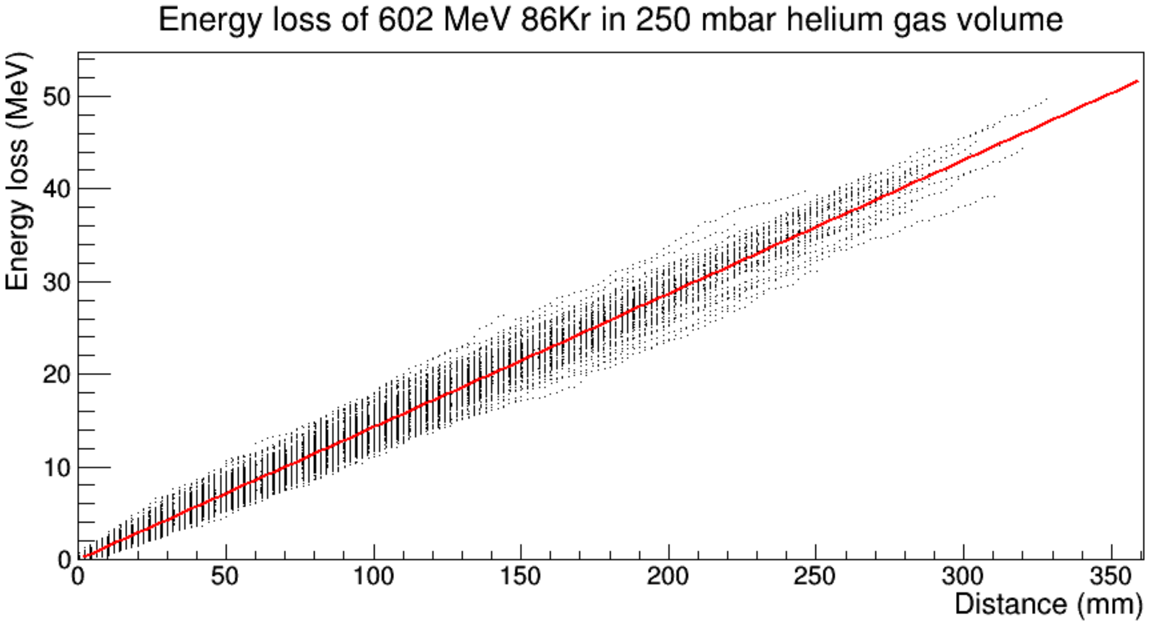

Figure D.1: Energy loss of the ^{86}Kr beam as a function of the distance inside the TPC, inserted as input in the $\alpha(^{86}\mathrm{Kr},^{3}\mathrm{He})^{87}\mathrm{Kr}$ simulation. The initial energy value is 602 MeV. In red the the interpolation of the points is shown. Fig. provided by A Ceulemans.

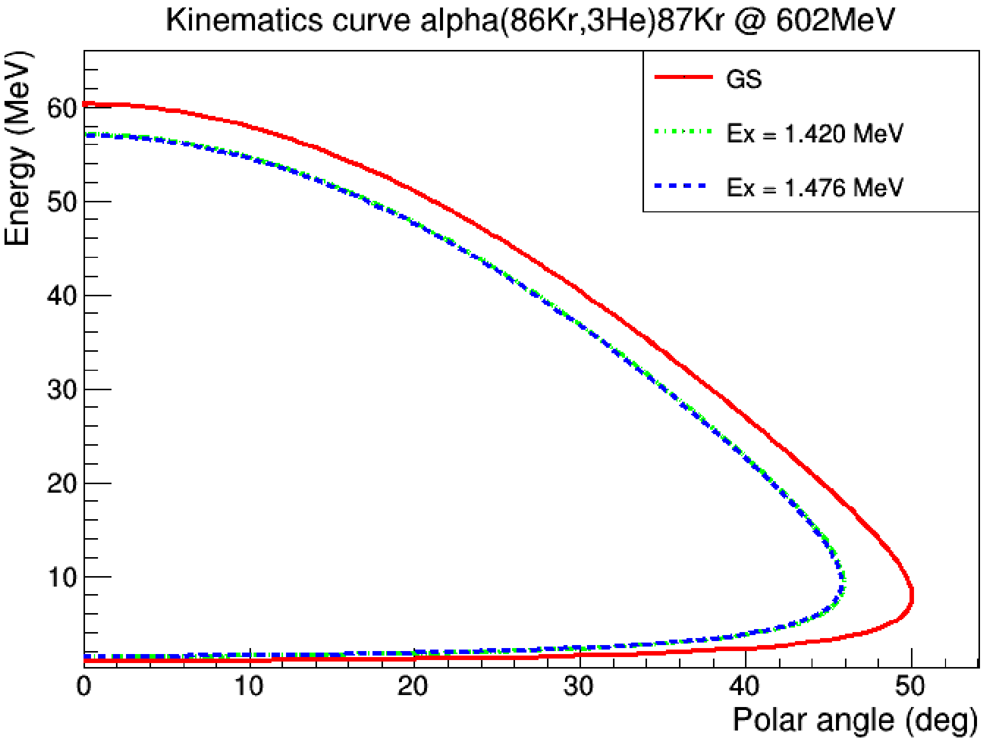

Figure D.2: Kinematics curves of the $\alpha(^{86}\mathrm{Kr},^{3}\mathrm{He})^{87}\mathrm{Kr}$ transfer reaction with 602 MeV energy beam. The energy of the ejectile ^{3}He is shown as a function of the emission polar angle. In red the kinematic curve for the reaction in which ^{87}Kr is produced in the ground state and the dashed line the event with the production of ^{87}Kr in one of the exited states simulated (in green for the 1.420 MeV energy level and in blue for the 1.476 MeV energy level), are reported. In the figure, the two lines corresponding to the exited levels are almost superimposed. The figure was provided by A. Ceulemans and it was obtained by a calculation made using the nptool package.

Bibliography

[1] E. Rutherford F.R.S. LXXIX. The scattering of α and β particles by matter and the structure of the atom. *The London, Edinburgh, and Dublin Philosophical Magazine and Journal of Science*, 21(125):669–688, 1911.

[2] E. Rutherford F.R.S. LIV. Collision of α particles with light atoms IV. An anomalous effect in nitrogen. *The London, Edinburgh, and Dublin Philosophical Magazine and Journal of Science*, 37(222):581–587, 1919.

[3] E. Rutherford. Bakerian lecture: Nuclear constitution of atoms. *Proceedings of The Royal Society A: Mathematical, Physical and Engineering Sciences*, 97:374–400.

[4] J. Chadwick. Possible Existence of a Neutron. *Nature*, 129:312, 1932.

[5] M. Elbistan, P. Zhang, and J. Balog. Neutron–proton scattering and singular potentials. *J. Phys. G*, 45(10):105103, 2018.

[6] R. B. Wiringa, V. G. J. Stoks, and R. Schiavilla. Accurate nucleon-nucleon potential with charge-independence breaking. *Phys. Rev. C*, 51:38–51, Jan 1995.

[7] V. G. J. Stoks, R. A. M. Klomp, C. P. F. Terheggen, and J. J. de Swart. Construction of high-quality NN potential models. *Phys. Rev. C*, 49:2950–2962, Jun 1994.

[8] R. Machleidt. High-precision, charge-dependent Bonn nucleon-nucleon potential. *Phys. Rev. C*, 63:024001, Jan 2001.

[9] W. Heisenberg. Über den Bau der Atomkerne. I. *Zeitschrift für Physik*, 77:1–11, Jan 1932.

[10] S. A. Milne, M. A. Bentley, E. C. Simpson, P. Dodsworth, T. Baugher, D. Bazin, J. S. Berryman, A. M. Bruce, P. J. Davies, C. Aa. Diget, A. Gade, T. W. Henry, H. Iwasaki, A. Lemasson, S. M. Lenzi, S. McDaniel, D. R. Napoli, A. J. Nichols, A. Ratkiewicz, L. Scruton, S. R. Stroberg, J. A. Tostevin, D. Weisshaar, K. Wimmer, and R. Winkler. Mirrored one-nucleon knockout reactions to the $T_z = \pm\frac{3}{2} a = 53$ mirror nuclei. *Phys. Rev. C*, 93:024318, Feb 2016.

[11] Kenneth S Krane. *Introductory nuclear physics.* Wiley, New York, NY, 1988.

[12] S.R. Beane, W. Detmold, K. Orginos, and M.J. Savage. Nuclear physics from lattice QCD. *Progress in Particle and Nuclear Physics*, 66(1):1–40, Jan 2011.

[13] G. Hagen, A. Ekström, C. Forssén, G. R. Jansen, W. Nazarewicz, T. Papenbrock, K. A. Wendt, S. Bacca, N. Barnea, B. Carlsson, C. Drischler, K. Hebeler, M. Hjorth-Jensen, M. Miorelli, G. Orlandini, A. Schwenk, and J. Simonis. Neutron and weak-charge distributions of the ^{48}Ca nucleus. *Nature Physics*, 12:186–190, Feb 2016.

[14] Walter M. Elsasser. Sur le principe de Pauli dans les noyaux - III. *Journal De Physique Et Le Radium*, 5:635–639, 1934.

[15] K. Guggenheimer. Remarques sur la constitution des noyaux - II. *J. Phys. Radium*, 5(9):475–485, 1934.

[16] Maria G. Mayer. On closed shells in nuclei. *Phys. Rev.*, 74:235–239, Aug 1948.

[17] Maria G. Mayer. On closed shells in nuclei. II. *Phys. Rev.*, 75:1969–1970, Jun 1949.

[18] O. Haxel, J. Hans D. Jensen, and Hans E. Suess. On the ”magic numbers” in nuclear structure. *Phys. Rev.*, 75:1766–1766, Jun 1949.

[19] National Nuclear Data Center at Brookhaven National Laboratory. `https://www.nndc.bnl.gov/nudat3`.

[20] M. L. Terranova and O. A. P. Tavares. The periodic table of the elements: the search for transactinides and beyond. *Rendiconti Lincei. Scienze Fisiche e Naturali*, 33:1–16, 2022.

[21] T. L. Tang, B. P. Kay, C. R. Hoffman, J. P. Schiffer, D. K. Sharp, L. P. Gaffney, S. J. Freeman, M. R. Mumpower, A. Arokiaraj, E. F. Baader, P. A. Butler, W. N. Catford, G. de Angelis, F. Flavigny, M. D. Gott, E. T. Gregor, J. Konki, M. Labiche, I. H. Lazarus, P. T. MacGregor, I. Martel, R. D. Page, Zs. Podolyák, O. Poleshchuk, R. Raabe, F. Recchia, J. F. Smith, S. V. Szwec, and J. Yang. First exploration of neutron shell structure below lead and beyond $n = 126$. *Phys. Rev. Lett.*, 124:062502, Feb 2020.

[22] John Douglas Cockcroft, E. T. S. Walton, and Ernest Rutherford. Experiments with high velocity positive ions. II. -The disintegration of elements by high velocity protons. *Proceedings of the Royal Society of London. Series A, Containing Papers of a Mathematical and Physical Character*, 137(831):229–242, 1932.

[23] O. Kofoed-Hansen and K. O. Nielsen. Short-lived krypton isotopes and their daughter substances. *Phys. Rev.*, 82:96–97, Apr 1951.

[24] B. Bastin, S. Grévy, D. Sohler, O. Sorlin, Zs. Dombrádi, N. L. Achouri, J. C. Angélique, F. Azaiez, D. Baiborodin, R. Borcea, C. Bourgeois, A. Buta, A. Bürger, R. Chapman, J. C. Dalouzy, Z. Dlouhy, A. Drouard, Z. Elekes, S. Franchoo, S. Iacob, B. Laurent, M. Lazar, X. Liang, E. Liénard, J. Mrazek, L. Nalpas, F. Negoita, N. A. Orr, Y. Penionzhkevich, Zs. Podolyák, F. Pougheon, P. Roussel-Chomaz, M. G. Saint-Laurent, M. Stanoiu, I. Stefan, F. Nowacki, and A. Poves. Collapse of the $N = 28$ Shell Closure in ^{42}Si. *Phys. Rev. Lett.*, 99:022503, Jul 2007.

[25] R. Kanungo, C. Nociforo, A. Prochazka, T. Aumann, D. Boutin, D. Cortina-Gil, B. Davids, M. Diakaki, F. Farinon, H. Geissel, R. Gernhäuser, J. Gerl, R. Janik, B. Jonson, B. Kindler, R. Knöbel, R. Krücken, M. Lantz, H. Lenske, Y. Litvinov, B. Lommel, K. Mahata, P. Maierbeck, A. Musumarra, T. Nilsson, T. Otsuka, C. Perro, C. Scheidenberger, B. Sitar, P. Strmen, B. Sun, I. Szarka, I. Tanihata, Y. Utsuno, H. Weick, and M. Winkler. One-neutron removal measurement reveals ^{24}O as a new doubly magic nucleus. *Phys. Rev. Lett.*, 102:152501, Apr 2009.

[26] R. Kanungo, I. Tanihata, and A. Ozawa. Observation of new neutron and proton magic numbers. *Physics Letters B*, 528(1):58–64, 2002.

[27] R. Raabe. Making radioactive ion beams - Detecting reaction products. *European physical journal plus*, 131(10):1–27, 2016.

[28] O. Kamigaito. Overview of the world-wide RIB facilities-status and challenges. *Proceedings of IPAC2013, Shanghai, China*, 2013.

[29] M.J.G. Borge. Highlights of the ISOLDE facility and the HIE-ISOLDE project. *Nuclear Instruments and Methods in Physics Research Section B: Beam Interactions with Materials and Atoms*, 376:408–412, 2016.

[30] ISOLDE website. `http://isolde.web.cern.ch`.

[31] A.C.C. Villari. The accelerated ISOL technique and the SPIRAL project. *Nuclear Physics A*, 693(1):465–476, 2001.

[32] Marek Lewitowicz. The SPIRAL2 project and experiments with high-intensity rare isotope beams. *Journal of Physics: Conference Series*, 312(5):052014, sep 2011.

[33] G C Ball, L Buchmann, B Davids, R Kanungo, C Ruiz, and C E Svensson. Physics with reaccelerated radioactive beams at TRIUMF-ISAC. *Journal of Physics G: Nuclear and Particle Physics*, 38(2):024003, jan 2011.

[34] G. Pretea, A. Andrighetto, M. Manzolaro, S. Corradetti, D. Scarpa, M. Rossignoli, A. Monetti, M. Lollo, M. Calderolla, J. Vasquez, D. Zafiropoulos, L. Sarchiapone, D. Benini, P. Favaron, M. Rigato, R. Pegoraro, D. Maniero, L. Calabretta, M. Comunian, M. Maggiore, A. Lombardi, L. Piazza, A.M. Porcellato, C. Roncolato, G. Bisoffi, A. Pisent, A. Galatà, M. Giacchini, G. Bassato, S. Canella, F. Gramegna, J. Valiente, J. Bermudez, P.F. Mastinu, J. Esposito, J. Wyss, and S. Zanella. The SPES project at the INFN- Laboratori Nazionali di Legnaro. *EPJ Web of Conferences*, 66:11030, 2014.

[35] G. F. Knoll. *Radiation Detection and Measurement.* Wiley, Hoboken, 4th ed. edition, 2010.

[36] H. Geissel, P. Armbruster, K.H. Behr, A. Brünle, K. Burkard, M. Chen, H. Folger, B. Franczak, H. Keller, O. Klepper, B. Langenbeck, F. Nickel, E. Pfeng, M. Pfützner, E. Roeckl, K. Rykaczewski, I. Schall, D. Schardt, C. Scheidenberger, K.-H. Schmidt, A. Schröter, T. Schwab, K. Sümmerer, M. Weber, G. Münzenberg, T. Brohm, H.-G. Clerc, M. Fauerbach, J.-J. Gaimard, A. Grewe, E. Hanelt, B. Knödler, M. Steiner, B. Voss, J. Weckenmann, C. Ziegler, A. Magel, H. Wollnik, J.P. Dufour, Y. Fujita, D.J. Vieira, and B. Sherrill. The GSI projectile fragment separator (FRS): a versatile magnetic system for relativistic heavy ions. *Nuclear Instruments and Methods in Physics Research Section B: Beam Interactions with Materials and Atoms*, 70(1):286–297, 1992.

[37] GSI website. `http://www.gsi.de/en`.

[38] T. Kubo, D. Kameda, H. Suzuki, N. Fukuda, H. Takeda, Y. Yanagisawa, M. Ohtake, K. Kusaka, K. Yoshida, N. Inabe, T. Ohnishi, A. Yoshida, K. Tanaka, and Y. Mizoi. BigRIPS separator and ZeroDegree spectrometer at RIKEN RI Beam Factory. *Progress of Theoretical and Experimental Physics*, 2012(1), 12 2012.

[39] GANIL website. `http://www.ganil-spiral2.eu`.

[40] NSCL website. `https://www.nscl.msu.edu`.

[41] M. Thoennessen. Plans for the facility for rare isotope beams. *Nuclear Physics A*, 834(1):688c–693c, 2010. The 10th International Conference on Nucleus-Nucleus Collisions (NN2009).

[42] William R Leo. *Techniques for nuclear and particle physics experiments: a how-to approach.* Springer, Berlin New York, 2nd rev. ed. edition, 1994.

[43] Jay N. Marx and David R. Nygren. The Time Projection Chamber. *Phys. Today*, 31N10:46–53, 1978.

[44] D. Bazin, T. Ahn, Y. Ayyad, S. Beceiro-Novo, A. O. Macchiavelli, W. Mittig, and J. S. Randhawa. Low energy nuclear physics with active targets and time projection chambers. *Prog. Part. Nucl. Phys.*, 114:103790, 2020.

[45] S. Beceiro-Novo, T. Ahn, D. Bazin, and W. Mittig. Active targets for the study of nuclei far from stability. *Prog. Part. Nucl. Phys.*, 84:124–165, 2015.

[46] Riccardo Raabe. *Nuclear Structure Studies with Active Targets*, pages 209–243. Springer International Publishing, Cham, 2022.

[47] J. Bradt, D. Bazin, F. Abu-Nimeh, T. Ahn, Yassid Ayyad, Saul Beceiro-Novo, L. Carpenter, Marco Cortesi, Michelle Kuchera, William Lynch, Wolfgang Mittig, Stefan Rost, N. Watwood,

and John Yurkon. Commissioning of the active-target time projection chamber. *Nuclear Instruments and Methods in Physics Research Section A: Accelerators, Spectrometers, Detectors and Associated Equipment*, 875:65–79, 09 2017.

[48] R. Raabe, A. Ceulemans A. A. Arokjaraj and, H. De Witte, S. Fracassetti, M. Latif, T. Marchi, A. Mentana, O. Poleshchuk, M. Renaud, A. Youssef, the ACTAR TPC Collaboration, , and the ISS Collaboration. The SpecMAT active target. *European Organization For Nuclear Research.*, 2020.

[49] C.E. Demonchy, W. Mittig, H. Savajols, P. Roussel-Chomaz, M. Chartier, B. Jurado, L. Giot, D. Cortina-Gil, M. Caamaño, G. Ter-Arkopian, A. Fomichev, A. Rodin, M.S. Golovkov, S. Stepantsov, A. Gillibert, E. Pollacco, A. Obertelli, and H. Wang. MAYA, a gaseous active target. *Nuclear Instruments and Methods in Physics Research Section A: Accelerators, Spectrometers, Detectors and Associated Equipment*, 573(1):145–148, 2007. Proceedings of the 7th International Conference on Position-Sensitive Detectors.

[50] B. Mauss, P. Morfouace, T. Roger, J. Pancin, G.F. Grinyer, J. Giovinazzo, V. Alcindor, H. Álvarez Pol, A. Arokiaraj, M. Babo, B. Bastin, C. Borcea, M. Caamaño, S. Ceruti, B. Fernández-Domínguez, E. Foulon-Moret, P. Gangnant, S. Giraud, A. Laffoley, G. Mantovani, T. Marchi, B. Monteagudo, J. Pibernat, O. Poleshchuk, R. Raabe, J. Refsgaard, A. Revel, F. Saillant, M. Stanoiu, G. Wittwer, and J. Yang. Commissioning of the ACtive TARget and Time Projection Chamber (ACTAR TPC). *Nuclear Instruments and Methods in Physics Research Section A: Accelerators, Spectrometers, Detectors and Associated Equipment*, 940:498–504, 2019.

[51] R. D. Evans. *The Atomic Nucleus.* McGraw-Hill, 1955.

[52] O. Poleshchuk. *SpecMAT, the active target for transfer reaction studies and gamma-ray spectroscopy in a strong magnetic field.* PhD thesis, KU Leuven. Faculty of Science, Leuven, 2021.

[53] O. Poleshchuk, R. Raabe, S. Ceruti, A. Ceulemans, H. De Witte, T. Marchi, A. Mentana, J. Refsgaard, and J. Yang. The SpecMAT active target. *Nuclear Instruments and Methods in Physics Research Section A: Accelerators, Spectrometers, Detectors and Associated Equipment*, 1015:165765, 2021.

[54] Y. Giomataris, Ph. Rebourgeard, J.P. Robert, and G. Charpak. Micromegas: a high-granularity position-sensitive gaseous detector for high particle-flux environments. *Nuclear Instruments and Methods in Physics Research Section A: Accelerators, Spectrometers, Detectors and Associated Equipment*, 376(1):29–35, 1996.

[55] O. Poleshchuk, J.A. Swartz, A. Arokiaraj, S. Ceruti, H. De Witte, G.F. Grinyer, A.T. Laffoley, T. Marchi, R. Raabe, M. Renaud, and J. Yang. Performance tests of a $LaBr_3$:Ce detector coupled to a SiPM array and the GET electronics for γ-ray spectroscopy in a strong magnetic field. 987:164863, 2021.

[56] E.C. Pollacco, G.F. Grinyer, F. Abu-Nimeh, T. Ahn, S. Anvar, A. Arokiaraj, Y. Ayyad, H. Baba, M. Babo, P. Baron, D. Bazin, S. Beceiro-Novo, C. Belkhiria, M. Blaizot, B. Blank, J. Bradt, G. Cardella, L. Carpenter, S. Ceruti, E. De Filippo, E. Delagnes, S. De Luca, H. De Witte, F. Druillole, B. Duclos, F. Favela, A. Fritsch, J. Giovinazzo, C. Gueye, T. Isobe, P. Hellmuth, C. Huss, B. Lachacinski, A.T. Laffoley, G. Lebertre, L. Legeard, W.G. Lynch, T. Marchi, L. Martina, C. Maugeais, W. Mittig, L. Nalpas, E.V. Pagano, J. Pancin, O. Poleshchuk, J.L. Pedroza, J. Pibernat, S. Primault, R. Raabe, B. Raine, A. Rebii, M. Renaud, T. Roger, P. Roussel-Chomaz, P. Russotto, G. Saccà, F. Saillant, P. Sizun, D. Suzuki, J.A. Swartz, A. Tizon, A. Trifiró, N. Usher, G. Wittwer, and J.C. Yang. GET: A generic electronics system for TPCs and nuclear physics instrumentation. *Nuclear Instruments and Methods in Physics Research Section A: Accelerators, Spectrometers, Detectors and Associated Equipment*, 887:81–93, 2018.

[57] D. K. Sharp, B. P. Kay, J. S. Thomas, S. J. Freeman, J. P. Schiffer, B. B. Back, S. Bedoor, T. Bloxham, J. A. Clark, C. M. Deibel, C. R. Hoffman, A. M. Howard, J. C. Lighthall, S. T. Marley, A. J. Mitchell, T. Otsuka, P. D. Parker, K. E. Rehm, D. V. Shetty, and A. H. Wuosmaa. Neutron single-particle strength outside the N = 50 core. *Phys. Rev. C*, 87:014312, Jan 2013.

[58] A.H. Wuosmaa, J.P. Schiffer, B.B. Back, C.J. Lister, and K.E. Rehm. A solenoidal spectrometer for reactions in inverse kinematics. *Nuclear Instruments and Methods in Physics Research Section A: Accelerators, Spectrometers, Detectors and Associated Equipment*, 580(3):1290–1300, 2007.

Acknowledgements

I would like to express my deepest gratitude to my supervisors, prof. Francesco Recchia and prof. Riccardo Raabe, for giving me the opportunity to work on this thesis project, for their precious advice and suggestions and for their guidance on my learning process of the scientific method.

I would also like to thank my co-supervisors, Dr. Oleksii Poleshchuk and Andreas Ceulemans, for their constant and continuous support during the whole period of this research activity.

I am grateful to the Department of Physics and Astronomy of the University of Padova for the meaningful study path which allowed me to follow and pursue, and the Department of Physics and Astronomy of the KU Leuven University for the opportunity to work in the owned structures and laboratories and for allowing me to gain research experiences at CERN and at the Ganil laboratories.

I would also like to give special thanks to my family for the warm and unconditional support in these years.

Anita